University of Strathclyde, Glasgow
Department of Civil and Environmental Engineering

METROLOGICAL EFFECTIVENESS OF DIAGNOSTIC TECHNIQUES FOR POST-TENSIONED CONCRETE BRIDGES

PhD Student: Francesco Rossi

Supervisors:

Enrico Tubaldi
John Quigley
Daniele Zonta

A thesis presented in fulfilment of the requirements for the degree of
Doctor of Philosophy

May, 2024

DECLARATION OF AUTHENTICITY AND AUTHOR'S RIGHTS

This thesis is the result of the author's original research. It has been composed by the author and has not been previously submitted for examination which has led to the award of a degree.

Signed: 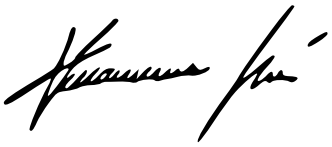

Date: 29/05/2024

ABSTRACT

Prestressed concrete (PC) bridges, widespread in transportation networks globally, face escalating challenges due to ageing and deterioration. This thesis addresses the critical need for accurate assessment and monitoring methodologies to ensure the safety and reliability of these structures. Focusing on Post-Tensioned (PT) concrete bridges, particularly those built before the 1980s, this research investigates the effectiveness of Structural Health Monitoring (SHM), Non-Destructive Testing (NDT), and modelling techniques in evaluating their condition.

Drawing from empirical data gathered from an extensive experimental campaign conducted on the Alveo Vecchio viaduct. This is a PT concrete viaduct, constructed in 1968 and decommissioned in 2005, representative of many bridges in the Italian highway network.

After introducing the experimental campaign, the dissertation analyses the results of comprehensive load tests pushing a bridge span up to failure, thus providing valuable insights into the structural behaviour under service and extreme loading conditions and into the accuracy of analytical and FE models for describing this behaviour. Subsequently, the accuracy and reliability of one of the most diffused SHM system, Acoustic Emission (AE) monitoring, is evaluated. Finally, some NDT techniques, including Digital Radiography (DR), Ground Penetration Radar (GPR), and Reflectometric Impulse Measurement Test (RIMT), currently used for detecting structural anomalies and assessing the integrity of prestressing systems are assessed.

Through a comprehensive evaluation of the empirical findings, this thesis offers critical insights into the state of PT bridges and the effectiveness of SHM and NDT techniques for assessing their conditions. The research outcomes are useful to bridge engineers and manage and provide a contribution towards better informed decision-making in bridge management and maintenance.

AKNOWLEDGMENT

I would like to acknowledge my gratitude to the professors and researchers who have contributed to my PhD journey.

Firstly, I am deeply thankful to my primary supervisors, Prof. Daniele Zonta and Prof. Enrico Tubaldi, for their unwavering support, mentorship, and encouragement throughout my research endeavors. Their guidance has been invaluable. I also appreciate my second supervisor, Prof. John Quigley, whose insights have played a crucial role in shaping my PhD.

Among the many researchers I have had the privilege to collaborate with, I wish to acknowledge Stefano Zorzi, Daniel Tonelli, Denise Bolognani, and Emiliano De Biasi from the University of Trento, as well as Andrea Verzobio from the University of Strathclyde. Their collaboration and support have been indispensable in developing my research studies. Working alongside them has been both a pleasure and an enriching professional experience. I want to convey to them that this achievement of mine is also a testament to their contributions, underscoring the significance of their support in enabling me to complete this research work.

LIST OF FIGURES

Figure 2.1 Radiography acquisition of an object investigated affected by a defect. 35

Figure 2.2 Georadar acquisition of an object investigated affected by a defect. 36

Figure 2.3 Reflectometric acquisition of an object investigated affected by a defect. 37

Figure 3.1 (a) top view; (b) lateral view; and (c) cross-section of the Alveo Vecchio viaduct (Italy).....44

Figure 3.2 Longitudinal and transversal section of girders with post-tensioned cables 45

Figure 3.3 (a and b) Mapping activity of the actual condition state of a prestressing cable; (c) procedure adopted during the night; (d) 1 m long ruler positioned for mapping the condition state of the metal duct; (e) 1 m long ruler positioned for mapping the condition state of the injected grout and the steel cable. 47

Figure 4.1 (a) Age distribution among a sample of 1945 Italian highway bridges (more than 65% across the Nation); (b) Age distribution among 1019 Italian PC highway bridges with simply-supported spans (52% of the whole sample) 54

Figure 4.2 (a) top view; (b) lateral view; and (c) cross-section of the Alveo Vecchio viaduct (Italy).....54

Figure 4.3 Longitudinal and transversal section of girders with post-tensioned cables 55

Figure 4.4 a) Live-loads configuration used to design the Alveo Vecchio viaduct; (b) Most demanding live load configuration that can transit nowadays on Italian highways in compliance with dimensional and mass limits.....56

Figure 4.5 Load unit configuration and sequence of weights application repeated for each layer.....56

Figure 4.6 Loading phases P1 – P5 with a progressive number of steel ballasts. Colours: green is equivalent to the load unit; yellow is twice the load unit; red is 3 and 4 times the load unit 57

Figure 4.7 Loading phases PP (weights on the pier) and PA (weights on the abutment) with 4800 kN each 58

Figure 4.8 Location of the extracted samples and NDTs along the viaduct.....59

Figure 4.9 a) Discretisation of (a) the bridge span and girders and (b) the prestressing cables in frame finite elements with fibre section 64

Figure 4.10 Pictures of the Alveo Vecchio viaduct during the loading phases (a) PP – 4800 kN; (b) PA – 4800 kN; (c) P1 – 1200 kN, (d) P2 – 2400 kN, (e) P3 – 4800 kN, (f) P4 – 7200 kN, and (g) P5 – 9600 kN 66

Figure 4.11 Layout of the structural health monitoring system installed on the Alveo Vecchio viaduct during the load test 68

Figure 4.12 Deflection of the girders midspan plotted against the load measured during the loading phases P1 – P5 69

Figure 4.13 Longitudinal deformed shape of girders (a) T1, (b) T2, (c) T3, and (d) T4 at the end of each loading phase 70

Figure 4.14 Vertical deformation of elastomeric bearings of girder T1 over (a) the abutment and (b) the pier; longitudinal strain measured at the bottom of the midspan of girders (c) T1 and (d) T4 during the load test 71

Figure 4.15 Visible cracks on the middle portion of girder T4 opened during the loading phases P3 (amber triangles), P4 (red single triangles), and P5 (red double triangles) 72

Figure 4.16 Non compensated (NC) and temperature compensated (TC) deflections measured at the midspan of the girder T1 during the loading phase (a) P1, (b) P2, (c) P3. (d) Difference between TC and NC deflections during loading phases P1, P2, P3 73

Figure 4.17 (a) FRFs from the accelerometer located on the girder T4 under the weight drops before P1 and at the end of each unloading phase. (b) variation of the first two modal frequencies during the load test 75

Figure 4.18 (a) Envelope of the vertical deflection at the girders' midspan plotted against the load and 76

Figure 4.19 Comparison between the predicted and the observed deflections at the midspan of girders (a) T1, (b) T2, (c) T3, and (d) T4 77

Figure 4.20 Differences between model predictions and observed response. Quantities are expressed in % respect to the observed value of the elastic stiffness and ultimate capacity, respectively. Error = abs (observation – prediction)/observation % 83

Figure 5.1 Working principle of an AE monitoring system. 94

Figure 5.2 AE signal and parameters expressed in the time-domain. 95

Figure 5.3 AE signal and parameters expressed in the frequency-domain. 95

Figure 5.4 Peak definition time (PDT), hit definition time (HDT), and hit lockout time (HLT). They discriminate one hit from another. 96

Figure 5.5 (a) top view; (b) lateral view; and (c) cross-section of the Alveo Vecchio viaduct (Italy) 97

Figure 5.6 Longitudinal and transversal section of girders with post-tensioned cables 97

Figure 5.7 Monitoring system layout (only sensors relevant in our analysis). 98

Figure 5.8 Load-test protocol: five loading phases with an increasing number of ballast weights. 99

Figure 5.9 The Alveo Vecchio viaduct during the loading phase 5, loaded with 93 weights—9300 kN 99

Figure 5.10 (a) Vertical displacements along girder T1 in the five loading phases; (b) load-deflection curve of girder T1 and its trilinear idealized flexural response. 101

Figure 5.11 Longitudinal strain at the bottom of the middle cross section of girder T1: (a) loading phase P3; (b) loading phase P4. The red dashed line represents the first-crack load identified by crack-opening sensors 101

Figure 5.12 Visible cracks on girder T1 opened during the loading phase P3 4800 kN. 102

Figure 5.13 Visible cracks on girder T1 opened during the loading phase P4 7200 kN. 102

Figure 5.14 Results in the time-domain from the loading phase P3 4800 kN: (a) amplitude; (b) cumulative number of hits; (c) signal strength; and (d) cumulative signal strength. 103

Figure 5.15 Results in the frequency-domain from the loading phase P3 4800 kN: (a) amplitude and load—peak-frequency; (b) peak frequency distribution among hits 103

Figure 5.16 . Results from AE and crack-opening sensors during phase P3: (a) amplitude from girder T2; (b) cumulative signal strength from girder T2; (c) longitudinal strain at the bottom of girder T1. 104

Figure 5.17 Results in the time-domain from the loading phase P4 7200 kN: (a) amplitude; (b) cumulative number of hits; (c) signal strength; and (d) cumulative signal strength. 104

Figure 5.18 Results in the frequency-domain from the loading phase P4 7200 kN: (a) amplitude and load—peak-frequency; (b) peak frequency distribution among hits.....105

Figure 5.19 Results from AE and LVDT sensors during phase P4: (a) amplitude from girder T2; (b) cumulative signal strength from girder T2; (c) longitudinal strain at the bottom of girder T1.....105

Figure 5.20 Differences in amplitude (a,b) and cumulative signal strength (c,d) between the AE acquired from the viaduct without pre-existent cracks (phase P3) and with pre-existent cracks (phase P4) for loads between 0 kN and 2400 kN. 109

Figure 5.21 Kaiser and Felicity effects in the AE acquired during the loading phases P3 and P4. 109

Figure 6.1 (a) top view; (b) lateral view; and (c) cross-section of the Alveo Vecchio viaduct (Italy).....115

Figure 6.2 Longitudinal and transversal section of girders with post-tensioned cables 116

Figure 6.3 a) Inspectors at work with the X-ray low-intensity source; (b) the high-intensity source; (c) the receiver panel; (d) the real-time outcome on a mobile screen. 118

Figure 6.4 Portions of girders inspected with DR.....119

Figure 6.5 Defect intensity scale to interpret DR outcomes and identify the presence of grouting void in the prestressing cable. 119

Figure 6.6 Superposition of a portion of DR outputs over the corresponding area of the longitudinal section of the girder T1.....120

Figure 6.7 Inspectors performing GPR on: (a and b) the girder's web; (c and d) the girder's lower flange. 121

Figure 6.8 Portions of girders inspected with GPR 121

Figure 6.9 Defect intensity scale to interpret GPR outcomes and identify corrosion in the prestressing system. 121

Figure 6.10 Superposition of a portion of GPR outputs over the corresponding area of the longitudinal section of the girder T1.....122

Figure 6.11 a) Inspector cleaning the rust from the steel wires with a metallic brush; (b) the cleaned steel cables 'anchorages; (c) Inspectors performing RIMT; (d) real-time outcome. 123

Figure 6.12 Prestressing cables investigated with RIMT. 123

Figure 6.13 a) demolition of the concrete slab; (b) demolition of the 5 cross-girders; (c) movement of the girders; (d) positioning of the girders on the ground; (e) excavator with the hydraulic crusher pliers; (f) demolition of the girders; (g) extraction of the prestressing system; (h)positioning of the prestressing cables on the ground; (i) mapping of the actual state of the prestressing system. 124

Figure 6.14 Discretisation in sixteenths of the samples used to map the actual condition state of the metal ducts. 125

Figure 6.15 Intensity scales to quantify the defects which can affect the metal ducts in the prestressing system. 126

Figure 6.16 Intensity scale used to classify the grade of grout fracturing (G.F) in the prestressing system. 127

Figure 6.17 Intensity scale used to classify percentage of grouting void (G.V) in the prestressing system. 127

Figure 6.18 Discretisation in twelfths of the samples used to map the actual condition state of two defects which can affect the steel wires. 128

Figure 6.19 Intensity scales used to quantify the steel wires corrosion (S.C) and the steel wires interruptions (S.I) in the prestressing system. 128

Figure 6.20 Example of quantification of the area reduction (S.R) in the corroded samples. 129

Figure 6.21 Intensity scale used to classify the steel threads area reduction (S.R) in the prestressing system. 129

Figure 6.22 Examples of contingency tables. a) case with very strong correlation; b) case with poor correlation. 132

Figure 6.23 Intensity of grouting void (G.V) defect of the samples in the portions of cables investigated with DR (DR.V). 135

Figure 6.24 Intensity of corrosion of the samples in the portions of cables investigated with GPR (GPR.C). 135

Figure 6.25 Intensity of grouting void of the samples in the portions of cables investigated with RIMT (RIMT.V). 136

Figure 6.26 Intensity of corrosion of the samples in the portions of cables investigated with RIMT (RIMT.C). 136

Figure 6.27 Actual grade of grout fracturing (G.F) of the samples observed during the dissection. (a) Girder T1, 3871 samples; (b) girder T2, 3871 samples; (c) girder T3, 4158 samples; (d) girder T4, 4030 samples. 137

Figure 6.28 Actual percentage of grouting void (G.V) of the samples observed during the dissection..... 137

Figure 6.29 Actual intensity of steel corrosion (S.C) of the samples observed during the dissection..... 138

Figure 6.30 Comparison between NDTs outputs and the actual intensity of defects observed in the injected grout. 139

Figure 6.31 Comparison between DR.V and G.F. 139

Figure 6.32 Comparison between DR.V and G.V. 140

Figure 6.33 Comparison between DR.V and G.V limited at the cables anchored at the slab. (a) Contingency table; (b) Conditional probability table. Above the tables the Spearman's correlation coefficient is reported. 140

Figure 6.34 Comparison between RIMT.V and G.F. (a) Contingency table; (b) conditional probability table. In the upside the Spearman's correlation coefficient obtained..... 141

Figure 6.35 Comparison between RIMT.V and G.V. (a) Contingency table; (b) conditional probability table. In the upside the Spearman's correlation coefficient obtained..... 141

Figure 6.36 Comparison between NDTs outputs and the actual intensity of corrosion observed in the steel wires. 142

Figure 6.37 Comparison between GPR.C and S.C. 142

Figure 6.38 Comparison between GPR.C and S.C limited at the cables anchored at the slab. 143

Figure 6.39 Comparison between RIMT.C and S.C. 144

LIST OF TABLES

Table 3.1 Materials properties of the Alveo Vecchio viaduct. 46

Table 3.2 Protocol of the diagnostic campaign 48

Table 4.1 Material properties of slab and girders estimated from NDTs 60

Table 4.2 Effects of dead loads g1 and g2 on girders T1, T2, T3, T4 60

Table 4.3 Three hypotheses on the mechanical properties of materials based on the results from the non-destructive tests 61

Table 4.4 Ultimate moment and shear resistance for each girder predicted by the structural model ANA1 63

Table 4.5 The updated value of residual stress $\sigma_{p,\infty}$ for each girder and hypotheses B and C implemented in ANA2 63

Table 4.6 The updated value of the residual stress $\sigma p,\infty$ and the elastic modulus Ec of the concrete for each girder implemented in FEM2 65

Table 4.7 Load test calendar with date and time of each loading and unloading phase. (*) of the following day 65

Table 4.8 Objectives, key parameters, and measured quantities defined to design the structural health monitoring system 67

Table 4.9 Measured quantity, location, performance, number, and other characteristics of sensors. (displ. = displacement) 68

Table 4.10 Non compensated (NC) and temperature compensated (TC) deflections, concrete strain, and crushing of bearings measured on the girder T1 during the loading phases P1, P2, and P3 73

Table 4.11 Errors without operating the temperature-compensation: e is the absolute value of the error, e/m is the relative value of the error, obtained by dividing the absolute value e with the non-temperature-compensated measurement m 73

Table 4.12 Peak frequencies of the first two vertical modes calculated before and after each loading and unloading phase 75

Table 4.13 Stiffness of each girder estimated through their trilinear idealised flexural response 76

Table 4.14 Loads corresponding to the change from state I to II and from state II to III of each girder 76

Table 4.15 Stiffness of each girder predicted by the structural models 78

Table 4.16 Loads corresponding to the change in the structural states predicted by the structural models 78

Table 4.17 Errors in the stiffness prediction. Error = (prediction – observation)/(observation of kI) × 100 [%] 79

Table 4.18 Errors in the load prediction. Error = (prediction – observation)/(observation of Load II – III) × 100 [%] 79

Table 5.1 Technical features of sensors installed on the viaduct (only sensors relevant in our analysis). 98

Table 5.2 Threshold, sampling frequency, high-pass filter, and time-parameters PDT, HDT, and HLT. 100

Table 6.1 Defect intensity scale to interpret RIMT outcomes and identify the presence of grouting voids and corrosion in the prestressing system. 124

Table 6.2 Spearman's Correlation Coefficient. (*) denoted SpearCC with confined reference sample at the cable anchored at the slab. 145

Table 6.3 Metrics comparison 146

CONTENT

Declaration of authenticity and author's rights **3**

Abstract **4**

Aknowledgment **5**

List of figures **6**

List of tables **12**

1 Introduction **18**

1.1 Aims and objectives. **20**

1.2 Thesis outline **20**

1.3 List of publications **21**

2 Literature review **24**

2.1 Management of ageing PT bridges **24**

2.1.1 Bridge collapse events: Italian case studies and global perspectives 25

2.1.2 Bridge Management Systems and guidelines 26

2.1.3 Visual inspections 28

2.2 Structural Health Monitoring (SHM) systems **29**

2.2.1 Acoustic Emission monitoring 29

2.2.2 Other SHM systems 31

2.3 Non-Destructive testing (NDT) and techniques for evaluation of the condition state of the post-tensioned concrete structures **33**

2.3.1 Digital Radiography (DR) 34

2.3.2 Ground Penetration Radar (GPR) 35

2.3.3 Reflectometric Impulse Measurements Test (RIMT) 37

2.3.4 Strand-Cutting Tests (SCT) 39

2.4 Load Testing for prestressed concrete bridges and viaducts **40**

2.5 Bayesian approach for bridge condition assessment and management **41**

3 The Alveo Vecchio Testbed 44

3.1.1 MIT Infrastructure Safety Test Field 45

3.1.2 Experimental campaign 46

4 Prestressed concrete bridge tested to failure: the Alveo Vecchio viaduct case study 50

4.1 Introduction 50

4.2 Case study – the Alveo Vecchio viaduct 54

4.3 Load test design 55

4.3.1 Load test protocol 55

4.3.2 Material properties 58

4.3.3 Prediction models 60

4.4 Load test execution 65

4.4.1 Calendar 65

4.4.2 Structural health monitoring system 66

4.4.3 Observed response 69

4.5 Discussion 75

4.5.1 Model prediction vs observed response 75

4.5.2 Errors in predictions 78

4.5.3 Load test utility for model updating 83

4.6 Conclusions 86

5 Structural Health Monitoring Based on Acoustic Emissions: Validation on a Prestressed Concrete Bridge Tested to Failure 89

5.1 Introduction 89

5.2 AE Principle and Observable Quantities 93

5.2.1 Phenomenon and Technology 93

5.2.2 AE Signal Parameters 94

5.2.3 AE Analysis for Load Tests 96

5.3 Case Study of a Prestressed Concrete Bridge Tested to Failure 96

5.3.1 Alveo Vecchio Viaduct 96

5.3.2 Structural Health Monitoring System 97
5.3.3 Load-Test Protocol 98
5.4 Results of the Case Study 99
5.4.1 Results from Displacement and Crack-Opening Transducers 100
5.4.2 Results from AE Sensors – P3 4800 kN 102
5.4.3 Results from AE Sensors – P4 7200 kN 104
5.5 Discussion of Results 105
5.5.1 Discuss of AE Results from P3 – 4800 kN 106
5.5.2 Discuss of AE Results from P5 – 7200 kN 107
5.5.3 Comparison of Results from P3 and P4 for Low Values of the Load (0–2400 kN) 108
5.6 Conclusions 109
6 Metrological validation of non-destructive testing methods for assessing the condition state of post-tensioned prestressing systems 112
6.1 Introduction 112
6.2 Case Study – The Alveo Vecchio viaduct 115
6.3 Experimental campaign 116
6.3.1 Experimentation setup 116
6.3.2 Non-destructive tests (NDTs) 118
6.3.3 Dissection of the prestressing system 124
6.4 Correlation analysis 130
6.5 Results 134
6.5.1 Interpretation of the NDTs outcomes 134
6.5.2 Condition state of the prestressing system 136
6.6 Correlation analysis 138
6.6.1 Condition state of the injected grout 138
6.6.2 Condition state of the steel wires 141
6.6.3 Summary 144
6.7 Discussion of the results 146
6.8 Conclusions 147

7 Conclusions 149

8 References 151

1 INTRODUCTION

Prestressed concrete (PC) bridges constitute a substantial portion of the existing bridge inventories worldwide, particularly favored for applications requiring long, slender spans since the 1950s [1]. Accurately assessing the condition of these bridges is paramount for infrastructure managers and engineers tasked with ensuring the safety and reliability of transportation networks. Specifically, bridges constructed using the Post-Tensioned (PT) concrete technique before the 1980s present significant concerns due to natural deterioration over time and increased traffic loads since their design [2]. In addition, these types of structures commonly suffer from loss of prestressing, which can generate extensive cracking and long-term deflections, resulting in a drop in service performance [3].

In the United Kingdom alone, over 2,000 PT structures support the Strategic Road Network (SRN) and roads managed by local authorities [1]. Similarly, approximately 90% of the 2,000 highway bridges in Italy are reinforced concrete or prestressed bridges built before 1980 [4]. The United States also relies heavily on bonded PT concrete construction for a significant proportion of its bridge inventory [5].

Despite their widespread use, PT bridges present ongoing challenges for asset maintainers due to the inaccessibility of the primary load-bearing elements—PT strands or tendons—often encased within grouted ducts involved in the concrete. Issues such as poor workmanship, inadequate water management, or inferior construction materials exacerbate concerns, potentially leading to tendon deterioration, structural cracking, and even catastrophic collapse [1].

The ageing of PT concrete bridges has become a pressing concern for infrastructure managers and regulatory authorities worldwide. As many of these structures have exceeded their expected lifespan, they have increasingly started to experience a range of issues affecting their performance and safety, including concrete degradation, steel corrosion, and loss of prestress, among others [6]. The ageing phenomenon is not confined to a specific geographical location but is a global issue. Statistics from diverse nations reveal a similar narrative: in the United States, 42% of bridges are at least half a century old, with an average age of 44 years, while in Japan, a quarter of bridges are of similar vintage, a figure set to rise to 52% by 2029 [7] [8]. Italy, too, suffers from the same problem, with over half of its highway bridges aged 50 or more, averaging 48 years [9].

The problem is exacerbated by rising traffic demands, characterized by increased vehicular numbers and weights, aggravating the load demands on these ageing structures and the risk of failure [7]. The extensive literature on risk assessment and bridge maintenance underscores the pivotal role of the condition of prestressing systems in maintaining the integrity and stability of prestressed concrete (PC) bridges [10] and the difficulties in accessing these for inspection.

In addressing the above challenges, effective monitoring and maintenance strategies are crucial to ensure structural safety and avert potential risks. Central to these efforts is a comprehensive understanding of the degradation processes, mainly focusing on the critical components of these bridges. Given the limitations of conventional investigation techniques and visual inspections, especially concerning PT structures, recourse to alternative monitoring and assessment methodologies is indispensable [11]. Non-Destructive Testing (NDT) methods and Structural health monitoring (SHM) can play a decisive role in facilitating informed decision-making regarding maintenance, repair, and reconstruction, optimizing bridge asset management, and safeguarding public safety. Many recent standards and guidelines, such as the Italian Guidelines for Risk Classification, Safety Assessment, and Monitoring of Existing Bridges [12] and Atkins [1], recommend recourse to these techniques to understand the structural state better.

Along with SHM systems and NDTs, load testing of existing dismissed bridges may be beneficial in understanding the residual capacity of PT bridges. They can also be very useful for calibrating and validating models for assessing the bridge's performance under service and extreme loading conditions. Many studies acknowledge the importance of load tests for bridge diagnosis [13], [14], [15]. These tests generally come in two forms: diagnostic load tests and proof load tests [14]. Diagnostic load tests involving loads lower than the design live load allow engineers to compare observed structural responses with predictions from a model, refining the model based on field results. On the other hand, proof load tests aim to verify whether a bridge can withstand prescribed live loads without distress. These tests cannot be carried out on a bridge in service, but the rising number of dismissed bridges offers the opportunity to perform tests up to failure.

In recent years, a proliferation of SHM and NDT techniques has been witnessed, accompanied by the increased availability of case studies for load testing. However, a fundamental question needs to be answered: How effective are these SHM and NDT techniques and load testing in gauging the actual health state of PT bridges?

This thesis aims to answer this research question by conducting a rigorous analysis of the empirical data obtained from an extensive experimental campaign performed on the Alveo Vecchio viaduct. This PT concrete viaduct, constructed in 1968 and dismissed in 2005, is representative of numerous bridges across the Italian highway network in terms of type, age, and deterioration state. In the last years, it has been used as a testbed for performing a series of experiments and tests, including comprehensive load testing up to failure, evaluation of SHM systems featuring Acoustic Emission (AE) sensors, and of NDT techniques, including Digital Radiography (DR), Ground Penetration Radar (GPR), and Reflectometric Impulse Measurement Test (RIMT).

1.1 Aims and objectives.

This thesis aims to evaluate the effectiveness of diagnostic tests for evaluating the state of PT concrete bridges. In particular, the main objectives of the study are:

- to assess the usefulness of load testing techniques for evaluating the performance of PT concrete bridges up to failure and validating the effectiveness of prediction models;
- to evaluate the effectiveness of acoustic emissions for monitoring the occurrence of limit-state conditions in PT concrete bridges;
- to quantify the effectiveness of NDTs for assessing the state of the PT system in concrete bridges.

The results of this study provide a significant contribution towards a better understanding of the performance of various diagnostic tools and prediction models that are used in current practice by bridge engineers and managers for assessing and managing a very critical structural typology.

1.2 Thesis outline

This thesis is structured into 7 chapters, presenting a comprehensive overview of the research's objectives and outputs.

Chapter 1 offers a general introduction to the research’s motivations and objectives.

Chapter 2 provides an extensive review of the current state-of-the-art in the field, starting with an outline of the management of ageing post-tensioning (PT) bridges worldwide and reviewing recent failures. The chapter proceeds to examine bridge management systems (BMSs) utilised by leading civil infrastructure operators, emphasising the strengths and

limitations of each system. Additionally, it discusses protocols prescribed by these systems, including the use of non-destructive testing (NDT), structural health monitoring (SHM) systems, and load tests to assess the condition of structures under analysis. Furthermore, it presents an exhaustive review of commonly used SHM systems such as Acoustic Emission (AE), Total Stations (TS), and accelerometers for dynamic monitoring, together with some prevalent NDT techniques like Digital Radiography (DR), Ground Penetration Radar (GPR), and Reflectometric Impulse Measurement Test (RIMT). The chapter concludes with an overview of load testing methods to enhance understanding of structural capacity.

Chapter 3 illustrates the Alveo Vecchio viaduct testbed. Information regarding its construction year, structural scheme, PT system, and current deterioration state are provided. Additionally, the chapter covers the research agreement that generated the transformation of the viaduct into a full-scale open-air laboratory, along with details of the ongoing experimental campaign.

Chapter 4 focuses on investigating the predictive capabilities of structural models and their alignment with load test results. It delves into what insights can be obtained from load tests to refine predictive models and enhance their accuracy concerning PT structural behaviour.

In Chapter 5, the effectiveness of the acoustic emission (AE) technique is investigated. The chapter analyses and discusses AE data recorded during a load test on an Alveo Vecchio span leading up to failure. It aims to discern patterns in AE data as load increases and compares these findings with data from other sensors installed on the structure. The objective is to evaluate whether AE monitoring can detect pre-existing damages, identify the start of cracks, determine maximum load capacity, and classify different types of damage.

Chapter 6 undertakes a metrological evaluation of Digital Radiography (DR), Ground Penetration Radar (GPR), and Reflectometric Impulse Measurement Test (RIMT) techniques for identifying defects in the PT system of concrete bridge girders. The study compares the outcomes of these NDT methods with observed defects during the autopsy of the PT system.

Finally, Chapter 7 presents concluding remarks, discussing the research outcomes and demonstrating achievement of predetermined aims. It also addresses the study's limitations and outlines potential routes for future research.

1.3 List of publications

Listed below are the journal papers (submitted or already published) that have stemmed from the research, with a description of my contribution:

1. Prestressed concrete bridge tested to failure: the Alveo Vecchio viaduct case study
   Tonelli, Rossi, Brighenti, Verzobio, Bonelli and Zonta
   Journal of Civil Structural Health Monitoring.
   Published 8 September 2022
   Contribution to this work: Tonelli and I actively participated in the experimental campaign to collect the essential data required for the analysis. Moreover, together with Brighenti, I conducted the literature review regarding the load tests and the proof load. All the authors provided feedback and reviewed the manuscript before the submission to the journal.
   Chapter 4 is based on this article.
2. Structural Health Monitoring Based on Acoustic Emissions: Validation on a Prestressed Concrete Bridge Tested to Failure
   Tonelli, Luchetta, Rossi, Migliorino and Zonta
   Sensors Journal
   Published 18 December 2020
   Contribution to this work: Tonelli and I actively participated in the experimental campaign to collect the essential data which this study is based on. Moreover, I conducted the literature review regarding the different Non-Destructive Tests and Structural Health Monitoring to evaluate the condition state of the prestressed concrete structures. All the authors provided feedback and reviewed the manuscript before the submission to the journal.
   Chapter 5 is based on this article.
3. Metrological validation of non-destructive testing methods for assessing the condition state of post-tensioned prestressing systems
   Rossi, Zorzi, Tonelli, Tubaldi and Zonta
   Structure & Infrastructure Engineering Journal.
   Under preparation
   Contribution to this work: Tonelli and I actively participated in the experimental campaign, collecting crucial data essential for our analysis. My responsibilities included directly mapping the actual condition state of the prestressing system within the concrete girders. This mapping aimed to quantify the level of defects and establish correlations with the outcomes of non-destructive testing methods conducted before dissecting the girders. Additionally, I conducted an extensive literature review on the

non-destructive testing methods employed. Furthermore, all authors contributed to refining the manuscript by providing feedback and critically reviewing the content. Chapter 6 is based on this article.

Other research outputs (conference papers) are:

1. Metrological Validation of Non-Destructive Testing Techniques for Assessing the Condition State of Pre-Stressing Systems
   Zorzi, Rossi, Tonelli, Lotti, and Zonta
   Proc. Structural Health Monitoring 2023
2. Comparison between model prediction and measured response of a prestressed concrete bridge tested to failure
   Rossi, Brighenti, Verzobio, Tonelli, Zonta, and Migliorino
   Proc. European Workshop on Structural Health Monitoring, 2022
3. Acoustic emission monitoring of prestressed concrete bridges: Differences before and after the first-crack opening
   Tonelli, Rossi, Luchetta, Zonta, Migliorino, Selleri, Valeri, Marchiondelli and Ascari
   Proc. CSHM-8 Workshop 8, 2021
4. Effectiveness of acoustic emissions monitoring for in-service prestressed concrete bridges
   Tonelli, Rossi, Luchetta, Caspani, Zonta, Migliorino, Selleri, Valeri, Marchiondelli and Ascari
   Proc. Sensors and Smart Structures Technologies for Civil, Mechanical, and Aereospace Systems 2021

2 LITERATURE REVIEW

This chapter explores the current state-of-the-art and fundamental concepts that form the backbone of the research. The first section provides an overview of the management practices concerning ageing of post-tensioned (PT) bridges on a global scale, coupled with a review of recent bridge failures occurred in Italy in the last ten years. This is followed by an analysis of bridge management systems (BMSs) employed by prominent civil infrastructure operators, highlighting their strengths and criticisms. Moreover, we delve into the protocols mandated by these systems, including the utilization of non-destructive testing (NDT), structural health monitoring (SHM) systems, and load tests to evaluate the structural condition under scrutiny.

The subsequent section provides an exhaustive examination of some of the widely utilized SHM systems, such as Acoustic Emission (AE) monitoring, and some of the prevalent NDT techniques like Digital Radiography (DR), Ground Penetration Radar (GPR), and Reflectometric Impulse Measurement Test (RIMT). The chapter concludes with an overview of load testing methodologies and their use for calibrating and validating modeling strategies.

2.1 Management of ageing PT bridges

The management of ageing post-tensioned (PT) bridges has emerged as a critical concern for infrastructure managers and engineers worldwide. Prestressed concrete bridges, a favored choice for long, slender spans since the 1950s, now constitute a substantial portion of bridge inventories globally [1]. However, bridges constructed using post-tensioned (PT) concrete techniques before the 1980s are particularly vulnerable to deterioration over time and increased traffic loads since their design [2]. Loss of prestressing in these structures is a common issue, often leading to extensive cracking and excessive long-term deflections, resulting in diminished service performance [3]. An extensive literature on risk assessment and bridge maintenance confirms the crucial role of PT system conditions in maintaining the integrity and stability of this kind of structure [10], [16].

PT structures are integral to transportation networks in various countries, including the United Kingdom, Italy, and the United States. For instance, over 2,000 PT structures support the strategic road network in the UK [1], while approximately 90% of highway bridges in Italy were constructed before 1980 [4]. Similarly, the United States relies heavily on bonded PT concrete construction for a significant portion of its bridge inventory [5].

Despite their widespread use, PT bridges pose ongoing challenges for asset maintainers due to the inaccessibility of primary load-bearing elements such as PT strands or tendons, often

encased within grouted ducts within the concrete. Issues such as poor workmanship, inadequate water management, or inferior construction materials can exacerbate concerns, potentially leading to tendon deterioration, structural cracking, and catastrophic collapse [1].

The ageing of PT concrete bridges has become a pressing global concern, as many of these structures have surpassed their expected lifespan, experiencing issues affecting performance and safety, including concrete degradation, steel corrosion, and loss of prestress [6]. This issue transcends geographical boundaries, with statistics from diverse nations indicating a similar narrative. For instance, 42% of bridges in the United States are at least half a century old, with an average age of 44 years [7]. In Japan, a quarter of bridges are of similar vintage, a figure set to rise to 52% by 2029 [8]. Italy faces a comparable challenge, with over half of its highway bridges aged 50 or more, averaging 48 years [9].

As civil infrastructure assets age, the investments required to maintain their performance and safety escalate, alongside the economic, environmental, and societal impacts of bridge failures [17], [18], [19]. Addressing the backlog of bridge repair needs is estimated at $125 billion in the USA in 2020 [7]. The American Society of Civil Engineers warns that without increased investment, necessary repairs will not be completed until 2071, with additional deterioration exacerbating the situation. Moreover, the closure of strategic bridges can result in significant time loss for drivers due to congestion and impose severe economic costs on national economies [7]. The problem is exacerbated by increasing traffic demands, characterized by rising vehicular numbers and weights, placing additional stress on ageing structures and increasing the risk of failure [7].

2.1.1 Bridge collapse events: Italian case studies and global perspectives

The collapse of the Polcevera Bridge, also known as the Morandi Bridge, in August 2018 in Italy, resulting in 43 fatalities, has raised significant concerns among bridge managers, infrastructure operators, and the general public, regarding the state of prestressing systems in bridges [19]. This tragic event stressed the imperative need for enhanced safety measures for Italy's ageing infrastructure. This encouraged the development of new guidelines for risk classification, safety assessment, and monitoring of existing bridges, particularly those over 50 years old that have yet to receive adequate maintenance. Even though most collapses in Italy have not been attributed to defects in prestressing systems, the frequent occurrence of bridge failures underscores the broader issue of ageing infrastructure in Italy. Italy has witnessed more than 10 collapsed bridges in the past decade alone. Among these incidents,

two notable cases reported by Clemente et al., 2020 [20] are worth mentioning: the collapse of the bridge between Annone and Cesana Brianza in October 2016 while a truck carrying steel coils was passing on it, and the sudden collapse of the viaduct on the Fossano ring road in April 2017, occurring in the absence of any travelling loads. In Fareti et al. 2023 [21] the collapse of another Italian bridge in the last ten years is reported as a case study: the Albiano-Magra Bridge. This was a reinforced concrete road bridge that crossed the Magra River and connected the two small towns of Caprogliola and Albiano at the border between Italy's Liguria and Tuscany regions. On 8 April 2020, the Albiano-Magra Bridge collapsed in a reduced traffic regime due to the restrictions resulting from the Covid-19 pandemic. Fortunately, the failure involved only two vehicles and caused no fatalities.

These events illustrated above serve as poignant reminder of the critical need for comprehensive assessment and maintenance strategies for ageing bridges, not only in Italy but also globally.

2.1.2 Bridge Management Systems and guidelines

Bridge management system (BMS) is defined as a set of components that aims to the successful management of a civil asset. Technical literature reports several examples of BMS: Zonta et al., 2007 [22] describe the BMS of a small-sized transport agency, the Department of Public works of the Autonomous Province of Trento. The system operates on the web and includes a section for condition state evaluation, safety assessment and prioritisation of interventions [23]. Condition appraisal is based on visual inspections and acknowledges the general rules of the AASHTO, 1997 [24] Commonly Recognized Standard Element system.

As described before, a very important segment in a BMS is the assessment of infrastructure asset's conservation state. The DOMUS system (2014) [25], that is the system currently in use by "*Rete Ferroviaria Italiana*" RFI (i.e., the largest transporting public operator in Italy), proposes a codified methodology for the inspection visits with the purpose to create a database, that includes all the infrastructures and their conservation states. To this end, DOMUS uses the following fundamental elements: infrastructures database that contains different information such as the category of structures, structural components, and their defects. One of the problems of the inspection visits is the different judgment that the inspectors can have in their evaluations. The technical literature reports many examples that aim to resolve this critical aspect of BMS. "*Autostrade per l'Italia*" ASPI (i.e., the largest

highway operator in Italy) use SPEA catalogue, 2015 [26] to homogenise inspectors' judgement with a new common language of defect features. There are 103 different defects within the catalogue and, for each one, there is an ID card reporting critical information: defect number code, defect denomination, and related features. Each part of the bridges is identified, so it is possible to assign to each element one or more defects and their features.

The last significant component of a BMS is the prioritisation of the interventions to provide a score of structural reliability. Also, for this section the technical literature reports several techniques to satisfy this main purpose [22]. It is possible to observe that the system conservatively estimates the prior reliability of each bridge, basing on the sole inspection data. Where the condition of the bridge gives cause for concern, its reliability is evaluated in a more formal manner using multi-step procedures of increasing refinement. Decision-making is driven by a principle whereby priority is given to those actions that, within a specific budget, will minimize the risk of occurrence of an unacceptable event in the whole network.

Mirzaei et al. [27] analyses and compares numerous BMS, their main information and areas of improvement. The document is based on the completed questionnaires on 21 BMS, from 16 countries, used to manage approximately 980.000 objects. The report provides a general overview of the surveyed management systems. The conclusion emerging from the synthesis of the questionnaires is that a certain level of standardisation of the different BMS between managing agents could potentially enhance the exchange of knowledge and experience and improve the usefulness of management systems.

Specific standards and guidelines have been developed for post-tensioned concrete bridges. These efforts reflect a global commitment to enhancing these critical infrastructure assets' inspection, assessment, and management.

One notable publication in this domain is the American National Cooperative Highway Research Program (NCHRP) Research Report 848, released in 2017 [28]. Titled "Inspection Guidelines for Bridge Post-Tensioning and Stay Cable Systems Using NDE Methods," this report serves as a comprehensive guideline for bridge owners, offering insights into the selection of appropriate non-destructive evaluation (NDE) methods for assessing the condition of post-tensioning and stay cable systems.

Similarly, the British Standards for Highways introduced document CS 465, "Management of Post-Tensioned Concrete Bridges," in April 2022 [29]. This document outlines a systematic

process for conducting risk reviews, assessments, and management activities explicitly tailored to post-tensioned concrete bridges. By providing a structured approach, CS 465 aims to enhance the safety and reliability of these structures within the highway network.

In Italy, the Ministry of Infrastructures and Transport (MIT) published the "Italian Guidelines for Risk Classification and Management, Safety Assessment, and Monitoring of Existing Bridges" (LG20) [11]. These guidelines advocate for a multilevel approach to risk classification and contain a specific protocol for special inspections on existing post-tensioned bridges, given the critical nature of this kind of construction system. By prescribing investigation techniques, structural health monitoring systems, and load tests, the protocol underscores the importance of proactive management strategies to safeguard these vital assets.

Collectively, these initiatives underscore the global commitment to advancing the safety, resilience, and longevity of post-tensioned concrete bridges through robust standards, guidelines, and protocols tailored to address their unique characteristics and challenges.

2.1.3 Visual inspections

The maintenance and safety of bridges heavily rely on regular visual inspections, which are widely used as the primary technique for assessing the condition state of bridges worldwide [30]. They are crucial for identifying faults, defects, and deterioration early on, allowing for timely maintenance and preservation efforts to ensure the structural integrity of bridges and the safety of the travelling public.

However, the success of visual inspections depends on the ability of bridge inspectors to detect and report on the condition of bridge components accurately. Human reliability in visual inspections is subject to various factors, including inherent human fallibility and performance-influencing elements within the inspection process. Despite the critical importance of visual inspections, studies, such as the one conducted by Moore et al., 2000 [31] , have highlighted the importance of ensuring that inspection reports consistently meet the desired standards for quality and consistency.

One notable aspect highlighted by Clarke [32] is the impact of performance-influencing factors on the reliability of visual inspection reports. These factors, which may include aspects of the inspection environment, inspector experience, and inspection protocols, can significantly impact the accuracy and thoroughness of inspections. Moreover, inspectors'

belief in their ability to detect defects and reliance on visual inspection as the primary assessment method may contribute to overestimating the effectiveness of inspections.

Enforcing mandatory inspection programs, as expressed in the "Italian Guidelines for Risk Classification and Management, Safety Assessment, and Monitoring of Existing Bridges" (LG20) [11], underscores the acknowledgement of the crucial role regular inspections play in maintaining bridge safety. These programs were initiated in response to past bridge failures, emphasizing the need for proactive measures to mitigate risks associated with ageing infrastructure, lack of maintenance, and increasing traffic volumes and loads.

There is a growing realization that the emphasis must shift from simply conducting inspections to assessing the reliability of inspection procedures and establishing confidence in inspection results. This shift requires a comprehensive evaluation of inspection methodologies, the developing standardized protocols, and incorporating advanced technologies to augment human inspection capabilities. By addressing these challenges, bridge owners and regulatory authorities can enhance the effectiveness of visual inspections and ultimately improve the maintenance and safety of bridges for the benefit of the travelling public [30].

2.2 Structural Health Monitoring (SHM) systems

Structural Health Monitoring (SHM) systems present a solution to overcome the limitations of visual inspections and enhance the understanding of a structure's condition. Broadly, SHM systems utilize sensors to achieve timely and dependable diagnosis of the condition state of structural components or the entire structure. Compared to visual inspections, the primary advantage of SHM systems lies in their ability to offer objective and quantitative insights into the monitored structure [33].

Additionally, they provide continuous data on the structural state, even in extreme events.

The next subsections illustrate various SHM systems developed and implemented for assessing in real time the state of prestressed concrete bridges, with a particular focus posed on acoustic emission (AE) monitoring systems.

2.2.1 Acoustic Emission monitoring

The Acoustic Emission (AE) technique represents a passive monitoring approach crucial for detecting elastic waves within prestressed concrete structural components, indicative of damages such as crack initiation, propagation, and the failure of steel wires or bonds [34].

This non-invasive method aims to detect, locate, and assess damage intensity, making it applicable both during a structure's service life and load testing scenarios. While AE monitoring saw its inception in fields like aerospace, its application in Structural Health Monitoring (SHM) began later but has garnered significant interest due to its ability to detect damages in otherwise inaccessible areas [34].

Numerous laboratory studies on crack detection based on AE have been conducted on specimens representative of in-service structures, both on steel members [35], [36], [37] and concrete samples [38], [39], [40]. In addition, field-testing applications have been carried out on large-scale structures, such as bridges, nuclear power plants, containment structures like silos, bins, and water storage tanks [41], and prestressed concrete pipes exposed to corrosion phenomena [42]. Applications of AE for damage monitoring in masonry structures are also reported in the literature [43].

The use of AE in bridge monitoring traces back to the 1970s, when it was first employed to assess a portable military bridge during proof testing [44]. Subsequent experiments have applied AE technology in various field bridge testing scenarios, addressing issues such as concrete crack detection, fatigue crack development in steel members, and failure of prestressed tendons [45]. Comprehensive reviews have outlined its applications on bridges from 1970 to 2010 [45].

Researchers have utilized AE monitoring for safety assessments of different bridge types, including reinforced concrete, prestressed concrete (both post-tensioned and pre-tensioned), and steel-concrete composite bridges [46]. The method has proven effective in evaluating bridge integrity despite the caveat that specific evaluation criteria must be established for each structural type [46]. Other studies have focused on AE's role in identifying and classifying crack extensions during load tests [47].

Numerous experiments have targeted crack opening and propagation in concrete elements, often comparing AE results with traditional crack-opening sensors and finite-element-model predictions [48]. Recent endeavours have even integrated machine learning algorithms to assess crack-opening rates in prestressed concrete structures, yielding promising correlations between AE parameters and crack events under different loads [49].

AE monitoring has also been instrumental in detecting wire breaks in prestressed concrete bridges, with studies demonstrating its efficacy in wire break localization and detection accuracy [50], [51]. Moreover, investigations into corrosion in prestressed concrete

components have validated AE's efficiency in evaluating and detecting corrosive phenomena [52].

In summary, while AE techniques have been extensively validated in laboratory conditions and on individual structural elements, their performance on full bridges nearing collapse remains an area of ongoing research. While experimental verifications typically focus on damage states that do not threaten bridge safety directly, there is a need for further exploration into AE's potential as an early warning system for bridges approaching their ultimate state.

2.2.2 Other SHM systems

In the field of structural health monitoring (SHM), various types can be applied to structures in operation to monitor their behavior [53]. Of the many, the system of Total Stations (TS) to record anomalous displacements and the system of accelerometers to check vibration modes are among the most widely used.

TS combine electronic distance measuring devices (EDM) with electronic theodolites; modern TS offers efficient and accurate measurement solutions for assessing the positions or heights of points within a structure [53]. Initially developed for precise surveying applications, TS offers high accuracy, long-range measurement capabilities, and the ability to track movements and deformations with exceptional precision [54]. The functionality of a TS is embedded in its ability to measure both vertical and horizontal angles using the theodolite. At the same time, electronic distance measuring (EDM) utilizes electromagnetic waves to determine the slope distance to a target or prism [55]. The measured time interval of light signals reflected from the prism is utilized to calculate distances, with typical TS boasting an accuracy of about 2 mm for distances up to 2000 m [55]. Moreover, the accuracy of total stations in detecting vertical displacements has been reported to be as precise as ±0.1 mm [56], [57]. Despite their ruggedness and widespread commercial availability, total stations have limitations. Data gathering can be time-consuming, and the equipment is susceptible to vibrations and environmental conditions, which may impact measurement accuracy [53].

In SHM for prestressed concrete structures, TS has garnered significant attention due to its ability to capture subtle changes in structural behaviour and identify potential issues before they lead to critical failures. Palazzo et al., 2006 [58] investigated the use of Robotic Total Stations (RTS) for monitoring the deflection and deformation of prestressed concrete bridges under varying loads and environmental conditions. Their study demonstrated that RTS

provided accurate and reliable measurements, empowering engineers to comprehensively assess the structural health of bridges and make well-informed decisions regarding maintenance and repair strategies. Overall, the integration of TS into SHM systems offers promise for enhancing the monitoring and maintenance of prestressed concrete structures, contributing to improved safety, longevity, and resilience of civil infrastructure.

Even the accelerometers play a pivotal role in the field of SHM, providing essential insights into the dynamic behavior of various structures. These sensors measure acceleration along one, two, or three axes and are instrumental in understanding the effects of vibrations and external forces on structural integrity [53]. Accelerometers come in various types, each with its unique mechanisms and advantages. Piezoelectric accelerometers emerge as the most prevalent choice due to their efficiency and widespread commercial availability. These sensors are designed to generate electrical signals proportional to the forces induced by structural vibrations [59]. Common materials in piezoelectric accelerometers include quartz and lead zirconate titanate, which exhibit desirable properties for converting mechanical energy into electrical signals. Notably, piezoelectric accelerometers boast impressive resolution, with measurements capable of reaching up to 0.0001 g [60]. The adoption of piezoelectric accelerometers is driven by their affordability, accessibility, and ease of installation. Their widespread commercialization has made them indispensable tools in dynamic analysis and SHM. However, despite their advantages, interpreting accelerometer measurements for structural dynamic analysis can be intricate. Factors such as nonlinear temperature influences pose challenges in accurately assessing structural health indicators [53].

Recent studies have demonstrated the efficacy of dynamic monitoring in examining prestressed concrete structures. For instance, Wei-Hua et al. 2020 [61] implemented statistical pattern recognition (SPR) technology to conduct vibration-based SHM of an ageing prestressed concrete highway bridge to track its deterioration over 14 years from 2000 to 2013. The study elucidated the significant impact of temperature variations on structural frequencies. By mitigating nonlinear temperature influences, the research elucidated the correlation between the loss of prestress in prestressed tendons and alterations in statistical health indicators of the analyzed structure. In summary, using accelerometers for dynamic analysis presents a promising avenue for understanding the behavior of various structures, with particular relevance in examining prestressed concrete structures. Despite challenges in

interpretation, advancements in technology and methodologies continue to enhance the efficacy of accelerometer based SHM.

2.3 Non-Destructive testing (NDT) and techniques for evaluation of the condition state of the post-tensioned concrete structures

Non-destructive testing (NDT) techniques are pivotal in assessing material decay and monitoring the structural condition state of in-service structures [62]. The increasing interest in diagnostic techniques within infrastructure operations, coupled with recent technological advancements, has fueled the exploration and development of innovative monitoring methodologies, with a particular focus on post-tensioned concrete structures [63]. Notable techniques include Ground Penetration Radar (GPR) [64], [65], Reflectometric Impulse Measurement Technology (RIMT) [66], [67], [68], Time Domain Reflectometry (TDR) [69], [70], Strand-Cutting Test (SCT) [71], [72], [73], Core Drilling Method (CDM) [74], [75], and Digital Radiography (DR) [76], [77], [78]. While these methods have undergone laboratory experimentation and field monitoring, the lack of standardized procedures and the necessity for expert interpretation have hindered their widespread application in civil infrastructure.

Among them, various NDT methods are commonly employed to assess the condition state of post-tensioned (PT) systems. A study commissioned by Highway England outlines prevalent NDT techniques for investigating PT structures, delineating their strengths, weaknesses, and primary applications [1]. Ground Penetration Radar (GPR) is predominantly utilized to identify the path of prestressing cables and potentially detect grouting voids within non-metal ducts. Impact Echo (IE) exhibits promise in identifying grouting voids within metal ducts. Digital Radiography (DR) excels in pinpointing defects in grout and tendons with high precision. Ultrasonic Tomography (UT) is leveraged to detect tendon corrosion, assess bond quality, and identify grouting voids within ducts. Moreover, research by S. Hurlebaus et al. suggests the value of combining multiple NDT techniques to enhance diagnostic capabilities [28].

This research work focuses on three prominent NDT techniques: Digital Radiography (DR), Ground Penetration Radar (GPR), and Reflectometric Impulse Measurement Test (RIMT), which have gained traction and are increasingly recommended for non-destructive assessment of PT bridges. DR employs X-rays to inspect internal material structures, effectively detecting grouting voids, cable breaks, and concrete defects in PT structures [76], [77], [78]. GPR relies on electromagnetic energy reflections to locate cables and reinforcement in PT structures [79]. RIMT generates high-frequency electromagnetic pulses along PT cable wires

and analyzes the reflected signal to detect corrosion pits, wire breaks, and grouting voids within ducts. While RIMT is not universally recognized as an effective NDT method for prestressing system assessment, its potential merits further exploration [68], [80].

2.3.1 Digital Radiography (DR)

A testing technique based on Digital Radiography (DR) has already been successfully applied in civil engineering for tasks such as scanning steel pipelines (Haith MI, 2016 [81] and Silva W. et al., 2021 [82]) and investigating corrosion issues (Beck M. et al., 2010 [83] and Lim S et al. 2019 [84]) have recently been developed and employed to assess the actual condition of cables with promising results. This innovative approach allows for the rapid acquisition of high-resolution two-dimensional images of the internal structures within the investigated components, presenting encouraging prospects for non-destructive inspections of prestressed concrete bridges. As reported by Innocenzi R. D. et al., 2022 [77], the DR technique relies on the interaction of ionized radiation with a body positioned between an emitting source and a receiver, followed by the processing of data through a tablet equipped with specialized software capable of acquiring, processing, and storing images in real-time. Radiation encompasses the transmission of energy in the form of photons associated with the propagation of electromagnetic waves, such as X-rays and γ-rays, as well as kinetic energy associated with the high speed of charged particles, such as α-rays, β-rays, protons, neutrons, and ions. As radiation traverses a material, it may be absorbed, diffused, or transmitted. The degree of absorption follows an exponential law, dependent on the thickness and density of the penetrated material. The attenuated radiation ultimately reaches the panel receiver behind the examined object, where a portion of the passing energy is captured. This results in a radiographic image portraying a faithful representation of the object in a negative form.

Figure 2.1 depicts a radiography acquisition of an object investigated affected by a defect. Defects in the object, such as cavities or cracks, will be less absorbent than the surrounding material. As a result, darker spots will appear on the receiver, corresponding to the severity of the defect. Conversely, lighter spots will indicate the presence of more absorbent elements, such as reinforcing bars or post-tensioned cables.

In the context of prestressed concrete (PC) structures (Verma et al., 2013 [78] and Rehman et al., 2016 [76]), DR holds promise in detecting various anomalies, such as grouting voids in metal ducts, cable breaks, and defects within concrete components. The technique's ability to distinguish between different materials and highlight areas of interest, such as cavities or

cracks, is instrumental in assessing structural integrity and identifying potential areas of concern.

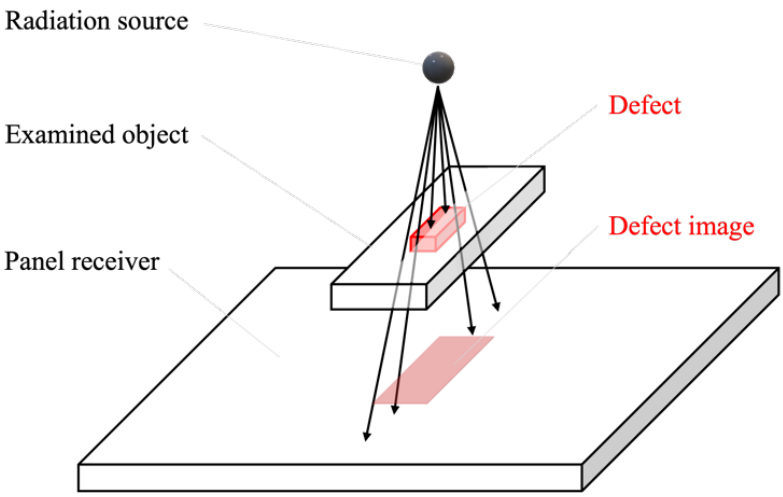

Figure 2.1 Radiography acquisition of an object investigated affected by a defect.

DR's effectiveness depends on several critical parameters, including the penetrating power of the radiation, the energy spectrum emitted by the source, the thickness of the object under examination, and the material composition. Additionally, factors such as exposure time and the relative distances between the source, object, and receiver play crucial roles in ensuring optimal image quality and diagnostic accuracy.

Moreover, recent advancements in DR technology have facilitated the development of portable and user-friendly devices, enabling onsite inspections of prestressed structures with greater convenience and efficiency. These advancements have opened up new possibilities for routine inspections and maintenance activities, allowing engineers to monitor the condition state of critical infrastructure assets more effectively.

In summary, DR significantly advances NDT techniques for prestressed structures. Its ability to provide detailed imaging of internal structures and its versatility and efficiency positions it as a valuable tool for engineers tasked with evaluating the condition state and ensuring the safety and reliability of critical infrastructure assets. Ongoing research and development efforts are essential to refine DR methodologies further and maximize their effectiveness in structural engineering.

2.3.2 Ground Penetration Radar (GPR)

Ground Penetrating Radar (GPR) is a technique employed in civil and structural engineering for rapidly assessing various characteristics of concrete structures. By utilizing high-

frequency electromagnetic waves, GPR provides continuous evaluations of concrete elements by relying on the reflection of these waves from boundaries with varying dielectric constants within the material (Rehman et al., 2016 [76]).

The operational principle of GPR revolves around the transmission and reception of radar signals via a transducer or antenna. Short pulses of high-frequency electromagnetic energy are emitted into the concrete structure under examination. As these pulses propagate through the material, they encounter changes in dielectric constants, leading to partial reflection. By analysing the transit time from the initiation of the pulse to the reception of the reflected signal and considering the velocity of wave propagation, GPR determines the location and depth of these dielectric constant boundaries. The depth of these boundaries is directly proportional to the transit time, providing crucial information about the internal structure of the concrete. Figure 2.2 depicts the working phases during a GPR acquisition.

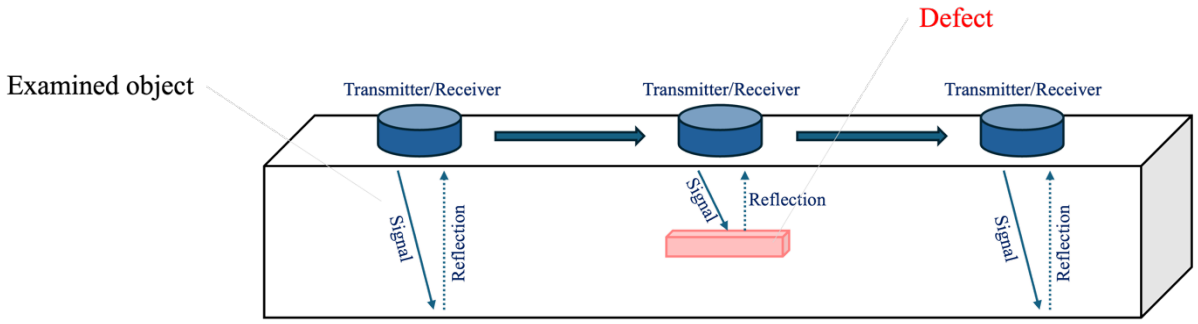

Figure 2.2 Georadar acquisition of an object investigated affected by a defect.

GPR is a radar imaging technique that involves emitting electromagnetic pulses from an antenna, and receiving reflected pulses from internal reflectors within the scanned medium, which are in turn caused by changes in the materials' electrical conductivities (reinforcement, tendon ducts and voids) [85]. This technique has been widely adopted for a number of purposes related to NDT of post-tensioning systems, as the system is comparatively inexpensive, quick to deploy through lightweight, compact scanners and high-speed in return of results. The usage and effectiveness of GPR for the inspection of post-tensioning ducts is mixed within the available literature, often due to the specifics of the structure and the material makeup being scanned. Where the ducts are non-metallic, there are examples of GPR being used to detect voids within internal ducts. However, factors such as high-density concrete or metallic ducts can render the system difficult to obtain reliable readings, and generally cannot be used even in optimum situations to determine strand corrosion or depth and size of duct voids.

In summary, in many cases GPR's use may be limited to identification and location of the post-tensioning ducts; However the usefulness of this system for this purpose alone should not be underestimated – many of the NDT techniques available require the precise location of the ducts to be known to be effective, and as such GPR can be a powerful tool when used in combination with others, particularly given that is it is typically unaffected by the presence of reinforcement meshes [86] [79].

2.3.3 Reflectometric Impulse Measurements Test (RIMT)

The RIMT method operates on the principle of high-frequency electromagnetic wave propagation and reflection. This diagnostic technique begins with generating an electromagnetic pulse by a transmitter, the primary device. The measurements are carried out by emitting voltage pulses of concise duration (ranging from 10 ns to 1 ms) at one end of the cable and detecting the reflected impedance signals at the same point. These reflected signals are complex, consisting of two components: one inductive type, characterised by an overall negative slope and associated with cable corrosion phenomena, and the other capacitive type, exhibiting an overall positive slope and linked to injection deficiency phenomena. Figure 2.3 depicts the working phases during a RIMT acquisition.

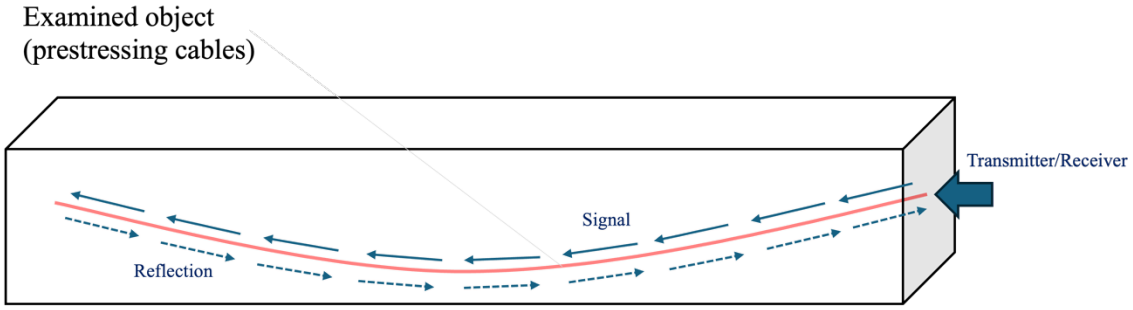

Figure 2.3 Reflectometric acquisition of an object investigated affected by a defect.

The resulting waveform trends are displayed on a desktop screen, stored on a computer, and subsequently processed in the laboratory by an expert operator. This analysis provides information regarding the location, type, and severity of any detected faults along the cable. Specifically, the analysis of impedance signals enables the assessment of the type, importance, and location of faults as follows:

- Type of fault: By determining the impedance components (inductive and capacitive)
- The magnitude of the fault: measuring the signal's derivative and amplitude.

- Distance L from the measuring head: Using the relationship $2L = V \cdot t$ where V represents the propagation speed of the wave and t denotes the time delay between the emission and reception of the pulse.

Numerous authors, including Pernica and Rahman, 1997 [67], have examined the effectiveness of the RIMT method. In their experimental endeavours in Canada, conducted under the auspices of the Institute for Research in Construction (IRC) and the National Research Council (NRC), the RIMT's performance was evaluated. The study involved the analysis of three distinct prestressed concrete structures, denoted as structures A, B, and C. A total of 86 tendons were subjected to investigation using the RIMT technique. In Building A, seven new tendons were stripped of their ducts and prepared with artificial defects for testing.

Additionally, six tendons were scraped and cut at different locations along the length. The remaining 69 cables were investigated in their natural states without any alterations. Defects identified through the RIMT method and inspection visits were independently classified on a 5-degree scale, correlating each degree with a percentage reduction in the cross-sectional area of the tendon. Notably, the study provided defect localisation with a resolution of ± (0.5+0.005L) m, where L represents the estimated distance of the defect from the probing end. However, despite these efforts, the results were not satisfactory. The RIMT method failed to identify 158 anomalies detected during inspection visits. Of particular concern, 83 anomalies were detected in tendons deemed completely healthy by RIMT, while inspection visits identified 68 anomalies, 49 of which went undetected by RIMT. Similar discrepancies were observed in the study by Matt, 2001 [68].

Given these results, the research progress has recently experienced a slowdown, mainly due to the discouraging results obtained from this non-destructive test compared with inspection visits.

More recently, investigations utilising the RIMT method were conducted on the Morandi Bridge in Genova, Italy, known as the Polcevera Viaduct, before its collapse in 2018. The method was employed to assess the condition of the stays and the potential presence of voids within the metal duct. However, in the report by Mortellaro et al., 2018 [87], incongruities between RIMT results and inspection visits were noted. The RIMT underestimated the extent of problems associated with the reduction in the cross-sectional area of the tendons.

2.3.4 Strand-Cutting Tests (SCT)

The Strand-Cutting Test (SCT) is a pivotal method used in assessing pre-compression stress within structural elements strands or tendons, particularly crucial in evaluating the condition state of the prestressed concrete structures. It is a diagnostic test that provides insight into the state of internal stress within these structures, determining their structural integrity and informing decisions regarding maintenance, rehabilitation, or further construction.

The SCT procedure entails a series of meticulous steps to ensure accurate analysis. Initially, the concrete cover and the duct encasing the cable under examination are carefully removed from a specific section, allowing access for analysis. Subsequently, macrostrain sensors are meticulously installed on the cable wire, enabling precise strain measurements. Following this, the wire is cut, and its relaxation behaviour is recorded, providing data regarding the pre-compression stress acting on the cable.

In the extensive body of literature surrounding the SCT, its categorisation as either a semi-destructive or destructive test remains controversial among researchers. While some consider it a semi-destructive test due to its invasive nature yet potential for continued structural functionality [72], [73], others view it as destructive, given its alteration of the tested material [71], [88], [89]. However, regardless of its classification, the SCT occupies a significant place within the "strain methods" field and finds wide-ranging applications in both research and practical engineering settings.

The pioneering work of Shenoy and Frantz, 1991 [90] laid the groundwork for subsequent research, although their initial attempts at employing the SCT did not yield satisfactory results. Nevertheless, this setback prompted further investigation by subsequent researchers, who aspired to refine the methodology and understand its limitations and capabilities more comprehensively.

For instance, Halsey & Miller, 1996 [88] conducted a comparative study, pitting the SCT against methods reliant on cracking re-open load and first crack moment calculation (Mcr). Their findings revealed slight differences in results, suggesting potential sources of error within the SCT methodology.

Similarly, subsequent studies by Labia et al., 1997 [91] and Baran et al., 2005 [71] further explored the efficacy of the SCT in comparison to alternative methods. Labia et al., 1997, validated theoretical models using experimental data obtained through the SCT, highlighting its utility in assessing pre-compression strength. Meanwhile, Baran et al., 2005, emphasised

the importance of visual observations alongside SCT results, underscoring the need for comprehensive analysis in structural evaluation.

In a later study by Czaderski & Motavalli, 2006 [73], the SCT was applied to ageing beams from the Cantine a Campolago Viaduct in Switzerland, producing promising results regarding its reliability. However, the study also identified challenges in interpreting SCT data, particularly concerning discrepancies among results from different locations along the beams.

In conclusion, while the SCT offers invaluable insights into pre-compression stress within prestressed concrete structures, its application necessitates careful consideration of various factors, including methodology, interpretation, and validation against alternative techniques. Continued research and refinement of the SCT methodology are essential for its ongoing utility in structural assessment and maintenance.

2.4 Load Testing for prestressed concrete bridges and viaducts

Load tests serve as essential tools for calibrating prediction models and assessing the performance of existing bridges and viaducts [13], [14], [15]. These tests are typically categorized into two types: diagnostic load tests and proof load tests. Diagnostic load tests involve applying loads lower than the design live load, allowing engineers to compare the observed response of the structure with model predictions and update the model accordingly [14]. Conversely, proof load tests aim to verify whether a structure can withstand prescribed factored live loads without experiencing distress [14].

Diagnostic load tests are particularly suitable for in-service bridges, where damage should not occur during the test, thus allowing for observation of only the linear elastic response. However, due to non-linearities and stress redistribution, the structure's response to service loads may not accurately reflect its behaviour under higher loads [14]. Collapse tests, though informative about a bridge's non-linear behaviour and ultimate capacity, result in the dismissal of the structure post-test.

A comprehensive analysis of several studies reveals key insights: firstly, the correlation between model predictions and load test results is generally strong for linear elastic responses but diminishes significantly after the initiation of the first crack [92], [93], [94], [95]. Moreover, observed ultimate capacities often deviate from model predictions due to factors such as shear failure or conservative estimates by models [92]. Secondly, discrepancies between predicted and observed capacities can stem from inaccuracies in geometric representations, boundary conditions, and material properties [93] [92]. Field factors like

diaphragm action, parapet stiffening, and concrete hardening, typically overlooked during design stages and structural modelling, can influence a bridge's capacity [93]. Environmental conditions and material ageing further contribute to structural deterioration, impacting load-carrying capacities [96].

Furthermore, the accuracy of predictions depends on the structural analysis method employed. Refined non-linear finite element (FE) models have been shown to reproduce actual structural behaviour closely and predict load-carrying capacity with high accuracy [15] [94]. However, standard linear elastic analyses often underestimate ultimate loads [94].

Sensitivity analyses reveal that small changes in model parameters can significantly affect predictions of elastic response, load-carrying capacity, and failure mechanism [15] [93]. The most influential parameters include concrete compressive and tensile strength, elastic modulus, residual stress in prestressing cables, and boundary conditions at supports.

In summary, load tests provide invaluable insights into the behaviour and capacity of bridges and viaducts, highlighting the importance of refining prediction models and accounting for various factors affecting structural performance. Future research should focus on refining analytical techniques, incorporating more accurate material and environmental data, and improving the understanding of complex non-linear behaviours to enhance the reliability of load test predictions and ensure the safety and longevity of civil infrastructure.

2.5 Bayesian approach for bridge condition assessment and management

The Bayesian approach provides a logical framework for incorporating data from inspections, visual inspections, SHM systems, NDT techiniques and load testing into bridge management and thus supporting the decision-making process.

Recent studies have explored frameworks for SHM-based decision-making, such as the work by Zonta et al. (2014) [97] on a pedestrian bridge at Princeton University equipped with a fibre optic sensing system and Tonelli et al. (2017) [98] proposing a decision support system for the Colle Isarco Viaduct in Italy. Additional examples can be found in Flynn and Todd (2010a, 2010b) [99] [100], Flynn et al. (2011) [101], and Cappello et al. (2016) [102].

Zambon et al. (2019) [103] proposed a Bayesian method for Condition Prediction of Existing Concrete Bridges combining Visual Inspection and Analytical Models of Deterioration.

Another study from Ma et al., 2014 [104] proposes a Bayesian framework for predicting the remaining capacity of reinforced concrete bridges. The framework exploits data from in situ

load testing to update the knowledge of the corrosion state in the reinforcement and update the estimate of the bridge load carrying capacity.

Bayesian approaches can also be used to update knowledge of the bridge state based on information gained using NDT. Mazzatura et al., 2024 [105] employ a Bayesian approach to establish Probability of Detection (PoD) curves for Ultrasonic Tomography (UT), an often utilized NDT technique for detecting voids in post-tensioning ducts. This method is employed to assess its real-world effectiveness.

Regardless of the type of information available, the process of managing a bridge typically comprises two steps: judgment and decision-making. First, based on available data, the structural state (S) is inferred. Then, the optimal action (a_{opt}) is chosen using knowledge of the structural state. The structural state represents the structure's condition, which may exist in various probabilistic states (e.g., severely damaged, moderately damaged, not damaged). An interpretation model is employed to assess the structural state based on observations, considering uncertainties. Actions available to the decision-maker may be discrete (e.g., do nothing, limit traffic, close the bridge) or continuous (e.g., adjust maintenance frequency). Taking an action produces measurable outcomes, such as monetary gains or losses, downtime, or casualties. The outcome of an action depends on both the action and the structural state.

The decision model aims to determine the most suitable action based on the outcome and knowledge of the structural state acquired through one or a combination of diagnostic tests. This process relies on rational decision-making principles encapsulated in the Expected Utility Theory (EUT), initially proposed by Von Neumann and Morgenstern, 1944 [106] and later refined by Raiffa and Schlaifer, 1961 [107]. EUT is extensively discussed in various modern textbooks, with Parmigiani and Inoue, 2009 [108] being recommended sources.

To select the optimal action using EUT, three key elements must be considered: the probability of the structural states determined through Bayesian inference, denoted as $P(S_i)$; the assessment of the outcome z, typically comprising both direct and indirect costs (i.e., consequences); and the decision maker's risk tolerance, often characterized by a utility function U.

Specifically, when the structural state S is deterministically known with certainty, a rational decision maker prioritizes actions based on their consequences z using a utility function $U(z)$. Mathematically, the utility function transforms the multidimensional outcome vector z

into a single scalar value U, representing the decision maker's subjective preference for each potential outcome. When the structural state S is uncertain, and therefore, the consequences of an action are only probabilistically understood, EUT suggests that decision makers prioritize their preferences based on the expected utility u, which is defined as:

$$u(a) = E_S[U(z(a,S))] \tag{2.1}$$

Where E_S represents the expected value operator of the random variable S, which is assumed to be the sole source of uncertainty in the problem. To clarify the notation, U indicates the utility function, while u denotes an expected utility. In essence, if each state S has a probability $P(S_i)$ and yields an outcome $z(a_j, S_i)$ when action a_j is taken, the expected utility $u(a_j)$ of a specific action a_j is evaluated as follows:

$$u(a_j) = \sum_{i=1}^{N} U(z(a_j, S_i))P(S_i) \tag{2.2}$$

Thus, following the principles of EUT, the decision maker will select the action a_{opt} that offers the highest expected utility payoff u:

$$u = \max_j u(a_j) \quad a_{opt} = \arg\max_j u(a_j) \tag{2.3a,b}$$

3 THE ALVEO VECCHIO TESTBED

The Alveo Vecchio viaduct is part of the old track of the A16 Italian Highway. It was built in 1968 and decommissioned in 2005 after being struck by a landslide. It represents 52% of the Italian highway bridges in terms of structural type, age, and deterioration. The viaduct consists of two structurally independent decks, one for each carriageway, each made of three 32.5 m-long simply supported spans, with a slight slope of around 1.45%. Each span consists of four 2 m-high PC girders supporting a 20 cm-thick concrete slab. Five equidistant reinforced concrete cross-girders connect the longitudinal girders, one at the centre, two at the end, and the remaining two between them. The bridge deck leans on fixed and free neoprene bridge bearings. Figure 3.1 shows a top view, a lateral view, and a cross-section of the viaduct. According to the design documentation [109], the prestressing was applied through 14 post-tensioned parabolic cables per girder, with an initial jacking tension of 1250 MPa. Each cable has an ultimate strength of 1700 MPa and a yielding strength of 1450 MPa. Fig. 3.2 shows transversal sections of the girders with the prestressing cables. The wall piers are 3.30 m high and have deep foundations consisting of eight bored piles 23 m long with a diameter of 1.2 m. The abutments are founded on six bored piles with a diameter of 1.20 m. Additional information about the structure is found in [109].

The viaduct is 50 km far from the sea and surrounded by countryside. The winter temperature hardly goes below 5°C; thus, the environment is not aggressive, and the viaduct is subject to limited use of de-icing salts. Visual inspections never reported signs of corrosion degradation, nor did we notice it in the steel specimens extracted for laboratory tests. In 2005, a landslide hit the C1sx and C1dx spans. It resulted in the collapse of span C1dx and the roto-translation of Pier 1. A preliminary visual inspection reported that the landslide did not affect spans C3sx and C3dx.

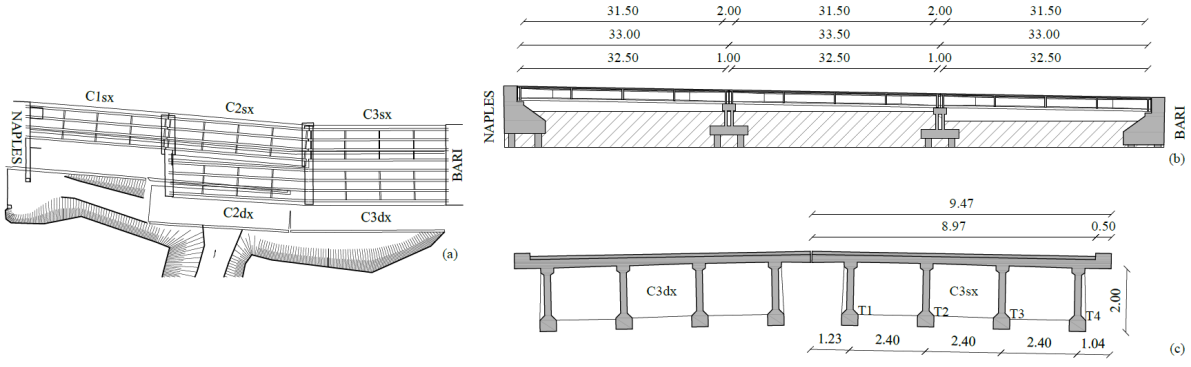

Figure 3.1 (a) top view; (b) lateral view; and (c) cross-section of the Alveo Vecchio viaduct (Italy)

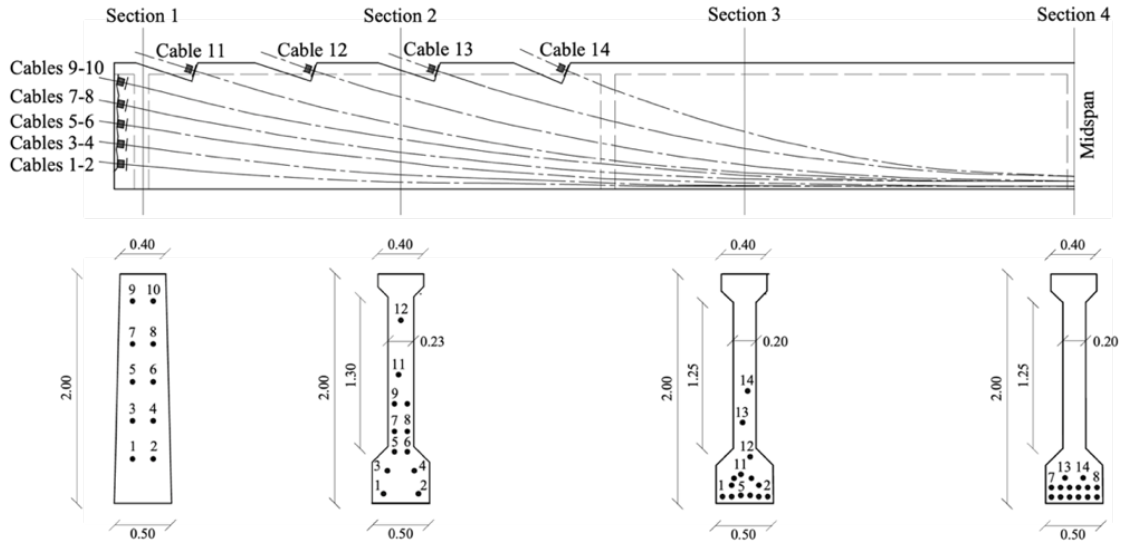

Figure 3.2 Longitudinal and transversal section of girders with post-tensioned cables

3.1.1 MIT Infrastructure Safety Test Field

Since June 2019, a research agreement has been active between the Italian Ministry of Infrastructure and Transport (MIT), Autostrade per l'Italia SpA (the principal operator of Italian highways), and the University of Trento (UniTN). This agreement concerns the management and monitoring of civil infrastructure, intending to develop survey protocols and monitoring systems to assess the safety and performance of existing highway bridges. It includes an extensive experimental activity that aims to validate the feasibility and effectiveness of methods for assessing the safety of existing bridges in actual conditions, including static and dynamic load tests and NDTs for the characterization of materials.

The MIT Infrastructure Safety Test Field was set up at the Alveo Vecchio viaduct: it is an open-air laboratory that provided a unique opportunity to perform a wide range of tests on a real bridge. The inaugural test comprised a load test up to the failure of an entire span, intending to evaluate the ultimate capacity of an isostatic span constructed in 1968 subject to routine maintenance. This test was conducted in conjunction with an extensive sampling and testing campaign performed following the Italian standard on Structural Health Monitoring (SHM) [110]. The aim was to quantify the materials' mechanical properties and assess the span's structural integrity. Table 3.1 reports the mechanical properties of materials resulting from the testing campaign.

Slab Concrete Compressive Strength	Girders Concrete Compressive Strength	Post Tensioned Cables Residual Stress	Steel Yield Strength	Steel Ultimate Strength
f_{cm} (MPa)	f_{cm} (MPa)	σ_{resm} (MPa)	f_{pym} (MPa)	f_{t1m} (MPa)
31.9	41.5	952	1509	1618

Table 3.1 Materials properties of the Alveo Vecchio viaduct.

The Alveo Vecchio test field was established under art. 14 of DL 28/09/2018, n.109, ("Genoa Decree") [111], which led to the release of an official document called "Italian guidelines for risk classification and management, safety assessment and monitoring of existing bridges" (LG20) [11].

3.1.2 Experimental campaign

As reported in Chapter 4 and in D. Tonelli, et al. 2022 [9], a proof load test was conducted in 2019 on an isostatic span (C3sx) of the viaduct to evaluate the actual load-bearing capacity of the structure, considering its representative state of degradation and routine maintenance. The applied load was concentrated to generate a bending moment in the midspan cross-section of the most stressed girder (externals) equal to the design bending moment. The yield state of the prestressing cables was reached at approximately four times the design load required by current Italian legislation [112], with a loading value of about 930 tons.

Before and after the proof load, identified as Phase 1, a series of Non-Destructive Tests (NDTs), Semi-Destructive Tests (SDTs), and Structural Health Monitoring (SHM) systems were conducted on the same span to characterize the structure's mechanical properties and investigate the condition of the prestressing system.

After completing various NDTs, SDTs and SHM systems, the decision was made to demolish the same bridge span. This demolition presented a unique opportunity to examine the prestressing system within the four reinforced concrete girders, essentially conducting an autopsy on the bridge structure. The objective was to assess the bridge's condition and quantify any defects within the metal ducts, injected grout, and steel cables.

Figure 3.3 shows photograph documentation acquired during the execution of the mapping activity of the three main component of the prestressing system embedded in the C3sx span's girders.

Figure 3.3 (a and b) Mapping activity of the actual condition state of a prestressing cable; (c) procedure adopted during the night; (d) 1 m long ruler positioned for mapping the condition state of the metal duct; (e) 1 m long ruler positioned for mapping the condition state of the injected grout and the steel cable.

The entire diagnostic campaign was divided into three distinct phases:

- Phase 2A: Evaluation of the effectiveness of NDTs, SDTs and SHM systems for the mechanical characterization of the structure and investigation of the prestressing system's conditions.
- Phase 2B: Proof load (both bending and shear) in displacement control on twin beams.
- Phase 2C: Dynamic tests with progressive imposed damage on span C3dx.

A consortium of universities, led by the University of Trento (UniTN), is carrying out the activities designed in this diagnostic campaign. The consortium includes the Polytechnic University of Marche (UniPM), the University of Naples Federico II (UniNa), the Sapienza University of Rome (UniRoma1), the University of Rome Three (UniRoma3), the University of Chieti and Pescara (UniCh), and the Polytechnic of Turin (PoliTO). University of Strathclyde was indirectly involved in the activities and signed a separate agreement for collaborative research with University of Trento.

Table 3.2 outlines the protocol of the experimental diagnostic campaign, which began with Phase 2A. In this phase, various Non-Destructive Tests (NDTs), Semi-Destructive Tests (SDTs), and Structural Health Monitoring (SHM) systems were implemented to assess the structure's condition. Subsequently, controlled demolition of the C3sx span was executed to extract the prestressing system from the four concrete girders and map its actual condition, with further details provided in Chapter 6.

Currently, two other phases are ongoing:

- Phase 2B involves load tests under displacement control using hydraulic jacks equipped with a pull system on twin girders taken from the C2sx span, tested in the same laboratory setup where the C3sx span was located. These load tests include both bending and shear assessments. The primary objective of this phase is to thoroughly

investigate the flexural capacity and shear resistance reserves of structures with similar characteristics to the Alveo Vecchio viaduct.

- Phase 2C will conduct vibrational tests on the C3dx span with progressive damage imposed at five levels. The damage levels range from the intact state of the structure to spalling without loss of cross-section, cutting of a single girder's prestressing cable, cutting one prestressing cable per girder, removing the ordinary reinforcement of a girder, and cracking of all girders. The principal purpose of this test is to investigate the different frequencies as a function of the varying states of health of the structure.

Phase	Purpose of the phase	NDTs – SDTs – SHM systems	Operator
Phase 1	Proof load up to the failure	Ground Penetration Radar (GPR) Acoustic Emission (AE) Strand-Cutting Test (SCT) Core Drilling (CD)	UniTN
Phase 2A	Evaluation of the metrological effectiveness of NDTs, SDTs and SHM systems	Digital Radiographs (DR)	UniPM
		Strand-Cutting Test (SCT) Core Drilling (CD)	UniRoma1
		Reflectometric Impulse Measurement Technology (RIMT)	UniRoma3 and UniCh
		Ultrasonic Test (UT) Pull-Out (PO)	UniRoma1
		Tomography 2D (Tomo2D) Tomography 3D (Tomo3D) Potential Mapping (PM)	UniRoma3 and UniCh
Dissection of C3sx span in order to map the actual condition state of the prestressing system			UniTN
Phase 2B	Bending and Shear load tests	Strand-Cutting test (SCT)	UniRoma1
		Digital Image Correlation (DIC) Acoustic Emission (AE)	PoliTO
Dissection of C3sx span in order to map the actual condition state of the prestressing system			UniTN
Phase 2C	Dynamic test with controlled damage imposed	Strand-Cutting Test (SCT)	UniRoma1
		Reflectometric Impulse Measurement Technology (RIMT) Tomography 2D (Tomo2D) Tomography 3D (Tomo3D) Potential Mapping (PM)	UniRoma3 and UniCh
Dissection of C3sx span in order to map the actual condition state of the prestressing system			UniTN

Table 3.2 Protocol of the diagnostic campaign

Upon completion of these two phases, controlled demolition of the girders will be conducted to extract and map the actual condition state of the prestressing system. This activity is crucial to verify the effectiveness of the NDT and SDT methods performed, and the Structural Health Monitoring (SHM) systems used during the load and dynamic tests.

4 PRESTRESSED CONCRETE BRIDGE TESTED TO FAILURE: THE ALVEO VECCHIO VIADUCT CASE STUDY

Abstract. The number of bridges approaching or exceeding their initial design life has been increasing dramatically. Meanwhile, bridges are withstanding an ever-increasing traffic volume, both in number and weight of vehicles. Analytical and numerical models can predict bridges' response to traffic loads and their ultimate capacity with low uncertainties; however, such uncertainties increase as bridges age due to deterioration mechanisms. Non-destructive tests of material specimens and full-scale load tests allow for updating structural models and predicting bridges' responses with higher accuracy. On-site load tests with different load levels provide different information on the bridge behaviour (e.g., elastic response, first-crack load, ultimate capacity), which impact the model updating differently. This paper compares the observed response of the Alveo Vecchio viaduct, a prestressed concrete (PC) bridge subjected to a controlled load test up to its failure, with its predicted response provided by four structural models. The observed response is measured by an extensive structural health monitoring system, while the structural models are developed with different levels of refinement and uncertainty in the input parameters. This study gives an insight into the ultimate load-carrying capacity of existing PC bridges and their behaviour during a whole load test to failure. The results show that the load carry capacity of the Alveo Vecchio viaduct is almost four times higher than the design load; likely, many other Italian highway bridges with similar structural characteristics have a similar capacity.

4.1 Introduction

The number of bridges approaching or exceeding their initial design life has increased dramatically over the last decade. The 2021 Report Card for America's Infrastructure [7] points out that 42% of all bridges across the United States are at least 50 years old; the average age of America's bridges is 44 years, and 7.5% of them are considered structurally deficient. In Japan, around 25% of bridges (2-m long or longer) are at least 50 years old, and the number is expected to rise to 52% in 2029 [8]. In Italy, we estimated that 50.4% of the highway bridges are at least 50 years old, and their average age is 48. Figure 4.1 shows the age of a sample of 1945 highway bridges, more than 65% of the Italian asset.

At the same time, bridges are withstanding an ever-increasing traffic volume, both in the number and the weight of vehicles. For instance, in the United States, the vehicle miles travelled reached more than 3.2 trillion in 2019, an increase of 18% from 2000 . The US

Standard [5], the European Standard [114], and the Italian Standard [115] have progressively increased the design traffic load over the years [116]; the current dimensional and mass limits imposed by national's Highway Codes [117] [118] [112] confirm such increment. All that increases the maximum load effects (e.g., shear force and bending moment) that ageing bridges may expect during their remaining life.

As civil infrastructures age, the investments required to maintain their performance and safety increase, along with the impact of bridges' failures on the economy, environment, and society [17], [18], [19]. Moreover, since a short-term substitution of all the structurally deficient bridges is economically and strategically impossible, the average age of bridges and the investments in maintenance will increase exponentially in the future. For instance, the 2020 USA's backlog of bridge repair needs is $125 billion, rising from $14.4 billion annually to $22.7 billion annually [113]. The American Society of Civil Engineers claims that at the current rate of investment, all the currently necessary repairs will take until 2071 and that the additional deterioration over the next 50 years will become overwhelming. In addition, since most goods and products are moved by trucks and trains, even short-term closure of strategic bridges can cause time-loss to drivers due to congestion and excessive damage to national economies [113].

As a result, it is crucial to frequently check bridges' deterioration, prioritise the maintenance within an infrastructure asset, and effectively assess bridges' performance and safety [119]. Non-destructive tests (NDTs) of material specimens and structural health monitoring (SHM) can measure and control the decay of the materials' properties and the variation in the structural behaviour of bridges in-service [62]. Numerical models of bridges can predict their response under operational and exceptional loads with low uncertainties [14]; however, such uncertainties increase as bridges age due to deterioration mechanisms. Moreover, real-life boundary conditions, connections between structural parts, and the soil-structure interaction may differ from what is defined in the numerical model and have an unexpected influence on the observed response. To cope with those problems, NDTs of material specimens and full-scale on-site load tests allow updating model parameters and obtaining predictions of bridges' responses as close as possible to the observed response.

Here, some questions arise. What behaviour can a structural model accurately predict? Are the model predictions in line with load test results? What is it possible to learn from a load test? How accurate are predictions after the model updating?

We presume most careful readers are well aware that progressively refined levels of structural models and structural analysis exist in the scientific literature [15]: linear elastic, linear elastic with a limited redistribution, and plastic analysis with finite elements (FE), beam, frame or handbook methods; non-linear analysis reflecting flexural failures with FE; non-linear analysis reflecting flexural and shear related failures with FE; and fully non-linear analysis reflecting flexural, shear-related and anchorage failures with FE. Typically, predictions of the same structural response obtained from different structural models reveal significant variations. Predictions from refined models can be more accurate, but the analysis is more complex and may take a longer modelling and computational time. Moreover, assumptions on the geometry, boundary conditions, constitutive laws, and solution methods are necessary; thus, the outcomes are highly dependent on the modelling choices, which in turn depend on the analyst's experience [15].

Load tests allow calibrating prediction models and evaluating the performance of existing bridges [13], [14], [15]. Two load tests exist: diagnostic load tests and proof load tests. Diagnostic load tests involve loads lower than the design live load; they allow engineers to compare the observed response of the structure with the predictions of a structural model and update the model based on the results to make it verified in the field [14]. In contrast, proof load tests aim to verify whether a bridge can carry the prescribed factored live loads without distress [14]. Diagnostic load tests are suitable for in-service bridges, which should not experience damage during the test; therefore, only their linear elastic response is observable. However, the response of a structure to service loads is not necessarily representative of its response to higher loads due to non-linearities, stress redistribution, and other forms of interaction among elements. Collapse tests allow learning more about bridges' non-linear behaviour and ultimate capacity; however, the structure will be dismissed after the test.

By analysing several studies published in the scientific literature [92], [93], [94], [95], we observed that, in general, (i) the comparison between models predictions and load tests results typically shows a good correlation for the linear elastic responses; (ii) the correlation decreases significantly after the first crack opens; and (iii) the ultimate capacity observed is lower than the model prediction due to shear failure, or higher due to a conservative estimate by the models. In particular, Bagge et al. [92] present a review of 30 concrete bridges of different types tested to failure between 1952 and 2014: almost a third of them resulted in unexpected types of failure, mainly shear instead of flexure; the differences between predicted and observed capacities often appeared to be a consequence of inaccurate

representations of geometry, boundary conditions, and materials. Cai et al. [93] point out that those differences might also be attributed to field factors (e.g., diaphragm action, parapet stiffening, concrete hardening, unintended composite action, and unintended bearing restraints), which usually increase the bridges' capacity but are neglected during the design stages and in structural models. Also, harsh environmental conditions and the ageing of materials lead to a structural deterioration that affects the load-carrying capacities. For instance, corrosion degradation can produce concrete cracks that follow the trajectory of the post-tensioning tendons, reduce ductility, and halve the load capacity [96].

The correlation between predictions and observation also depends on the structural analysis performed. Pressley et al. [94] compare actual bending failure loads and ultimate loads predicted through progressively refined structural analysis. The standard 1D linear elastic analysis predicted the ultimate loads as 37-42% of the actual load, the 2D yield line predicted 81-96%, and the 3D non-linear FE analyses predicted 89-101%. They also claim that the analyses did not predict the general shear failure mode that accompanied the ultimate bending failure. Bagge et al. [15] confirm that a refined non-linear FE model can reproduce the actual structural behaviour, identifying the failure mechanism and predicting the actual load-carrying capacity with a difference of less than 3.8%.

Finally, many studies show that relatively small changes in the model parameters result in significant changes in the model predictions of the elastic response, load-carrying capacity, and failure mechanism [15], [93]. Sensitivity analyses point out that the most influential model parameters are the concrete compressive and tensile strength, concrete elastic modulus, level of residual stress in prestressing cables, and the boundary conditions at supports.

This paper gives an insight into the ultimate load-carrying capacities of existing prestressed concrete (PC) bridges and studies their response during a load test to failure. It compares the observed response of a PC bridge subjected to a controlled load test up to its failure, the Alveo Vecchio viaduct, with the responses predicted by four different structural models. An extensive SHM system measures the observed response. The structural models have different levels of refinement (two are analytical models, and two are finite element models) and (different uncertainties in the input parameters (two have prior parameters, and two have parameters updated based on monitoring data). First, the paper discusses what engineers can observe and learn from a load test as the load progressively increases (e.g., stiffness, first-crack load, ultimate capacity). Then, it identifies the model parameters that influence the

response prediction the most. Finally, it verifies whether a diagnostic load test carried on up until the design traffic load allows identifying the following states: (i) the structural response remains elastic during the entire load test; (ii) the bridge cracks during the load test; (iii) the bridge was already cracked before the load test.

We organised the manuscript as follows: Section 2 introduces the Alveo Vecchio viaduct; Section 3 illustrates the load test design, providing the details and the hypotheses of the four prediction models developed. Section 4 reports the load test execution: the agenda and the monitoring system results. Lastly, Section 5 discusses the correlation between the models' predictions and the observed structure response. Conclusions are drawn in Section 6.

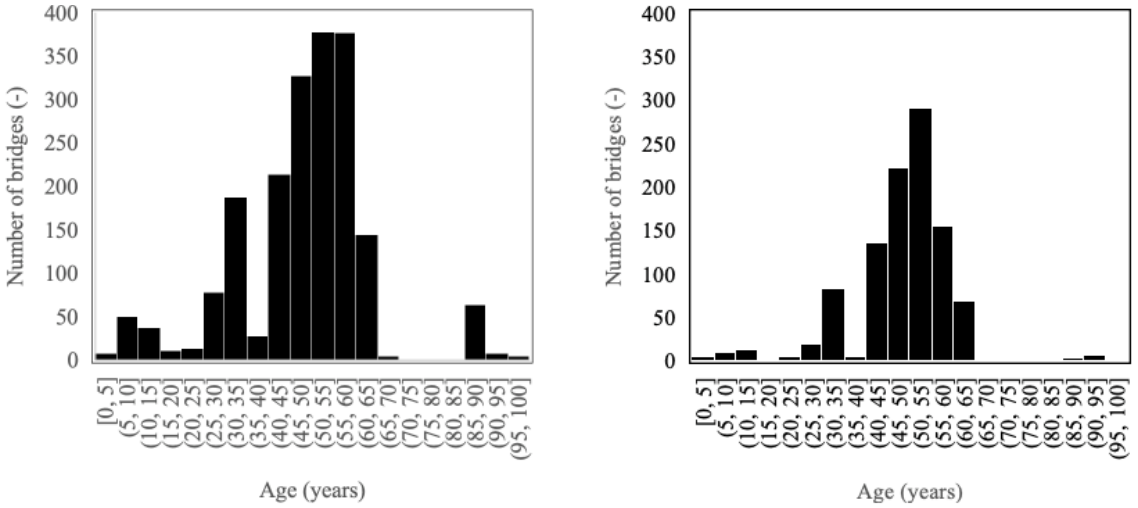

Figure 4.1 (a) Age distribution among a sample of 1945 Italian highway bridges (more than 65% across the Nation); (b) Age distribution among 1019 Italian PC highway bridges with simply-supported spans (52% of the whole sample)

4.2 Case study – the Alveo Vecchio viaduct

In Chapter 3, we comprehensively examine the case study, the Alveo Vecchio viaduct. To enhance clarity, we present the viaduct's top view, lateral view, and cross-section in Figure 4.2. Additionally, Figure 4.3 showcases a transversal section of the girders with the prestressing cables, offering detailed insights into the structural configuration of the viaduct.

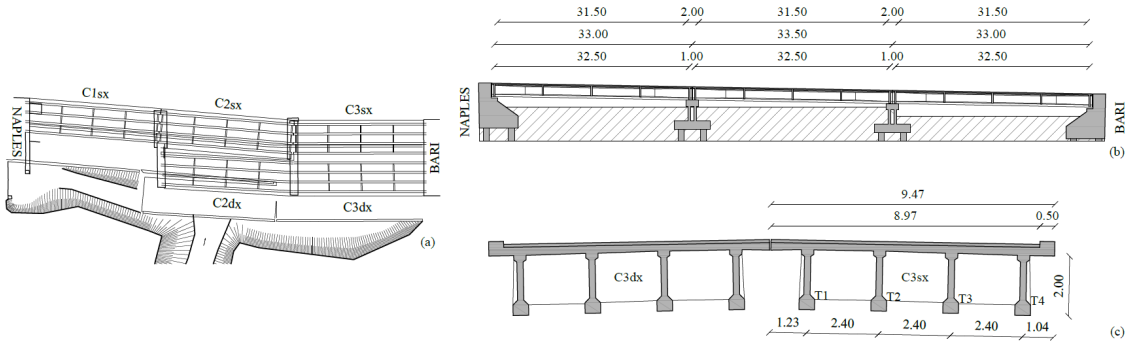

Figure 4.2 (a) top view; (b) lateral view; and (c) cross-section of the Alveo Vecchio viaduct (Italy)

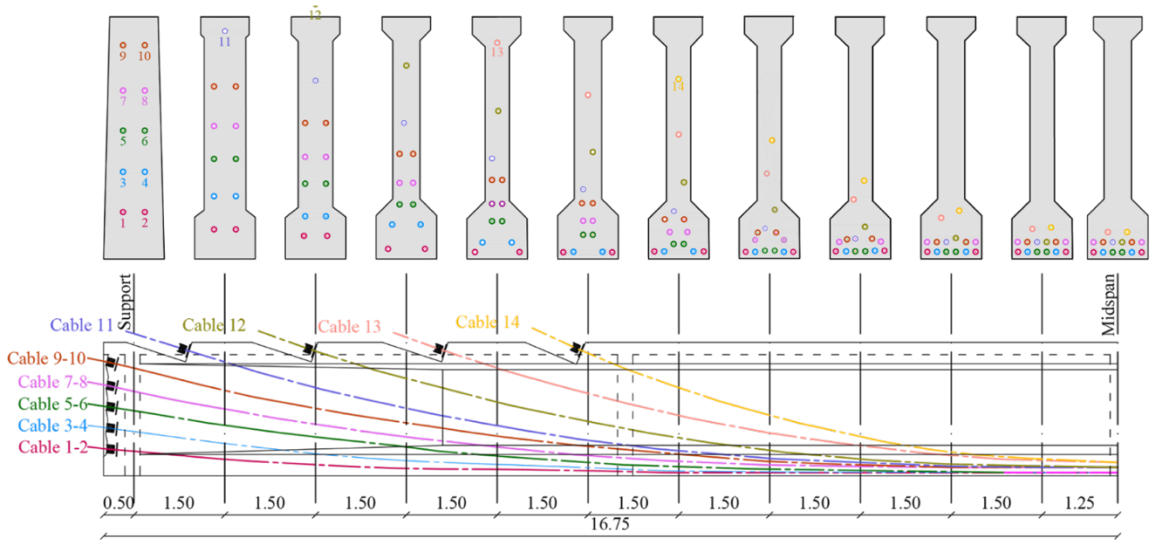

Figure 4.3 Longitudinal and transversal section of girders with post-tensioned cables

4.3 Load test design

4.3.1 Load test protocol

The Alveo Vecchio viaduct was designed in 1966 by Eng. A. Passaro. He chose the design live-loads according to the Italian standards Circ. Min. LL.PP. 14/02/1962 n. 384 [120], and he calculated their effects on each girder through the Courbon method [121]. The design documentation [122] reports that the bending moment on the most stressed girders (externals) of span C3sx due to the design live loads is 4259 kNm. We designed the load test protocol by choosing as the load unit the concentrated load that would have generated a bending moment equal to the design bending moment in the midspan cross-section of the most stressed girders (externals). As a result, the load unit was a 2400 kN concentrated load centred in the midspan applied over a footprint that extends for 7.35 m longitudinally.

Since 1962, vehicles' type, number, and mass have changed significantly. Therefore, we also calculated the highest bending moment on the most stressed girders of span C3sx considering the vehicles that nowadays can transit on the Italian highway network. The Italian Highway Code [112] defines the dimensional and mass limits; the current Italian standard DM 17/01/2018 [115] defines the width of the lines. We considered a train of loads consisting of two 5-axle trucks with a total capacity of 440 kN and a 440 kN work vehicle with the characteristics shown in Figure 4.4. We assumed that the vehicles are in a static configuration aligned at a distance of 1 m. The dynamic effect can be neglected for bridges with short spans like the Alveo Vecchio viaduct. We also assumed two load lanes of 3 m-width plus one of 2.75 m-width for the emergency lane. According to the Courbon method, the emergency lane

implies a negative transverse partition coefficient; consequently, we consider the emergency lane unloaded. The bending moment resulting in the most stressed girders due to the real live-loads is 4853 kNm, which is 13.9% higher than the design bending moment.

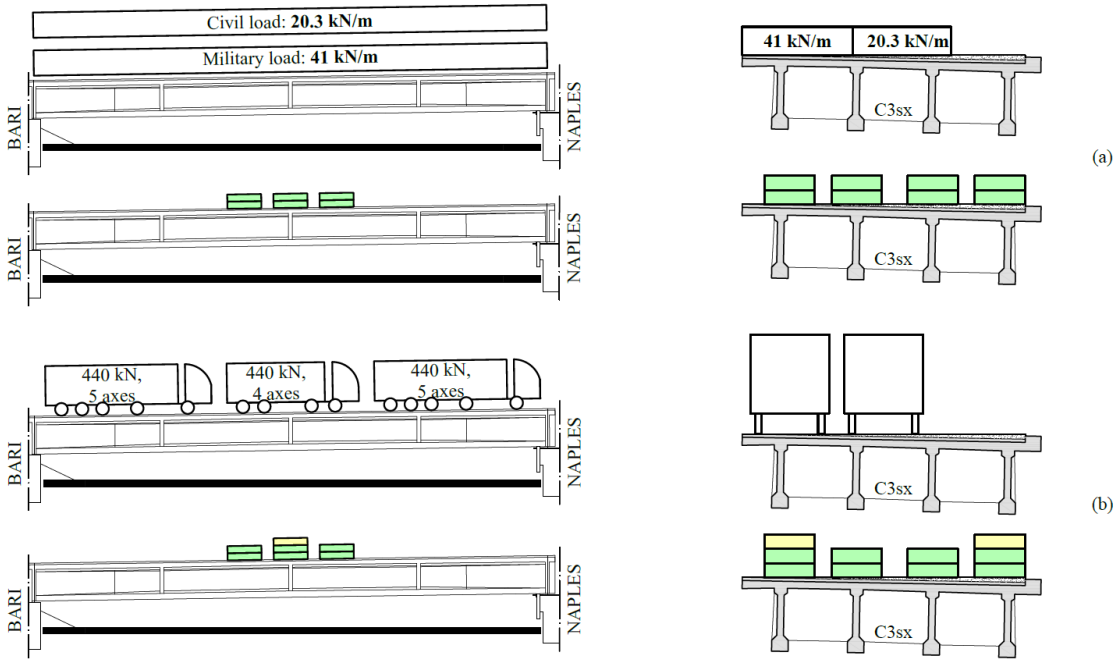

Figure 4.4 a) Live-loads configuration used to design the Alveo Vecchio viaduct; (b) Most demanding live load configuration that can transit nowadays on Italian highways in compliance with dimensional and mass limits.

We chose to apply the load equally distributed between the four girders to avoid introducing a hypothesis on the transverse flexural distribution. We designed the load unit as a matrix of 3 × 4 steel ballast weights with a size of 2.15 × 1.60 × 0.45 m and a weight of 100 kN, each arranged in two layers. We planned to place the weights one by one on the bridge slab with a crane; Figure 4.5 shows the load unit configuration and the sequence of applications to be repeated for each layer.

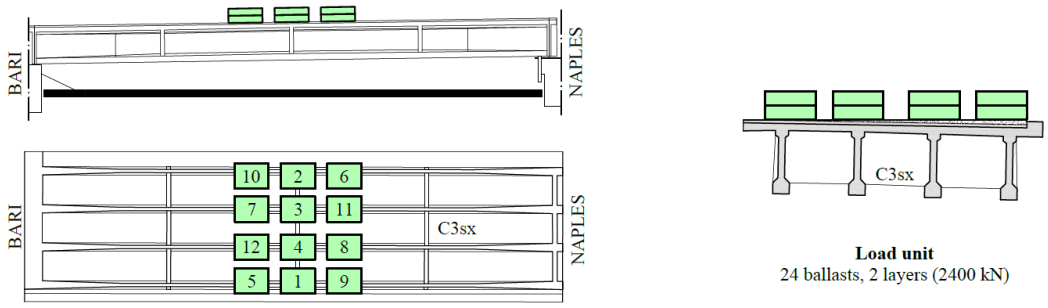

Figure 4.5 Load unit configuration and sequence of weights application repeated for each layer

To collapse the viaduct, we planned to progressively increase the number of weights layers in multiples of the load units. As a result, we defined the following loading phases: P1 – 1200

kN, P2 – 2400 kN, P3 – 4800 kN, P4 – 7200 kN, P5 – 9600 kN, each of them followed by the complete unloading of the bridge. Figure 4.6 shows the load test protocol for the load test of the span C3sx. We defined the stop criteria based on the midspan deflection. The load test had to stop if (i) the midspan deflection would have increased more than 50 mm after a new 100 kN weight application or (ii) the total midspan deflection would have exceeded 300 mm. To avoid the post-critical response of the structure, for safety reasons, and to save the equipment, we decided to perform the last loading phase, P5, in displacement control with four hydraulic jacks placed under the girders midspan.

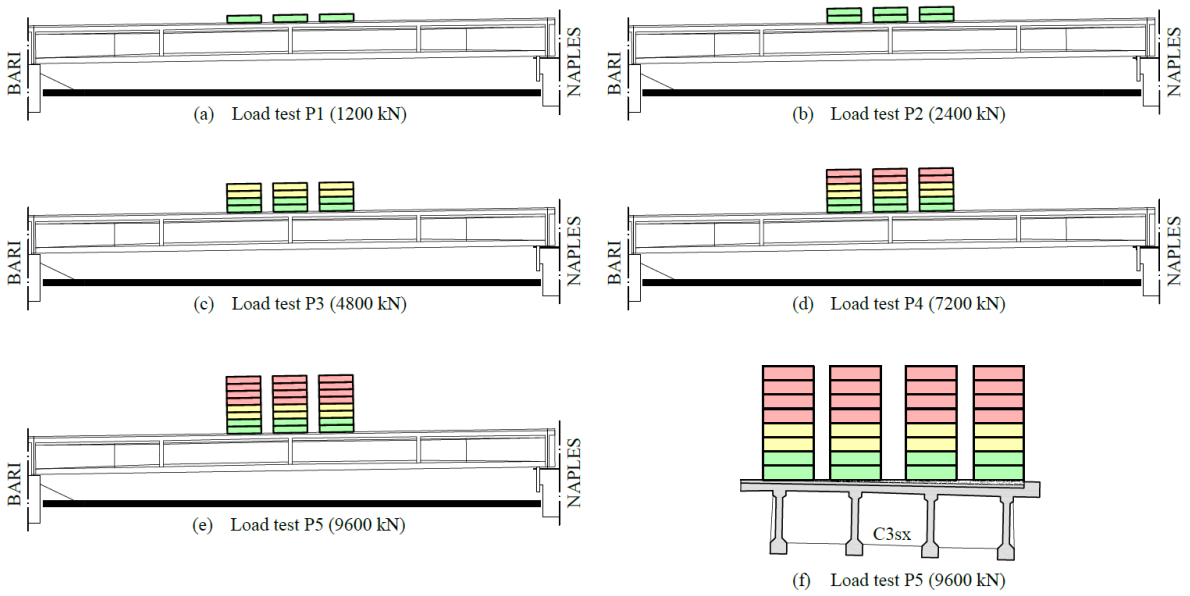

Figure 4.6 Loading phases P1 – P5 with a progressive number of steel ballasts. Colours: green is equivalent to the load unit; yellow is twice the load unit; red is 3 and 4 times the load unit

To verify whether the span C3sx had been unaffected by the 2005 landslide, we performed two additional load tests before P1: one for the abutment and one for the pier. They confirmed the absence of abnormal settlement and rotation of foundations, which might have falsified the output of the load test. We tested the C3sx span's pier and abutment with 4800 kN each, as shown in Figure 4.7.

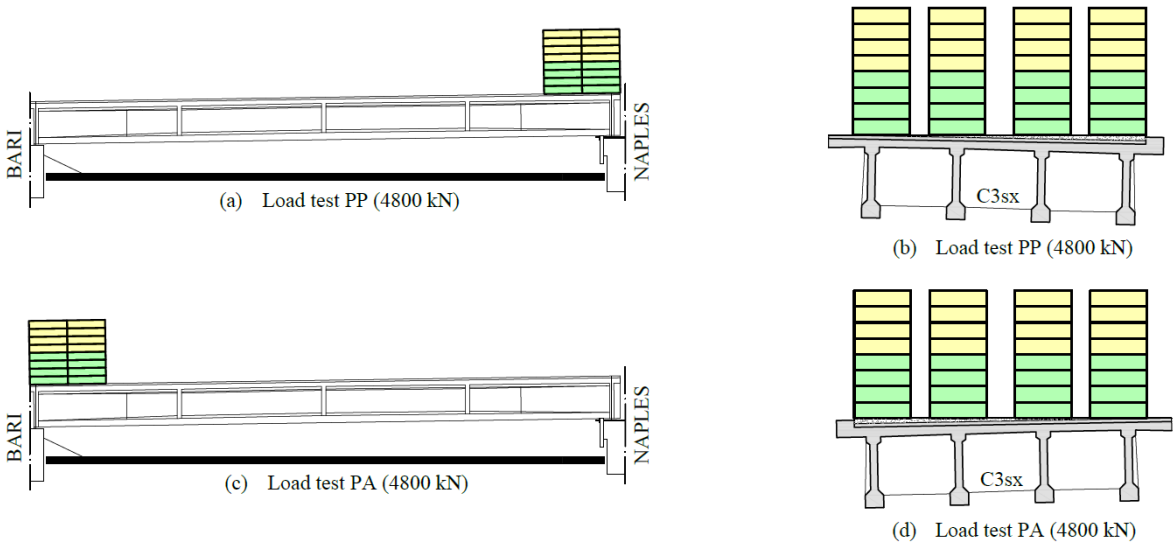

Figure 4.7 Loading phases PP (weights on the pier) and PA (weights on the abutment) with 4800 kN each

4.3.2 Material properties

The design documentation did not report all the mechanical properties of the materials used to build the viaduct. For structural calculations, Eng. Passaro used concrete with a compressive strength of 40 MPa, prestressing steel with a failure strength of 1700 MPa, and reinforcement bars with an ultimate strength of 220 MPa.

We performed an extensive campaign of NDTs to characterise the properties of materials and provide the most accurate input parameters for the prediction models: dead loads g1 and g2 supported by the girders and the following properties:

- Concrete of girders and slab: compressive strength, tensile strength, and elastic modulus.
- Prestressing steel: yield strength, ultimate tensile strength, strain at maximum load, and residual stress.
- Reinforcement steel: yield strength, ultimate tensile strength.

For this purpose, we performed the following tests (divided based on the material investigated):

- Concrete from girders and slab: 18 compression tests on cylindric samples, 18 pull-out tests, 5 indirect tensile tests (Brazilian test), 27 density measurements, and 9 carbonation tests.
- Reinforcement steel: 12 tensile stress tests.

- Prestressing steel: 8 strand-cutting tests of single wires for residual prestress, 12x6 tensile stress tests according to EN ISO 15630-1:2010 [123] yield stress, ultimate tensile stress, and strain at maximum load (12 wires per 6 cables).
- Road pavement: 4 density and thickness measurements.

Figure 4.8 shows the location of the extracted samples along the viaduct. We extracted most of the samples from the C3sx span's elements to accurately estimate its material properties before the load test; in contrast, we sampled the shear reinforcement steel and performed strand-cutting tests on the C1sx span to avoid reducing the C3sx span's performance. Table 4.1 shows the properties of the materials obtained from direct and indirect tests with their mean value, standard deviation, and coefficient of variation. Table 4.2 reports the effects of dead loads on the girders based on different portions of the slab supported by them.

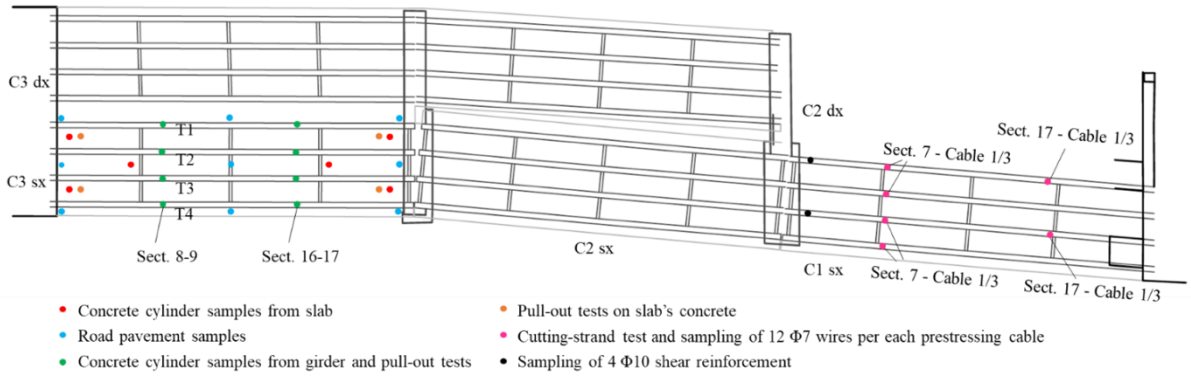

Figure 4.8 Location of the extracted samples and NDTs along the viaduct

Location	Material	Property	Test	Unit	Mean value	Standard deviation	Coeff. of variation
Slab	Concrete	Compressive cube strength	Pull-out	N/mm^2	38.37	3.33	8.68 %
Girder	Concrete	Compressive cube strength	Pull-out	N/mm^2	50.00	5.86	11.72 %
Girder	Concrete	Tensile strength	Brazilian	N/mm^2	2.2	0.34	15.5 %
Girder	Prestressing steel	Yield strength	Tensile	N/mm^2	1509.38	75.38	4.99 %
Girder	Prestressing steel	Ultimate tensile strength	Tensile	N/mm^2	1742.71	37.05	2.13 %
Girder	Prestressing steel	Strain at maximum load	Tensile	%	9.17	2.08	22.64 %
Girder	Prestressing steel	Residual stress	Strand-cut	N/mm^2	618.75	83.43	13.48 %
Girder	Reinforcement steel	Yield strength	Tensile	N/mm^2	398.97	79.03	19.81 %
Girder	Reinforcement steel	Ultimate tensile strength	Tensile	N/mm^2	614.23	48.63	7.92 %
Girder	Reinforcement steel	Strain at maximum load	Tensile	%	22.98	1.37	5.96 %

Table 4.1 Material properties of slab and girders estimated from NDTs

Girder	T1	T2 & T3	T4
M_{g1+g2} [kNm]	6231	5811	5588
V_{g1+g2} [kN]	739	687	659

Table 4.2 Effects of dead loads g1 and g2 on girders T1, T2, T3, T4

4.3.3 Prediction models

Hypothesis on the properties of materials. We assumed the distributions of NDTs results as Gaussian. Based on those distributions, we defined three hypotheses on the mechanical properties of materials, summarised in Table 4.3, as inputs of the prediction models:

- Hp. A: 5% fractal of the distribution of NDTs results, with some variations.
- Hp. B: 50% fractal (average value) of the distribution of NDTs results, with some variations.
- Hp. C: 95% fractal of the distribution of NDTs results, with some variations.

Location	Material	Property	Unit	Hypothesis A		Hypothesis B		Hypothesis C		Notes
				Fractal	Value	Fractal	Value	Fractal	Value	
Slab	Concrete	Compressive cylinder strength	N/mm^2	5%	27.3	50%	31.9	95%	36.4	

Slab	Concrete	Elastic modulus	N/mm^2	5%	29323	50%	31942	95%	34561	(1)
Girder	Concrete	Compressive cylinder strength	N/mm^2	5%	33.5	50%	41.5	95%	49.5	
Girder	Concrete	Tensile strength	N/mm^2	-	0	5%	2.18	5%	2.45	(2) (3)
Girder	Concrete	Elastic modulus	N/mm^2	5%	30774	5%	33523	95%	36272	(1)
Girder	Prestressing steel	Yield stress	N/mm^2	5%	1385	50%	1509	95%	1633	
Girder	Prestressing steel	Ultimate tensile strength	N/mm^2	1.49‰	1485	1.49‰	1618	1.49‰	1751	(4)
Girder	Prestressing steel	Strain at maximum load	%	Design value	3.5	1.49‰	4.43	1.49‰	6.06	(4) (5)
Girder	Prestressing steel	Residual stress	N/mm^2	5%	482	50%	619	Design value	1000	
Girder	Reinforcement steel	Yield stress	N/mm	5%	269	50%	399	95%	529	
Girder	Reinforcement steel	Ultimate tensile strength	[N/mm^2]	5%	534	50%	614	95%	694	

Table 4.3 Three hypotheses on the mechanical properties of materials based on the results from the non-destructive tests

Notes:

(1) $E_{cm} = 22\ (f_{cm}/10)^{0.3}$ from EN 1992-1-1:2004, Table 3.1 (European Committee for Standardization, 2005):

- Hp. A: $E_{ck;0.05} = E_{cm}(1 - 1.645\ CV)$ and $CV = 5\%$.
- Hp. C: $E_{ck;0.95} = E_{cm}(1 + 1.645\ CV)$ and $CV = 5\%$.

(2) Hp. A: the first crack has already opened; therefore, we assume a zero tensile strength of the concrete, $f_{ct} = 0$ MPa.

(3) $f_{ctk;0.05} = 0.7\ f_{ctm}$, where $f_{ctm} = 0.3\ f_{ck}^{2/3}$ from EN 1992-1-1:2004, Table 3.1 (European Committee for Standardization, 2005), and:

- Hp. B: $f_{ck} = f_{cm} - 8$; f_{cm} from pull-out tests.
- Hp. C: $f_{ck} = f_{cm} - 1.645\sigma$; f_{cm} and σ from pull-out tests.

(4) 1.49‰ of the distribution f_t/f_{ym}, with f_{ym} the yield stress of the same hypothesis; $1.49 \cdot 10^{-3}$ is (number of prestressing wires tested)$^{-1}$ because we consider that the structural collapse occurs when the first prestressing wire fails.

(5) Hp. C: average value of the more likely values; we considered a few values as outliers.

Structural models. Firstly, we developed an analytical model called ANA1 for designing the load test. We predicted the structural capacity in terms of bending moment and shear force. We compared them with the structural demand resulting from the increasing number of steel ballasts on the bridge. Model ANA1 is based on the design documentation and NDTs on material specimens only, without any evidence of the actual response during the load test.

Then, we updated the analytical model ANA1 into the analytical model ANA2 during the load test, once the first cracks had opened, by changing the residual stress to make the first crack loads (one for each girder) predicted by the numerical model equal to the observed ones. Therefore, model ANA2 is based on the design documentation, NDTs, and a diagnostic load test on the bridge until the first crack opening. Results from model ANA2 defined the load-test stop-criteria.

After the conclusion of the load test, we developed a finite element model, FEM1, with the same hypotheses as model ANA2, aiming to interpret the test results better.

Finally, we updated model FEM1 into model FEM2, changing the most influential parameters according to a sensitivity analysis (e.g., the elastic modulus of the concrete and the residual stress of prestressing cables) aiming to make the model predictions as similar as possible to what was observed by the monitoring system.

In this section, we illustrate only the hypotheses of the four prediction models; we will show their results and the model updating procedure in Section 5.

Model ANA1

Models ANA1 and ANA2 consider the following parameters as deterministic:

- Ultimate strain of concrete $\varepsilon_{cu} = 0.35$ %.
- Elastic modulus of the prestress steel: $E_s = 200$ GPa;
- Effects of dead loads g_1 and g_2 resulting from the NDTs (see Subsection 4.3.2).

Moreover, we implemented the following stress-strain relation curves of materials:

- Parabola-rectangle diagram for concrete under compression from EN 1992-1-1:2004 [124];
- Bilinear diagram for harmonic and reinforcing steel: linear elastic up to the yield strain, with a further increase between the yield and the ultimate strain.

We calculated the shear resistance of the girders over the pier and abutment with equations for the design shear resistance of the member without shear reinforcement from EN 1992-1-1:2004 [124], and the ultimate moment resistance of the prestressed concrete midspan cross-section of each girder with equations from EN 1992-1-1:2004 [124]. Regarding the ultimate moment resistance, we assumed different inertial properties of the girders: T2 and T3 have the same geometry, T1 supports a wider slab (0.270 m vs 0.240 m), and T4 supports a shorter slab with an additional curb, which significantly increases the stiffness. Table 4.4 shows the moment and shear resistance of each girder predicted by model ANA1.

Hypothesis	T1		T2		T3		T4	
	M_R [kNm]	V_R [Nm]	M_R [kNm]	V_R [Nm]	M_R [kNm]	V_R [Nm]	M_R [kNm]	V_R [Nm]
A	19748	1359	19521	1359	19521	1359	19990	1359
B	21777	2984	21535	2984	21535	2984	21605	2984
C	23347	5240	23155	5240	23155	5240	23260	5250

Table 4.4 Ultimate moment and shear resistance for each girder predicted by the structural model ANA1

Model ANA2

We updated model ANA1 into model ANA2 by changing the residual stress $\sigma_{p,\infty}$ in the material hypotheses, and we removed hypothesis A since it seemed excessively precautionary. Table 4.5 shows the updated value of residual stress.

Residual Stress $\sigma_{p,\infty}$ [MPa]				
Hypothesis	T1	T2	T3	T4
B	1030	975	980	1005
C	955	980	1020	950

Table 4.5 The updated value of residual stress $\sigma_{p,\infty}$ for each girder and hypotheses B and C implemented in ANA2

Model FEM1

We designed the finite element model FEM1 with the open-source software OpenSees developed by PEER (Pacific Earthquake Engineering Research) [125]. We considered only the material hypothesis C as defined for model ANA2, and we modelled each girder with frame elements with fibre section to permit the spread of plasticity and better simulate the girders' geometry and the position of the prestressing cables along the girder. Each fibre had the following non-linear stress-strain relations already implemented in OpenSees [126]:

- "Concrete 04 - Popovics Concrete Material" for the concrete.

- “Steel04 Material” for the harmonic steel.
- "Steel02 Material – Giuffr.- Menegotto-Pinto Model with Isotropic Strain Hardening” for the steel reinforcement.

We discretised each girder in 24 frame elements. We modelled the cross-girders as rectangular connecting elements, adding a portion of the collaborating slab to simulate its orthogonal stiffening effect. Figure 4.9 shows the number and length of each element and a girder modelled with a frame element with a fibre section. We modelled the span as simply supported by adding one pinned support over the abutment and one roller support over the pier for each girder.

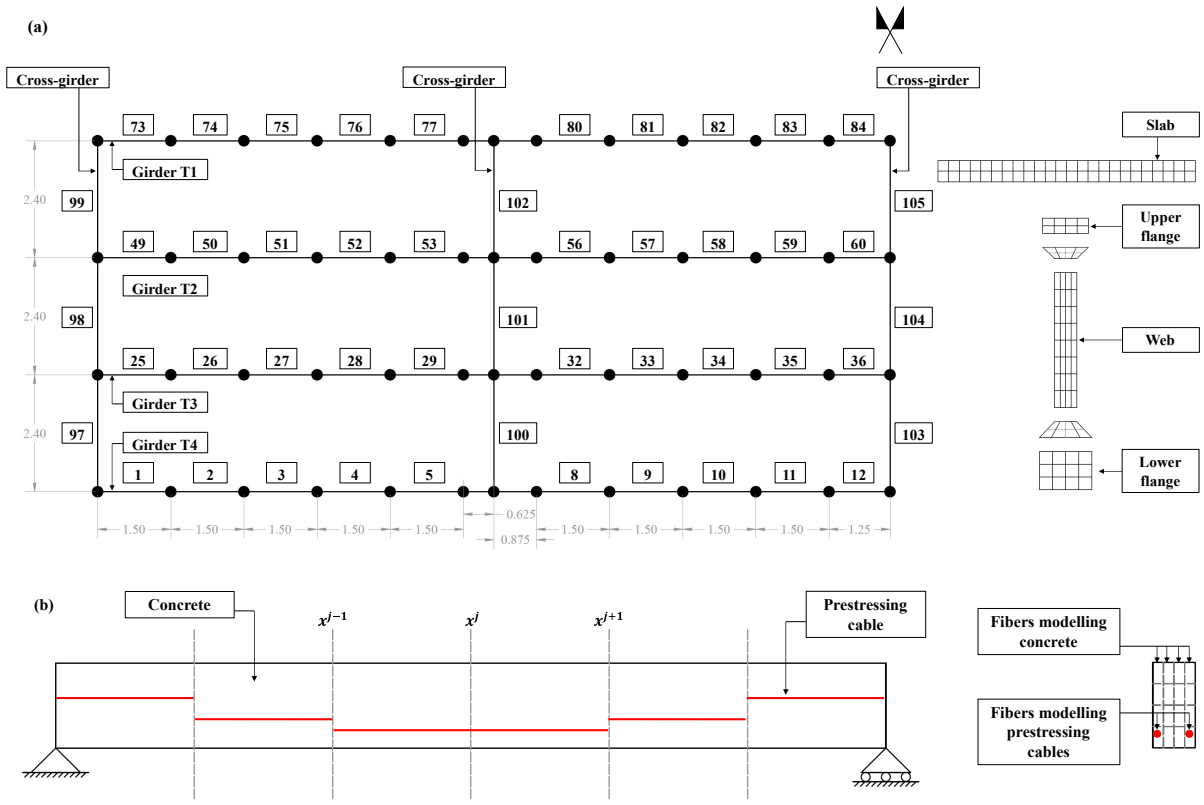

Figure 4.9 a) Discretisation of (a) the bridge span and girders and (b) the prestressing cables in frame finite elements with fibre section

Model FEM2

We updated model FEM1 into model FEM2 by changing the residual stress of prestressing cables $\sigma_{p,\infty}$ and the elastic modulus of the concrete E_c in each girder to better simulate the response of the viaduct observed by the monitoring system during the load test. We identified such values with a sensitivity analysis described in Subsection 4.5.2; Table 4.6 reports them.

Parameter	T1	T2	T3	T4
Residual stress $\sigma_{p,\infty}$ [MPa]	696	794	820	950
Elastic modulus E_c	39899	39899	39899	39899

Table 4.6 The updated value of the residual stress σp,∞ and the elastic modulus Ec of the concrete for each girder implemented in FEM2

4.4 Load test execution

4.4.1 Calendar

From 26 to 30 June 2019, a monitoring system (see Subsection 4.5.4) measured the bridge's response to environmental live-loads, measurements necessary for the temperature compensation of data acquired during the load test (see Subsection 4.4.3). The load test started on 1 July 2019 with the loading of the pier (phase PP), which was unloaded the day after by moving the steel ballasts progressively from the pier to the abutment (phase PA). The flexural load test of the span started on 4 July 2019 and continued until 23 July 2019, when it ended at 9300 kN once the stop criterion occurred. Table 4.7 reports the calendar: some loading and unloading phases lasted more than one day; weights were placed with an almost constant frequency of 1 ballast every 5 minutes. Figure 4.10 shows pictures of the bridge loaded at the end of all the loading phases.

Phase	Description	Data	Start loading	End loading	Start unloading	End unloading
P0	Environmental live loads	26/06-01/07/2019	-	-	-	-
PP	Pier 4800 kN	01/07/2019	16:15	21:27	10:04(*)	18:06(*)
PA	Abutment 4800 kN	02/07/2019	10:04	18:06	6:40(*)	12:30(*)
P1	Midspan 1200 kNt	04/07/2019	7:22	8:19	9:55	10:30
P2	Midspan 2400 kN	05/07/2019	10:30	12:27	13:20	16:00
P3	Midspan 4800 kN	08/07/2019	12:00	18:45	7:30(*)	14:49(*)
	Midspan 7200 kN – Part 1	10/07/2019	6:30	13:57 (4800 kN)	-	-
P4	Midspan 7200 kN – Part 2	11/07/2019	6:30 (4800 kN)	13:37 (7200 kN)	15:48 (720t)	18:09 (480t)
	Midspan 7200 kN – Part 3	12/07/2019	-	-	8:47 (480t)	12:40
	Midspan 9600 kN – Part 1	21/07/2019	13:15	18:00 (4800 kN)	-	-
P5	Midspan 9600 kN – Part 2	22/07/2019	6:45 (4800 kN)	15:23 (9300 kN)	16:45 (9300 kN)	21:20 (6000 kN)
	Midspan 9600 kN – Part 3	23/07/2019	-	-	8:58 (6000 kN)	13:10

Table 4.7 Load test calendar with date and time of each loading and unloading phase. (*) of the following day

Figure 4.10 Pictures of the Alveo Vecchio viaduct during the loading phases (a) PP – 4800 kN; (b) PA – 4800 kN; (c) P1 – 1200 kN, (d) P2 – 2400 kN, (e) P3 – 4800 kN, (f) P4 – 7200 kN, and (g) P5 – 9600 kN

4.4.2 Structural health monitoring system

We designed the SHM system based on the Italian Guidelines for structural health monitoring, UNI/TR 11634:2016 [110] [127]. Firstly, we identified the key parameters representing: the bridge response, the damage propagation during the load test, and the stop criteria. Then, we defined the type and position of measurements required to calculate the key parameters and chose the sensors' technology.

Key parameters. We defined two sets of key parameters: (i) key parameters to represent the structural behaviour during the load test; (ii) key parameters to identify in real-time the structural response and damage condition and verify the stop criteria. Table 4.8 summarises

the objectives, the key parameters, and the quantities we chose to measure to monitor the response of the bridge.

Structural behaviour during the load test			Real-time structural response & stop-criteria verification		
Objective	Key parameter	Measurement	Objective	Key parameter	Measurement
Structural distortion	Girder's deflection Pier and abutment settlement and inclination Bearings' crushing	Girder displacement Pier and abutment displacement and rotation	First-crack opening	Strain at the bottom of the midspan girders	Strain at the bottom of girders
Damage identification	Crack's initiation and propagation on girders Structural stiffness variation	Strain at the bottom of girders Acoustic emission Experimental modal analysis	Non-linear behaviour	Midspan deflection	Girder displacement
Thermal effects	Distortions due to temperature gradients	Temperature	Failure	Midspan deflection	Girder displacement

Table 4.8 Objectives, key parameters, and measured quantities defined to design the structural health monitoring system

System technology. Based on key parameters and quantities to be measured, we identified the type and required performance of the sensors. Table 4.9 provides technical details of the monitoring system designed, which consists of 119 sensors divided into 8 types: wire displacement sensors, deformation sensors, crack-opening sensors, electronic level, temperature sensors, inclinometers, accelerometers, and acoustic emission sensors. We also monitored air temperature, air humidity, and wind speed.

Quantity	Location	Unit	Sensor	Model	Manufacturer	Full-scale (FS)/ Range	Accuracy/ Resolution	N°
Girders' deflection	Bearings, *L*/4, *L*/2, 3/4*L*	mm	Wire displ. transducer	PT1DC-2 PT1DC-5	Celesco	50 mm 100 mm	0.28% FS	20 2
Girders' deflection	*L*/4, *L*/2, 3/4*L*	mm	Wire displ. transducer	PT1DC-20	Celesco	500 mm	0.18% FS	12
Displacement	All bridge	mm	Digital level & optical prism	LS10 0.3 mm	Leica	Min: 1.8 m Max: 110 m	Height: 0.3 mm Dist: 15 mm	18
Settlement	Abutment,	mm	Rectilinear	PZ12-50	Gefran	50 mm	-	8

	pier		displ. transducer					
Inclination	Abutment, pier, girders	°	Biaxial el-tiltmeter	-	Earth System	±5°	0.001°	12
Crack opening	Midspan T1, T4	mm	Rectilinear displ, transducer	PZ12-A-25 PZ12-100	Gefran	25 mm 100 mm	±0.01% FS	18 4
Temperature	Distributed	°C	Resistance thermometer	PT100	Earth System	-50/+250 °C	0,2 °C	16
Deformation	Top slab	με	Rectilinear displ. transducer	PZ12-A-25	Gefran	25 mm	-	3
Acceleration	Girders T1, T4	mg	Accelerometer	393B12	PCB	±0.5 g pk 0.15-1000 Hz	0.000008 g rms	15
Acoustic emission	Midspan T2, T3	mg	Accelerometer	42A18	Endevco	±10 g 50-10 kHz	-	4

Table 4.9 Measured quantity, location, performance, number, and other characteristics of sensors. (displ. = displacement)

System layout. Figure 4.11 shows the monitoring system layout: (a) wire displacement sensors for measuring the deflection of girders, rectilinear displacement transducers for the crushing of bearings and the settlement of pier and abutment, and biaxial tiltmeters for the inclination of the pier, abutment, and girders; (b) rectilinear displacement transducers for cracks opening and top slab deformation, and acoustic emission sensors; and (c) platinum resistance thermometers for temperature and accelerometers for dynamic monitoring.

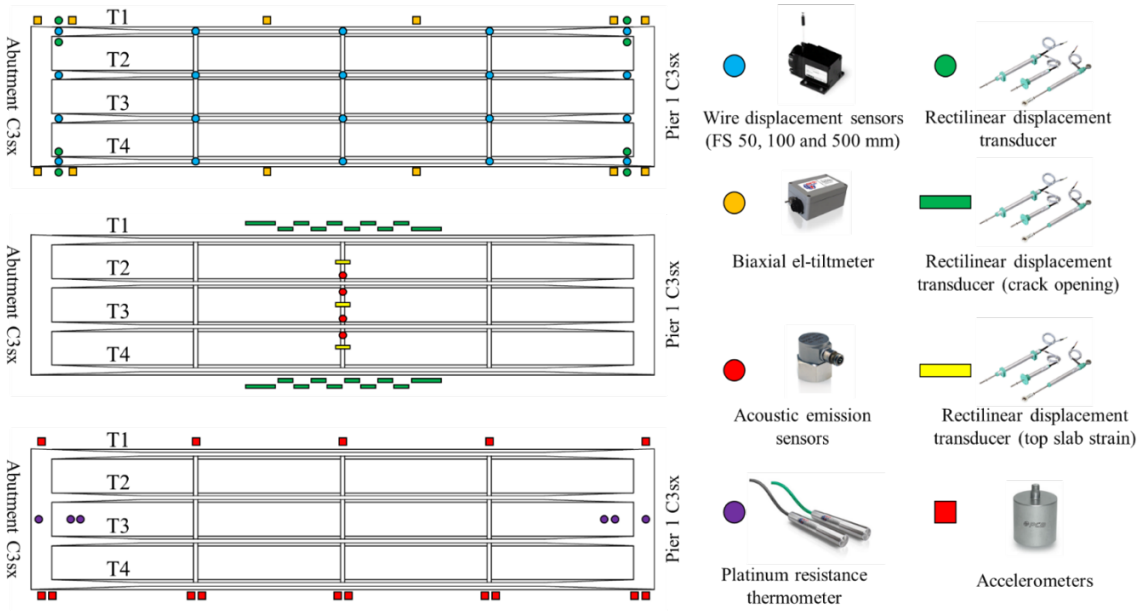

Figure 4.11 Layout of the structural health monitoring system installed on the Alveo Vecchio viaduct during the load test

4.4.3 Observed response

During the load test, the monitoring system acquired a large amount of data. We present and discuss only the most significant ones for the representation of the bridge's response and make a comparison with the prediction of models.

Direct measurements.

Deflection of girders

The deflection of girders is significant because (i) we defined the stop criteria in terms of deflection measurements, and (ii) we aimed to compare the deflection measured during the test with those predicted by the structural models. Figure 4.12 shows the deflection observed at the midspan of the girders against the load placed during the loading phases P1 – P5. It is possible to recognise stage I – elastic, between 0 – 3600 kN; stage II – cracks initiation and propagation, between 3600 – 8700 kN; and stage III – after the yielding of post-tensioned cables of all girders, over 8700 kN. The stop-criterion, a total deflection of a girder higher than 300 mm, was reached during the loading phase P5 by the girder T1 for a load of 9300 kN; thus, we stopped the load test.

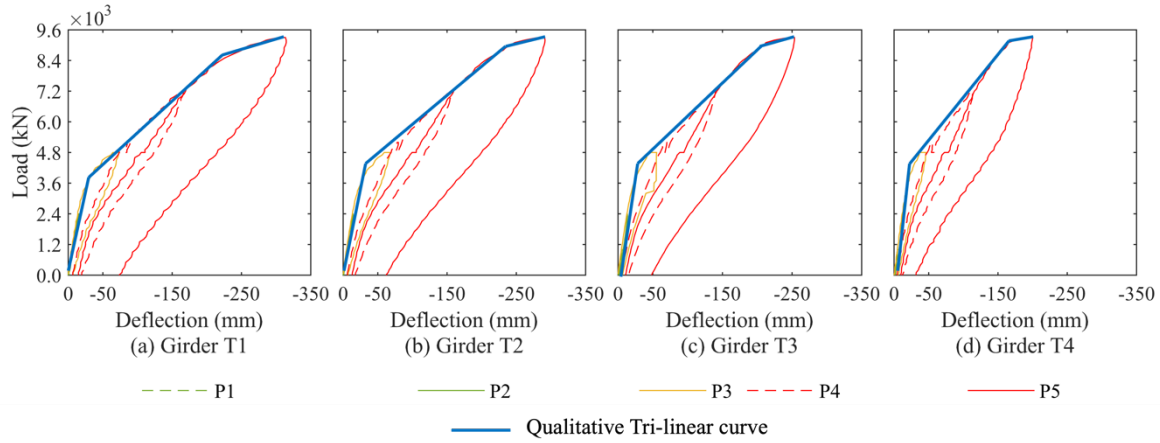

Figure 4.12 Deflection of the girders midspan plotted against the load measured during the loading phases P1 – P5

Figure 4.13 shows the longitudinal deformed shape of each girder at the end of each loading phase. The deflection was measured close to the bearings, at L/4, L/2, and 3L/4, where L is the length of the span. The girder T1 experienced the highest deflection; the other girders' deflection decreased progressively toward T4. As a result, the bridge deck experienced a visible torsion. Possible reasons are the different geometry of the girder T4 due to the curb, the loads' redistribution due to the cross-girders, and a different crack-propagation and stiffness variation among the girders.

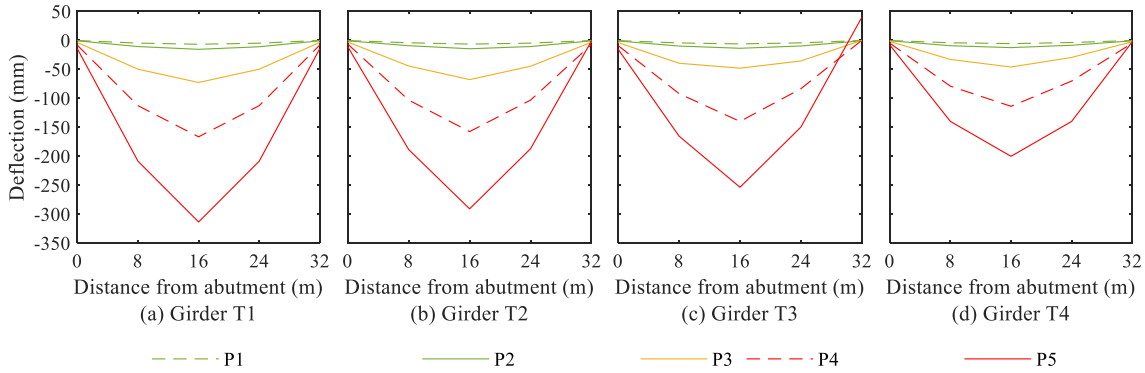

Figure 4.13 Longitudinal deformed shape of girders (a) T1, (b) T2, (c) T3, and (d) T4 at the end of each loading phase

Crushing of bearings.

The bearings were elastomeric pads. They experienced a vertical elastic deformation up to 1.030 mm during loading P1 and P2. At the end of the load test (P5), they accumulated a plastic deformation of 3.067 mm. As a result, the deflection of girders reported in Figure 12 and Figure 13 is not significantly affected by the bearings' vertical deformation. Figure 4.14a and Figure 4.14b show the vertical deformation of T1 bearings over the abutment and the pier.

Settlement of foundations.

During the load test, we did not record relevant settlement of the abutment and pier foundations of span C3sx, which confirmed that the 2005 landslide did not compromise their capacity. We measured settlements of around 0.1 mm during the load phases P1 and P2, 0.4 mm during P3 and P4, and 0.6 mm during P5. As a result, the deflection of girders reported in Figure 4.12 is not affected by the settlement of foundations.

Rotation of pier and abutment.

We did not record relevant rotation of the abutment and pier during the load test. The measured inclination was always lower than 0.1°. This result confirms that the abutment and pier foundations did not lose capacity due to the 2005 landslide. As a result, the deflection of girders reported in Figure 12 is not affected by abutment or pier inclination.

Crack-opening.

Figure 4.14c and Figure 4.14d show the longitudinal strain measured by crack-opening sensors at the bottom of the middle cross-section of girders T1 and T4, respectively. Girder T1 experienced a significant change in the strain at 3300 kN during the load phase P3 (solid amber line – Figure 14a), which marks the opening of the first crack and a change of the

girder's structural response from state I (elastic) to state II (cracked). On the other hand, girder T4 experienced the opening of the first crack at 4000 kN (solid amber line – Fig. 14b), which confirms the difference in the girders' stiffness starting from P3 and explains the highest deflection of T1 than T4. Figure 4.15 shows the crack pattern on girder T4 at the end of the load test. The amber and red triangles represent the propagation of cracks from phase P3 to phase P5: amber triangles mark the end of cracks after phase P3 – 4800 kN, single red triangles mark the end of cracks after phase P4 – 7200 kN, and double red triangles mark the end of cracks after P5 – 9300 kN. Girders T2, T3, and T4 have a similar crack pattern.

Acoustic emission.

We analysed the AE signals recorded during the load test and extracted the following parameters: amplitude, signal strength (MARSE), and peak frequency. A comprehensive report of the results and an in-depth discussion are in Chapter 5. Our analysis focuses on AE results from the girder T2; they show the opening of the first crack at 4300 kN. That is in contrast with the measurements of the crack-opening sensors. Crack opening sensors on girder T1 point out that the first crack opened at 3300 kN (Figure 4.14a). This difference can be explained by the difference in the girders monitored by the two technologies: girder T1 by crack-opening sensors and girder T2 by AE sensors. The girder T1 experienced the highest deflection and deformation; therefore, it is reasonable to assume that cracks have opened first on the girder T1 and then on the others.

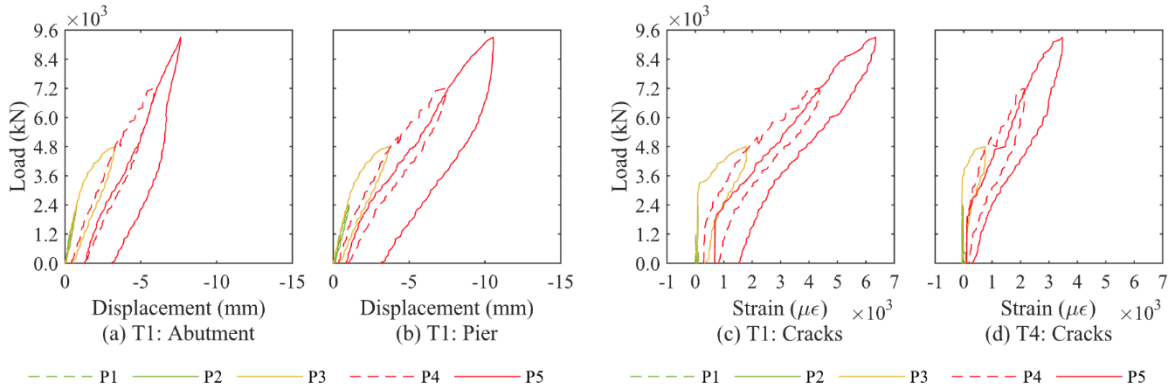

Figure 4.14 Vertical deformation of elastomeric bearings of girder T1 over (a) the abutment and (b) the pier; longitudinal strain measured at the bottom of the midspan of girders (c) T1 and (d) T4 during the load test

Figure 4.15 Visible cracks on the middle portion of girder T4 opened during the loading phases P3 (amber triangles), P4 (red single triangles), and P5 (red double triangles)

Temperature-compensation of measurements. It is commonly recognised that the response of a civil structure is significantly influenced by temperature variations [128], [129]. For this reason, we performed a temperature compensation [119] of the measurements acquired by the monitoring system to remove temperature effects from the structure's response and analyse only the response to the load progressively applied.

Based on the measurements of the bridge response to environmental live-loads recorded during phase P0 (mainly the variation of temperature), we found a correlation between the temperature in concrete and the sensors' measurements. Those are the steps that we followed: (1) we measured the temperature with 12 PT100 sensors in different portions of the bridge; (2) we limited the number of temperatures to 3 principal components using the Principal Component Analysis [130] to reduce the complexity of the problem; (3) we used a linear interpretation model to fit the measurements, and we estimated the model parameters through a least squares regression using the software MATLAB; (4) eventually, we calculated the thermal-compensated values by subtracting the terms related to the temperature measurements Δ. The linear interpretation model used to fit the monitoring data is:

$$\hat{\varepsilon} = \varepsilon_0 + m\,t + \alpha_1\,T_1 + \alpha_2\,T_2 + \alpha_3\,T_3 = \varepsilon_0 + m\,t + \Delta \quad (1)$$

where $\hat{\varepsilon}$ is the total strain, ε_0 is an offset parameter representing the ideal strain at time t_0 and temperature T_0, m is the variation trend over time, t is the instant of time considered, α is the apparent thermal expansion coefficient (i.e., it takes into account the changing of the strain as a function of the temperature), and T_i are the principal components of the temperature.

Table 4.10 and Figure 4.16 show the results of the temperature compensation of the measured response of the girder T1.

Measurement	Location	Unit	P1 – 1200 kN		P2 – 2400 kN		P3 – 4800 kN	
			NC	TC	NC	TC	NC	TC
Deflection	Midspan	mm	-6.287	-6.287	-15.60	-15.91	-72.87	-73.29

Concrete strain	Bottom of the midspan	με	48.40	53.60	178.8	171.2	1445	1436
Crushing of bearings	Abutment	mm	-0.2998	-0.2790	-0.7692	-0.7869	-3.291	-3.329
	Pier	mm	-0.4471	-0.4402	-1.030	-1.024	-3.667	-3.687

Table 4.10 Non compensated (NC) and temperature compensated (TC) deflections, concrete strain, and crushing of bearings measured on the girder T1 during the loading phases P1, P2, and P3

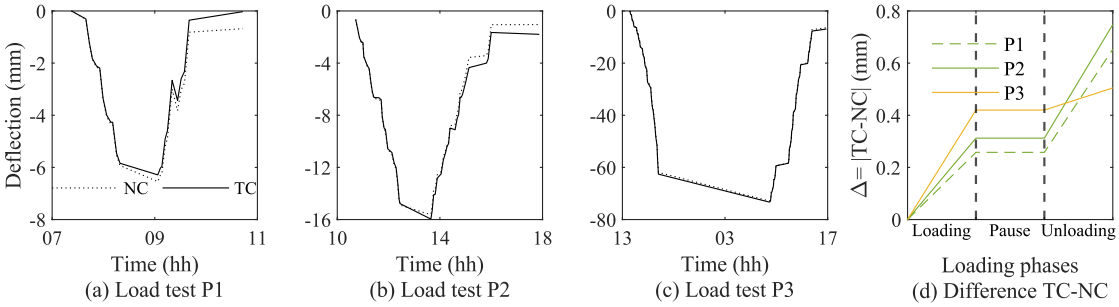

Figure 4.16 Non compensated (NC) and temperature compensated (TC) deflections measured at the midspan of the girder T1 during the loading phase (a) P1, (b) P2, (c) P3. (d) Difference between TC and NC deflections during loading phases P1, P2, P3

The temperature compensation proved necessary to provide more detailed information on the structure, especially for low load levels. Table 4.11 shows the error we would have committed without operating the temperature compensation. The temperature compensation gives symmetry to the response measured during loading and unloading, especially for tests with low loads. The symmetry is a key parameter to ensure that the bridge did not experience permanent damage during the test.

Measurement	Location	Unit	P1 – 1200 kN		P2 – 2400 kN		P3 – 4800 kN	
			e [unit]	*e/m* [%]	*e* [unit]	*e/m* [%]	*e* [unit]	*e/m* [%]
Deflection	Midspan	mm	0.2577	4.100	0.3122	1.962	0.4199	0.5729
Concrete strain	Bottom of the midspan	με	5.541	11.49	7.601	4.247	8.774	0.6071
Crushing of bearings	Abutment	mm	$2.078 \cdot 10^{-2}$	7.448	$1.768 \cdot 10^{-2}$	2.247	$3.785 \cdot 10^{-2}$	1.137
	Pier	mm	$6.920 \cdot 10^{-3}$	1.5719	$5.996 \cdot 10^{-3}$	0.5855	$1.968 \cdot 10^{-2}$	0.5338

Table 4.11 Errors without operating the temperature-compensation: e is the absolute value of the error, e/m is the relative value of the error, obtained by dividing the absolute value e with the non-temperature-compensated measurement m

Vibrational measurements. We performed an experimental modal analysis [131] with the vibrational measurements recorded after each loading and unloading phase P1 – P5. It allowed us to determine the peak frequencies of the span and observe their variation during the test. The vibrational measurements were acquired for 60 seconds at a sampling frequency of 800 Hz by 15 accelerometers attached solidly to the structure, positioned below the slab: 10 vertical axis accelerometers and 5 horizontal axis accelerometers. We provided an artificial excitation to the structure by dropping a 50 kg weight from a height of 0.50 m.

We dropped the weight always in the same position on the girder T4 at a distance of L/4 from the abutment. We repeated the dynamic test before, during, and after each loading and unloading phase. For safety reasons, during phases P4 and P5, we performed the dynamic test at 4800 kN and not at the end of the loading phases. We processed the acquired data with the software Diadem (National Instruments).

Figure 4.17a shows the frequency response functions (FRFs) obtained from the accelerometer placed under the girder T4 where the weight drops before the loading phase P1 and at the end of each unloading phase (always with the bridge unloaded). It is possible to observe to what extent the peak frequencies change as the damage progresses while the boundary conditions (mass and constraints) do not change. We focused mainly on frequencies below 10 Hz to control the evolution of the first modes of the span. The two peak frequencies appear as a double peak with closely spaced frequencies, which progressively move towards the lower frequencies as the applied load increases (from P1 to P5) and the damage progresses. The peak frequencies variations of the first two vertical modes (always measured with the bridge unloaded) are summarised in Table 4.12 and represented in Figure 4.17b. They highlight a downward trend before and after each loading phase. The reduction during P3 confirms the change in the girders' stiffness; thus, the change from state I (elastic) to state II (cracked) occurred during P3.

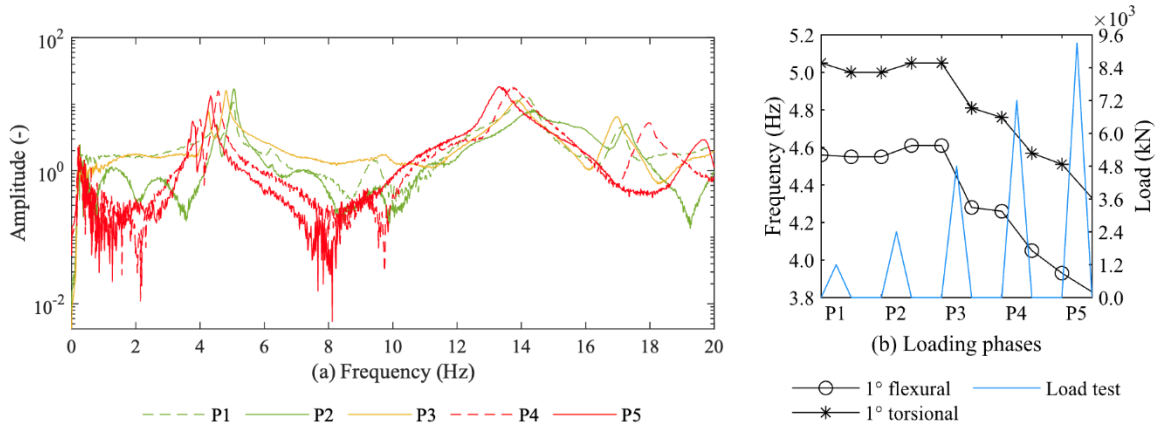

Figure 4.17 (a) FRFs from the accelerometer located on the girder T4 under the weight drops before P1 and at the end of each unloading phase. (b) variation of the first two modal frequencies during the load test

Phase	Load	First vertical mode			Second vertical mode		
		Before (0 kN)	Max. Load	After (0 kN)	Before (0 kN)	Max. Load	After (0 kN)
P1	1200 kN	4.55	3.96	4.63	5.05	4.63	5.00
P2	2400 kN	4.55	3.44	4.61	5.00	4.21	5.05
P3	4800 kN	4.61	2.53	4.28	5.05	3.24	4.81
P4	7200 kN	4.26	2.28(*) 2.13(*)	4.05	4.76	3.07(*) 2.68(*)	4.57
P5	9600 kN	3.93	2.48(*) 2.25(*)	3.83	4.51	3.12(*) 2.83(*)	4.33

(*) for the loading and unloading phases P4 and P5, the acquisition at maximum load was performed at 4800 kN for safety reasons.

Table 4.12 Peak frequencies of the first two vertical modes calculated before and after each loading and unloading phase

4.5 Discussion

4.5.1 Model prediction vs observed response

In this Subsection, we report the girders' predicted and observed vertical deflection, their stiffnesses resulting from the trilinear idealised flexural response, their first-crack load, and ultimate load-carry capacity. Figure 4.18a shows the envelope of the vertical deflections measured at the midspan of each girder by the monitoring system, while Figure 4.18b shows their trilinear idealised flexural response. As explained in Subsection 4.4.3, the girder T1 experienced the greatest deflection, up to 30% more than the others. That is probably due to the highest stiffness of T4, the cross girders' influence on the loads' redistribution, and the different cracks initiation and propagation among girders. Indeed, all girders have a similar stiffness in state I (elastic) but a visibly different stiffness in state II (cracked). Table 4.13

reports the stiffness of each girder estimated through their trilinear idealised flexural response, and Table 4.14 reports the loads corresponding to the changes in structural states.

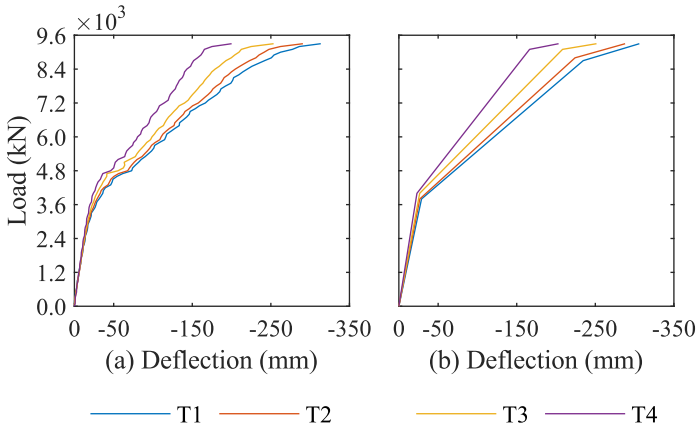

Figure 4.18 (a) Envelope of the vertical deflection at the girders' midspan plotted against the load and

State	T1 – k [kN/mm]	T2 – k [kN/mm]	T3 – k [kN/mm]	T4 – k [kN/mm]
I – Elastic	131.71	142.55	151.00	173.83
II – Cracked	23.82	25.32	28.04	35.58
III – Post-failure	8.40	7.84	4.64	5.42

Table 4.13 Stiffness of each girder estimated through their trilinear idealised flexural response

State change	T1 – Load [kN]	T2 – Load [kN]	T3 – Load [kN]	T4 – Load [kN]
I – II	3800	3800	4000	4000
II – III	8700	8800	9100	9100

Table 4.14 Loads corresponding to the change from state I to II and from state II to III of each girder

Figure 4.19 shows a comparison between the predicted and the observed deflections at the midspan of the girders. The predictions result from hypotheses A, B, and C of model ANA1, hypotheses B and C of model ANA2, and hypothesis C of model FEM1 and FEM2. Table 4.15 reports the stiffness of each girder resulting from the prediction models, and Table 4.16 reports the loads corresponding to changes in the structural states.

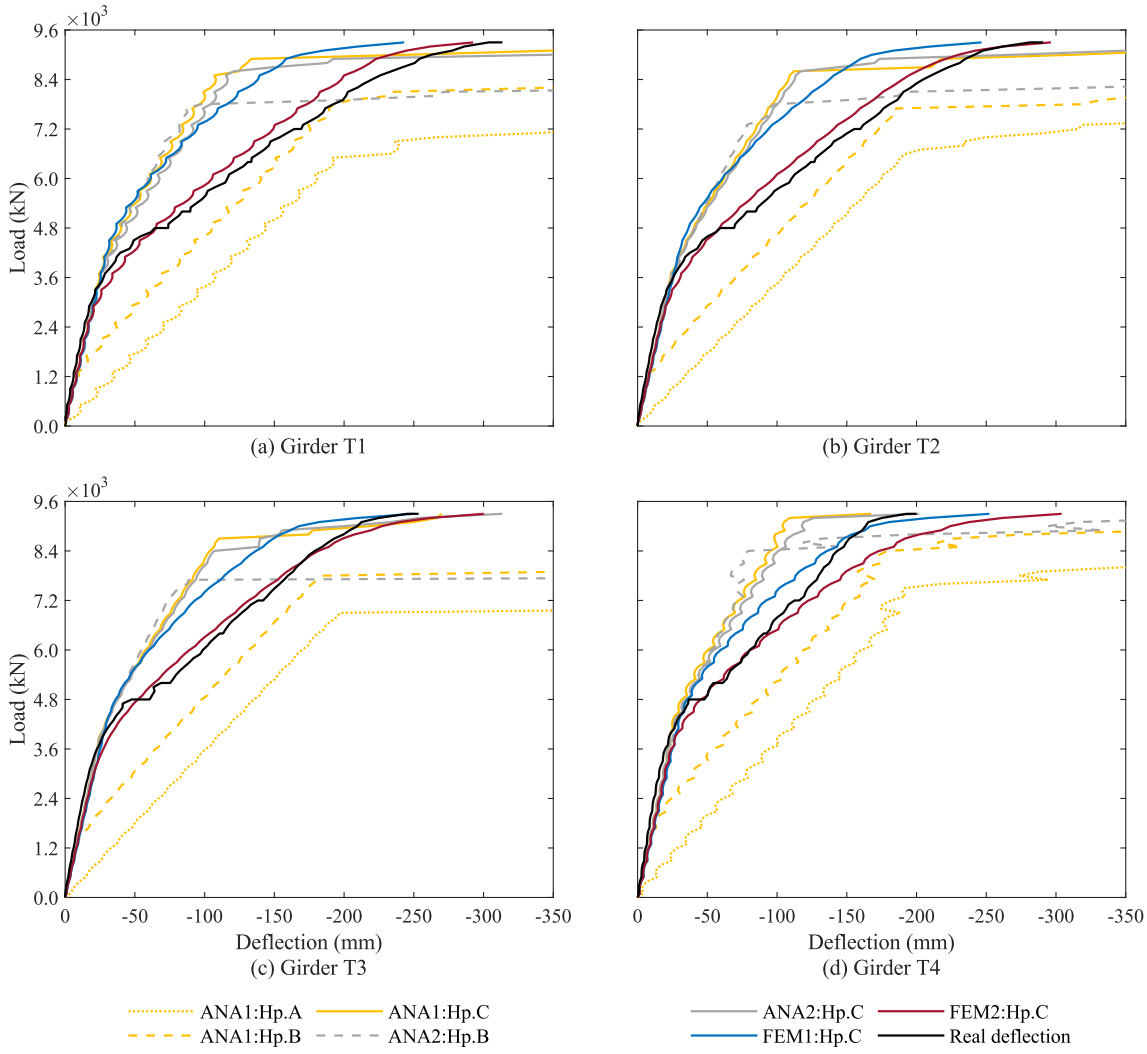

Figure 4.19 Comparison between the predicted and the observed deflections at the midspan of girders (a) T1, (b) T2, (c) T3, and (d) T4

k [kN/mm]		Hp. A				Hp. B				Hp. C			
Model	State	T1	T2	T3	T4	T1	T2	T3	T4	T1	T2	T3	T4
ANA1	I	33.06	34.14	35.09	37.32	121.2	140.22	147.2	143.03	144.8	152.72	158.44	166.43
	II	5.68	5.26	0.36	2.3	34.77	35.66	36.41	38.21	48.89	54.78	55.04	56.78
	III	1.53	1.33	2.15	-	1.4	1.82	2.21	2.91	1.27	2.02	3.56	1.72
ANA2	I	-	-	-	-	136.29	141.44	146	150.15	130.96	135.23	132.70	147.55
	II	-	-	-	-	63.24	67.26	66.2	55.91	51.52	53.37	58.82	52.42
	III	-	-	-	-	0.69	1.28	0.97	1.69	2.20	2.15	3.32	2.43

FEM1	I	-	-	-	-	-	-	-	-	133.55	130.70	142.42	160.00
	II	-	-	-	-	-	-	-	-	32.89	30.42	33.57	22.20
	III	-	-	-	-	-	-	-	-	4.71	5.15	3.25	9.06
FEM2	I	-	-	-	-	-	-	-	-	130.00	125.68	133.33	156.32
	II	-	-	-	-	-	-	-	-	25.92	25.63	36.55	27.59
	III	-	-	-	-	-	-	-	-	5.75	4.52	2.25	2.94

Table 4.15 Stiffness of each girder predicted by the structural models

Load [kN]		Hp. A				Hp. B				Hp. C			
Model	State	T1	T2	T3	T4	T1	T2	T3	T4	T1	T2	T3	T4
ANA1	I – II	6500	6600	6900	7600	1500	1400	1600	2000	4400	4000	4200	4600
	II – III	7000	7400	7000	-	7700	7700	7700	8500	8700	8600	8700	9200
ANA2	I – II	-	-	-	-	3900	3900	3900	4000	3900	3900	3900	4000
	II – III	-	-	-	-	7700	7700	7700	8400	8600	8600	8700	9200
FEM1	I – II	-	-	-	-	-	-	-	-	4900	4900	4700	4800
	II – III	-	-	-	-	-	-	-	-	8900	8900	9000	9000
FEM2	I – II	-	-	-	-	-	-	-	-	3900	3900	4000	4200
	II – III	-	-	-	-	-	-	-	-	8900	9000	9000	9000

Table 4.16 Loads corresponding to the change in the structural states predicted by the structural models

4.5.2 Errors in predictions

In this Subsection, we analyse whether the observed structural stiffnesses in states I, II, and III, the first-crack loads, and the failure loads align with the predictions, and we quantify the prediction errors. Then, we discuss the rationale and the procedure of the model updating we performed. Table 17 reports the errors in the prediction of stiffnesses, and Table 4.18 reports the errors in the prediction of loads.

Error in k [%]		Hp. A				Hp. B				Hp. C			
Model	State	T1	T2	T3	T4	T1	T2	T3	T4	T1	T2	T3	T4
ANA1	I	-74.9	-76.1	-76.8	-78.5	-7.98	-1.63	-2.52	-17.7	9.94	7.13	4.93	-4.26

	II	-13.8	-14.1	-18.3	-19.2	8.31	7.25	5.54	1.51	19.0	20.7	17.9	12.2
	III	-5.22	-4.57	-1.7	-	-5.31	-4.22	-1.61	-1.44	-5.41	-4.08	-0.72	-2.13
	I	-	-	-	-	3.48	-0.78	-3.31	-13.6	-0.57	-5.14	-12.1	-15.1
ANA2	II	-	-	-	-	29.9	29.4	25.8	11.7	21.0	19.7	20.4	9.69
	III	-	-	-	-	-5.85	-4.60	-2.43	-2.15	-4.71	-3.99	-0.88	-1.72
	I	-	-	-	-	-	-	-	-	1.40	-8.31	-5.68	-7.96
FEM1	II	-	-	-	-	-	-	-	-	6.89	3.57	3.66	-7.70
	III	-	-	-	-	-	-	-	-	-2.80	-1.88	-0.92	2.10
	I	-	-	-	-	-	-	-	-	-1.30	-11.8	-11.7	-10.1
FEM2	II	-	-	-	-	-	-	-	-	1.59	0.22	5.64	-4.60
	III	-	-	-	-	-	-	-	-	-2.01	-2.33	-1.58	-1.43

Table 4.17 Errors in the stiffness prediction. Error = (prediction – observation)/(observation of kI) × 100 [%]

Error in load [%]		Hp. A				Hp. B				Hp. C			
Model	State	T1	T2	T3	T4	T1	T2	T3	T4	T1	T2	T3	T4
ANA1	I – II	31.0	31.8	31.8	39.6	-26.4	-27.3	-26.4	-22.0	6.90	2.27	2.20	6.59
	II – III	-19.5	-15.9	-23.1	-	-11.5	-12.5	-15.4	-6.59	0.00	-2.27	-4.40	1.10
ANA2	I – II	-	-	-	-	1.15	1.14	-1.10	0.00	1.15	1.14	-1.10	0.00
	II – III	-	-	-	-	-11.5	-12.5	-15.4	-7.69	-1.15	-2.27	-4.40	1.10
FEM1	I – II	-	-	-	-	-	-	-	-	12.64	12.50	7.69	8.79
	II – III	-	-	-	-	-	-	-	-	2.30	1.14	-1.10	-1.10
FEM2	I – II	-	-	-	-	-	-	-	-	1.15	1.14	0.00	2.20
	II – III	-	-	-	-	-	-	-	-	2.30	2.27	-1.10	-1.10

Table 4.18 Errors in the load prediction. Error = (prediction – observation)/(observation of Load II – III) × 100 [%]

Model ANA1. The predictions of the structural response provided by the model ANA1 result from the hypotheses defined based only on the design documentation and NDTs on material specimens, without any evidence of the actual response of the bridge during the load test. The differences between that prediction and the response measured by the monitoring system raise the following observations:

- Elastic stiffness (slope of state I): the predictions from hypotheses B and C align with the observations.

- Cracked stiffness (slope of state II): the predictions are higher than the observations; predictions resulting from hypothesis B are more likely than from hypotheses A and C.
- Post-failure stiffness (slope of state III): the predictions are slightly lower than the observations.
- First-crack load (change from state I to II): hypothesis C's predictions align with the observation, while hypotheses A and B are very different.
- Failure load (change from state II to III): the predictions from hypotheses A and B are lower than the observations, while hypothesis C seems more likely.

The prediction errors strongly depend on the hypotheses of materials. The main differences are (i) in the elastic stiffness, with error > 70% in hp. A, and error < 10% in hp. C; and (ii) in the first-crack load, with error > 30% in hp. A, error < 7% in hp. C. The first crack load is particularly sensitive to the residual stress in prestressing cables; thus, it must be accurately estimated with NDTs.

Model ANA2. We updated the analytical model ANA1 by changing the residual stress of prestressing cables to make the predicted first crack loads as close as possible to the observed ones. Table 4.5 of Subsection 4.3.3 reports the updated values of residual stress. In addition, we neglected material hypothesis A since it seemed excessively precautionary.

As a result, the predictions of model ANA2 result from hypotheses defined based on the design documentation, NDTs on material specimens, and a diagnostic load test on the bridge (previously uncracked) carried on until the first crack opens and without any evidence of the cracked stiffness and ultimate capacity. The differences between that prediction and the response measured by the monitoring system raise the following observations:

- Elastic stiffness: predictions are in line with the observation.
- Cracked stiffness: predictions are still higher than the observation; this time, prediction from hp. C is more likely than hp. B.
- Post-failure stiffness: predictions are slightly lower than observations; they do not change while changing the residual stress.
- First-crack load: hypotheses B and C predictions are now almost equivalent to the observations.
- Failure load: predictions do not change while changing the residual stress; therefore, hypothesis C is still more likely than B.

From a load test carried on until the fist-crack opening, it is possible to learn the elastic response of the bridge – elastic stiffness and first-crack load – and update the model so that its prediction of elastic response better fits the observation. In particular, we can update the residual stress of prestressing steel, which is difficult to estimate with NDTs and strongly influences the first-crack load of PC girders. However, this load test will crack the structural elements; therefore, it might be unsuitable for an in-service bridge. After the model updating, the prediction error on the first crack load decreased from a mean value of 20% to around 1%. On the other hand, the prediction error on the cracked stiffness changed only slightly, as well as the error in the prediction of the ultimate capacity and the post-failure stiffness; that is because they typically do not change while changing the residual stress.

Model FEM1. To better fit the response of the bridge measured during the entire load test, we developed a finite element model FEM1 with the hypotheses described in Subsection 4.3.3. As far as the properties of the materials, we considered only hp. C.

The predictions of model FEM1 result from the same hypotheses as ANA2; however, it is a finite element model with more refined geometry and non-linear stress-strain relations. The differences between that prediction and the response measured by the monitoring system raise the following observations:

- Elastic stiffness: prediction is in line with the observation but slightly lower.
- Cracked stiffness: prediction is closer to the observation than before but still slightly higher.
- Post-failure stiffness: prediction is in line with the observation; the comparison is easier to perform for girder T3 and T4 since they experienced a more extended post-failure response.
- First-crack load: prediction is now higher than observation; a further update of the residual stress of prestressing cables is needed.
- Failure load: prediction is in line with the observation.

The results are similar to those obtained from model ANA2, apart from the first-crack load. The prediction errors increased because we used the residual stress updated ad hoc to make the prediction of ANA2 fitting better the observed response. However, the updated residual stress value did not bring the same result for the model FEM1. Not surprisingly, the output of a parameter updating process depends strongly on the model; if we change the model, we must update the parameters again to make the new model fit the observation.

Model FEM2. We performed a sensitivity analysis on the parameters of the model FEM1 to better establish their influence on the model prediction and select their values that make the model predictions better fit the observed response during the entire load test. We tested all their possible combinations in a range of [-10%, +10%] of their nominal value used in the model FEM1. The results of the sensitivity analysis suggest that:

- Elastic stiffness is strongly influenced by the elastic modulus of the girders' concrete. That aligns with what we expected, given the well-known theory of beams and the constitutive laws of materials. Other parameters do not significantly influence the predicted response in state I.
- Cracked stiffness depends mainly on the residual stress of prestressing cables and slightly on the tensile strength of concrete. According to the theory of prestressed beams, PC girders should not be affected by this parameter once the crack has occurred; however, the first-crack load is affected by the residual stress, affecting the cracked stiffness in turn.
- First-crack load depends on the concrete's tensile strength and the prestressing cables' residual stress. Therefore, we achieved an improvement by decreasing the residual stress, which resulted in a decrease in the predicted first-crack load. This change does not affect the ultimate load. Other parameters do not significantly affect the predicted response in state II.
- Ultimate capacity depends on concrete's tensile and compressive strength, the yield and ultimate tensile strength of prestressing steel, and the ultimate strain of concrete and steel. It does not depend much on the elastic modulus of the concrete and the residual stress of prestressing steel; therefore, its predicted value has never changed much between different models.

As a result, the most influential parameters of the finite element model of the viaduct are:

- E*c*: the elastic modulus of the concrete for structural elements in state I.
- $\sigma_{p,\infty}$: the residual stress of prestressing steel for structural elements in state II.

Table 4.6 of Subsection 4.3.3 reports the updated values of the prestressing steel's residual stress and the concrete's elastic modulus. We observe that the prestressing cables have lost considerable tension over time and that the loss has been non-uniform between the girders. Indeed, the girder T1 lost around 30% of the initial prestressing tension, the girders T2 and T3 around 20%, and the girder T4 less than 10%. Looking at Table 17 and Table 18, we note

a marked improvement in the model predictions from model FEM1 to model FEM2. The elastic, the cracked, and the post-failure predicted response align with the observation, and differences are negligible (error < 10 % for the stiffness, error < 3% for the load).

From a load test carried on until the bridge's failure, it is possible to learn the bridge's elastic, cracked, and post-failure response, the first crack load of its structural elements, and its ultimate capacity. However, such a load test will collapse the bridge; therefore, it is not unsuitable for an in-service bridge.

The prediction of the structural response becomes more accurate as the load test provides more information to update the structural model. The only difference is between model ANA2 and FEM1, where some quantities are better predicted by ANA2 than FEM1, as explained in Subsection 4.5.2. Figure 4.20 shows the variation of the prediction errors between the models. Quantities are expressed here in absolute value.

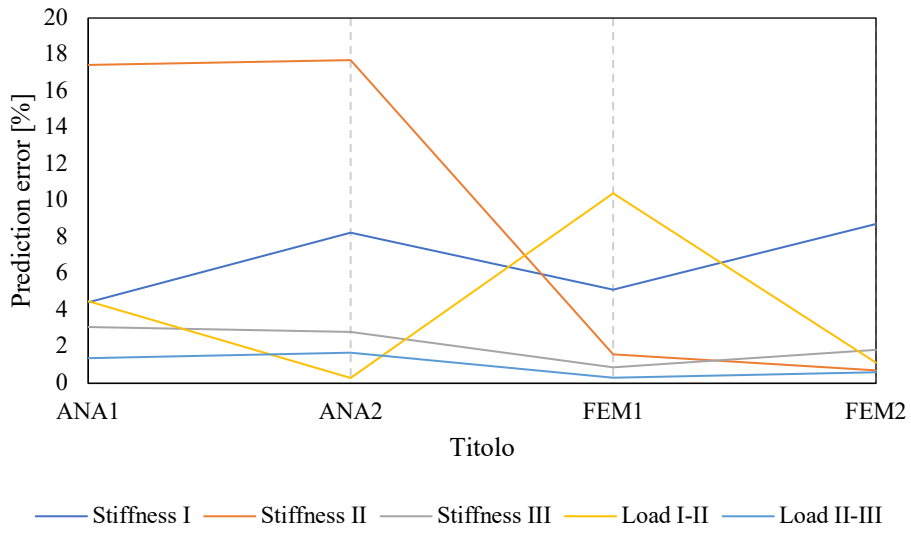

Figure 4.20 Differences between model predictions and observed response. Quantities are expressed in % respect to the observed value of the elastic stiffness and ultimate capacity, respectively. Error = abs (observation – prediction)/observation %

4.5.3 Load test utility for model updating

This Subsection focuses on the question, "What can we learn from a load test?". A load test can provide useful information on the condition state of a bridge. We can use it to update the parameters of a model to improve its prediction of the structure response; however, different load tests provide different information with different impacts on the model updating. We represent different load tests with our five loading phases P1 – P5 and different levels of

model updating with our four prediction models. We aim to verify whether diagnostic load test of the bridge's elastic response or proof tests with higher loads allow to:

- Discriminate whether the bridge has preexisting concrete cracks or not.
- Identify the opening of the first crack during the load test.
- Estimate the prestressing cables' residual stress.
- Update the structural model to predict the ultimate capacity of the bridge better.

Elastic vs cracked response. The loading phases P1 and P2 tested the elastic response of the bridge because it had no preexisting cracks, and the resulting bending moments in the girders did not exceed the yield strength of materials. In contrast, the loading phase P3 opened the first cracks in the girders. Finally, the loading phases P4 and P5 tested the cracked response of the bridge because the bridge experienced the initiation and propagation of cracks during the previous phase, P3.

Green lines in Figure 4.12 and Figure 4.14 of Subsection 4.4.3 (phases P1 and P2) clearly show the linear elastic response of the bridge and point out the absence of preexisting cracks in all girders since no residual vertical deflections nor longitudinal deformation remains after the unloading of the span. The same result comes from the acoustic emission sensors on girders T2 and T3 and the modal analysis. We did not observe any acoustic emissions from concrete cracks during the loading and unloading phases P1 and P2 (extensive results are in Chapter 5). Moreover, the first flexural and the first torsional frequencies do not change after P1 and P2. In contrast, the amber lines (phases P3) in Figure 4.12 and Figure 4.14 show a sharp change in the slope due to a change in the girders' response: from state I to state II. The acoustic emissions sensors confirm that (see Chapter 5); they suddenly started recording a high number of high-amplitude and high-strength signals, which identifies the behaviour change of girders T2 and T3. Also, the modal analysis confirms that; Figure 4.17 shows a reduction of around 0.2 Hz of both the first flexural and the first torsional frequencies after the unloading phase of P3.

Finally, the red dashed lines (phase P4) in Figure 4.12 and Figure 4.14 show a non-linear response starting from the beginning of the loading phase: the stiffness is half of what was observed during phases P1 and P2, and a residual deflection and deformation remains after the unloading of the bridge. Acoustic emission sensors recorded many signals from cracks opening and propagation, as reported in, [133], and the modal analysis shows a further reduction of 0.2 Hz after P4.

The prediction of model ANA1, whose parameters we have estimated only based on design documentation and NDTs of material specimens, identified the elastic stiffness with good accuracy: error < 20% (with hp. B and hp. C).

As a result, regular diagnostic tests up to the design traffic load can effectively discriminate whether a PC bridge has preexisting concrete cracks or not by comparing the observed stiffness with the predicted one. When the observation is slightly different from the prediction (error < 20%), the bridge is likely uncracked; the analyst can update the elastic modulus of concrete to have a more accurate prediction of its elastic response. A regular diagnostic test can also point out whether the opening of the first crack happens during the test and identify precisely the first-crack load.

Residual stress of prestressing cables. We observed that the residual stress of prestressing cables mainly influences the first-crack load, which in turn influences the stiffness in state II. Therefore, a regular diagnostic load test of an uncracked bridge cannot provide useful information to estimate it accurately. For an accurate residual stress estimation, the load test should identify the first-crack load; then, we can identify the updated residual stress by forcing the model prediction to crack at the same load, as we did with models ANA2. However, this procedure might be unsuitable for in-service bridges that must stay uncracked. The residual stress is probably just fine if bridges are still uncracked after 50 years. Moreover, residual stress typically does not influence the ultimate capacity; therefore, its accurate knowledge is generally not mandatory to verify the structural reliability of the bridge.

On the other hand, a diagnostic test up to a higher load than the predicted first-crack load can provide evidence of the cracked stiffness of a cracked bridge without a considerable increase in the damage level. In this case, the first-crack load will not show a marked change in the response as in the uncracked bridge. As a result, the residual stress can be better estimated. The knowledge of the residual stress is more important for a cracked bridge since it influences its serviceability (deflection) and durability (cracks propagation).

Prediction of ultimate capacity. We observed that the ultimate capacity of the bridge depends mainly on the tensile and compressive strength of the concrete, the yield and ultimate tensile strength of prestressing cables, and the ultimate strain of concrete and steel. Therefore, load tests of the elastic response of the bridge do not provide any useful information about the ultimate capacity, nor do load tests that exceed the first-crack load.

However, all prediction models with material hypothesis C provide a pretty good estimation of the ultimate capacity, even the model ANA1. The prediction errors are all lower than 5%. Therefore, it seems more important to perform an extensive NDTs campaign on material specimens to estimate the material properties accurately rather than load tests. A load test to failure is not an option to identify the ultimate capacity of a particular bridge since it would have to be dismissed after the load test.

Testing a bridge to failure can be particularly informative if that bridge has already been dismissed and is part of an asset that consists of many bridges with similar structural type, age, and deterioration state as the Alveo Vecchio viaduct was. Indeed, the load test described in this paper allowed us to verify that the ultimate moment resistance of the Alveo Vecchio viaduct has been almost four times what the design documentation reported. Most Italian bridges with similar characteristics are likely to have a similar ultimate capacity, or at least they can carry the design traffic load without much distress. However, particular attention should be paid to structures in marine, industrial, and aggressive environments, where the corrosion might induce an accelerated degradation and, consequently, an accelerated reduction of structural capacity and durability.

4.6 Conclusions

As civil infrastructure ages and the volume of road traffic increases, it is crucial to verify that bridges older than 50 can carry the new traffic loads without distress. Numerical models can predict their operational response to traffic loads and their ultimate capacity with low uncertainties; however, such uncertainties increase as bridges age due to deterioration mechanisms. Non-destructive tests on material specimens increase the knowledge of materials' properties; on-site diagnostic and proof load tests provide different information on the structural health state depending on the load applied during the test.

This paper summarises the research activity performed at the MIMS Infrastructure Safety Test Field set up at the Alveo Vecchio viaduct in Italy. The structure is a decommissioned PC bridge representing 52% of the Italian highway bridges in terms of structural type, age, and deterioration state. We subjected it to a load test performed in five phases with a progressively increasing load up to its failure. We measured its static and dynamic response with an extensive structural health monitoring system during the entire load test. We reported it in this manuscript, along with a detailed description of the design and execution of the test. In addition, we developed an analytical and a FE model of the structure. We progressively

updated them based on non-destructive tests of material specimens and monitoring system results acquired during the test. This paper compares the structure's observed response during the load test with its predicted response by structural models. A detailed discussion follows. First, the paper discusses what engineers can observe and learn from a load test as the load progressively increases (e.g., stiffness, first-crack load, ultimate capacity). Then, it identifies the model parameters that influence the response prediction the most. Finally, it verifies whether a diagnostic load test up to the design traffic load allows verifying whether: (i) the structural response is elastic during the entire load test; (ii) the bridge cracks during the load test; (iii) the bridge was already cracked before the load test. The main results are:

(1) The elastic modulus of concrete was the parameter that influenced the elastic stiffness the most; the residual stress of prestressing cables was the parameter that influenced the first-crack load and the crack stiffness the most.

(2) The ultimate capacity seemed to depend mainly on the tensile and compressive strength of the concrete, the yield and ultimate tensile strength of prestressing cables, and the ultimate strain of concrete and steel.

(3) Both analytical and FE models based only on the design documentation and NDTs of material specimens predicted the girders' elastic stiffness with an error of $< 20\%$ and the ultimate capacity with an error of $< 5\%$ when NDTs carefully estimated the material properties.

(4) The load test up to the design traffic load allowed recognising whether the PC bridge had preexisting concrete cracks by comparing the observed stiffness with the predicted one.

(5) The load test effectively pointed out whether the opening of the first crack happened or not during the loading phases, showing a sharp change in the slope of the load-deflection graph. The first-crack load was clearly detectable.

(6) When the PC bridge had no preexisted cracks, the load test up to the design traffic load did not provide useful information to estimate the residual stress of prestressing cables. To have them, we had to crack the girders, which is not an option for in-service bridges. To estimate the residual stress, performing NDTs of material specimens is preferable.

(7) When the PC bridge was already cracked, the load test with a higher load than the predicted first-crack load did not show a marked change in the observed response as in the uncracked bridge. That allowed measuring the cracked stiffness without a considerable increase in the damage level.

(8) Load tests of the elastic response did not provide information about the ultimate capacity, nor did load tests that exceeded the first-crack load. The last load test (which collapsed the bridge) did it; however, a load test to failure is not an option for in-service bridges since they would have to be dismissed after the load test.

(9) A load test up to a bridge failure can be particularly informative if that bridge has already been dismissed and is part of an asset that consists of many bridges with similar structural type, age, and deterioration as the Alveo Vecchio viaduct was.

The load test described in this paper allowed us to verify that the ultimate moment resistance of the Alveo Vecchio viaduct was almost four times what the design documentation reported.

5 STRUCTURAL HEALTH MONITORING BASED ON ACOUSTIC EMISSIONS: VALIDATION ON A PRESTRESSED CONCRETE BRIDGE TESTED TO FAILURE

Abstract: The increasing number of bridges approaching their design life has prompted researchers and operators to develop innovative structural health monitoring (SHM) techniques. An acoustic emissions (AE) method is a passive SHM approach based on the detection of elastic waves in structural components generated by damages, such as the initiation and propagation of cracks in concrete and the failure of steel wires. In this paper, we discuss the effectiveness of AE techniques by analysing records acquired during a load test on a full-size prestressed concrete bridge span. The bridge is a 1968 structure currently decommissioned but perfectly representative, by type, age, and deterioration state of similar bridges in operation on the Italian highway network. It underwent a sequence of loading and unloading cycles with a progressively increasing load up to failure. We analyzed the AE signals recorded during the load test and examined how far their features (number of hits, amplitude, signal strength, and peak frequency) allow us to detect, quantify, and classify damages. We conclude that AE can be successfully used in permanent monitoring to provide information on the cracking state and the maximum load withstood. They can also be used as a non-destructive technique to recognize whether a structural member is cracked. Finally, we noticed that AE allow classifying different types of damage, although further experiments are needed to establish and validate a robust classification procedure.

5.1 Introduction

An increasing number of civil infrastructures are approaching or exceeding their initial design life. For instance, the average age of bridges in the USA is estimated to be 46 years [134]; similarly, 70% of highway bridges in Italy were reportedly built around the 1970s [135]. As infrastructure ages, the effort required by operators to identify unsafe structural conditions increases. The benefit of structural health monitoring (SHM) to bridge management has been extensively analysed in the literature, see for instance [12]; SHM allows the early detection of possible damages resulting from the natural deterioration of structural materials, and to optimize decision over maintenance, repair, and reconstruction of the bridge asset [98] [136].

The growing interest in SHM for infrastructure operators and the recent technological progress have encouraged the research community to study and develop innovative sensors and monitoring methods. An incomplete list includes the Ground Penetration Radar (GPR),

or Georadar [65] [64], the Reflectometric Impulse Measurement Technology (RIMT) [67] [66], [68], the Time Domain Reflectometry (TDR) [69], [70], the Strand-Cutting test [71], [72], [73], the Core Drilling Method (CDM) [74], [75], and the Acoustic Emissions technique (AE) [45]. All these techniques have been studied in laboratory experiments and in-service structure monitoring; however, the absence of standardized procedures and the unavoidable need of experts to interpret results make these technologies unready for an extensive application on civil infrastructure yet. It is necessary to validate such technologies and define specific protocols to guarantee the accuracy and reproducibility of their results, which any qualified practitioner should be able to interpret. That is necessary to obtain effective monitoring information for infrastructure management [137], [138].

In this contribution, we focus on the AE technique. It is a passive monitoring approach based on the detection of elastic waves in structural components generated by damages, such as the initiation and propagation of cracks, the failure of steel wires, and the failure of bonds [34]. Its primary goal is to detect, locate, and assess the intensity of damage [45] in a non-invasive way, both when the structure is in-service and during load tests. Its application in SHM started much later compared to other fields, such as the aerospace industry [34]. The interest has increased because elastic waves generated by damages propagate throughout the structure; therefore, it is possible to remotely detect damages in areas that are not easily accessible to visual inspections and direct measurements [34].

Numerous laboratory studies on crack detection based on AE have been conducted on specimens representative of in-service structures, both on steel members [35], [36], [37] and concrete samples [38], [39], [40]. In addition, field-testing applications have been carried out on large-scale structures, such as bridges, nuclear power plants, containment structures like silos, bins, and water storage tanks [41], and prestressed concrete pipes exposed to corrosion phenomena [42]. Applications of AE for damage monitoring in masonry structures are also reported in the literature [43].

The use of AE in bridge monitoring dates back to the 1970s when Pollock and Smith monitored for the first time a portable military bridge subjected to proof testing [44]. After this experiment, AE technology has been used in numerous field bridge testing applications [45], addressing the detection of concrete cracks initiation and propagation, the development of fatigue cracks in steel members, the failure of prestressed tendons in prestressed reinforced concrete elements, and the break of wires in cable structures. A comprehensive review of AE monitoring applications on bridges from 1970 to 2010 is found in [45].

Golaski et al. [46] used AE monitoring for the safety assessment of five full-scale bridges of different types: reinforced concrete, prestressed concrete—both post-tensioned and pre-tensioned—and steel-concrete composite. They claimed that the AE method is useful for evaluating the integrity of bridges; however, individual evaluation-criteria must be selected for each structural type. Nair and Cai [45] focused on the condition assessment of a prestressed concrete slab-on-girder bridge and a steel bridge with a concrete deck under live loads. Anay et al. [47] worked on the damage identification in a three-span prestressed concrete girder bridge with pre-existent inclined cracks during a load test and used AE tests to classify crack extensions as stable or unstable.

Many experiments have specifically addressed the crack opening and propagation in concrete elements. Chataigner et al. [48] realized several real-size experimental investigations on a prestressed concrete girder taken from a decommissioned viaduct, carrying out both flexure and shear tests up to failure and using several measurements methods, including AE. They claimed that it is possible to learn additional information on the structure's state of damage by comparing results from traditional crack-opening sensors and AE sensors. They also compared the results with the prediction from a finite-element-model and with the results of an autopsy of the beam carried out by hydro demolition; they found a good correlation, even though they observed undetected damages during the autopsy. Recently, Ma and Du [49] applied a machine learning algorithm based on a Deep Neural Network model to combine some of the most common AE signal parameters to assess the rate of crack-opening on prestressed concrete structures. They found interesting results on the correlation between AE parameters and crack-opening events for different loads; however, they recognized some limitations in the approach.

Other research works have focused on AE as a means to detect failures of tendons in prestressed concrete bridges. Fricker and Vogel [51] monitored a small prestressed concrete bridge to evaluate the performance of permanent AE monitoring and demonstrated that it is possible to detect wire breaks with good localization accuracy. Yuyama et al. [50] carried out both laboratory and field tests: laboratory tests were conducted on three types of post-tensioned beams (with steel bars, strands, and parallel wire cables), while field tests were performed on two post-tensioned bridges. They found that it is easy to discriminate meaningful AE due to wire breaks from traffic noise and hammering and claimed that AE is a promising method to detect and locate wire breaks. Shiotani et al. [139] studied cable breakages and the subsequent failure process using a full-scale post-tensioned prestressed

concrete beam subjected to a four-point bending; they simulated the breakage of cables by reducing their stress in turn and identified breakage areas and failure areas of grout material based on AE.

The AE analysis has recently addressed the problem of corrosion in prestressed concrete structural components exposed to saltwater tides and splashing. Vélez et al. [52] carried out some laboratory experiments on a full-scale prestressed concrete specimen representative of outer portions of bridge piles exposed for one year to saltwater wet/dry-cycles mimicking natural tidal action; they stated that the AE technique is efficient to evaluate and detect corrosive phenomena.

In summary, most of the experimental verifications of AE techniques reported in the literature are based on tests carried out in laboratory conditions on specimens or individual structural elements. There are also a number of works that investigate the performance of AE methods on full bridges in operation. However, not that surprisingly, these experimental works are typically concerned with damage states that do not jeopardize the safety of the bridge, and they do not provide direct verification on how well an AE technique performs when the bridge is close to collapse. Indeed, we are not aware of any experiment on a full-scale bridge that verifies the capacity of AE to provide an early warning when the bridge is approaching its ultimate state.

In this paper, we wish to bridge this gap by analyzing and discussing the AE recorded during a load test on a full-size prestressed concrete bridge span, carried out up to the bridge failure. The bridge, the Alveo Vecchio viaduct, is a 1968 structure currently decommissioned but perfectly representative, by type, age, and deterioration state of similar bridges currently in operation on the Italian highway network. Our goal is to discuss how the AE change while the load progressively increases and compare the results with those provided by other sensors installed on the structure: linear variable differential transformers (LVDT) for the cracks detection and rotary variable differential transformers (RVDT) for the bridge deflection. We aim to verify whether an AE monitoring system can provide useful information to (i) discriminate whether the viaduct has pre-existent damages, such as concrete cracks or broken steel wires; (ii) identify the opening of the first crack; (iii) single out the maximum load withstood by the viaduct; and (iv) recognize different types of damages. Particularly, we wish to identify the most sensitive features of AE that deserve to be extracted to establish the level, extent, and type of damage on a prestressed concrete bridge.

For those readers who are not familiar with AE, in the following Section 2, we briefly summarize the physical principle and the technology at the basis of the method, along with the most typical signal analysis techniques. Then, in Section 3, we describe the Alveo Vecchio case study, including details of the monitoring system installed and of the load test carried out. Section 4 reports the results of the AE acquired during the different phases of the test. We discuss these results in Section 5, by comparing them with the evidence recorded by LVDT and RVDT sensors. Finally, in Section 6, we draw conclusions about the application of the AE technique to real-life prestressed concrete bridges.

5.2 AE Principle and Observable Quantities

5.2.1 Phenomenon and Technology

The AE is a phenomenon in which transient elastic waves are generated by the rapid release of strain energy from a localized source due to microstructural changes in the material [140]. Elastic waves travel into the material and move to the surface of a structural element where sensors can detect them. Therefore, an AE monitoring system requires two components: a source, such as a crack propagation or a tendon failure; and a transducer, which receives and acquires the elastic wave [45]. Figure 5.1 shows the working principle of an AE monitoring system.

An elastic wave is a combination of longitudinal, transverse, and reflected waves, with a broadband frequency range from kHz to MHz [34]. Even though they are called acoustic emissions, elastic waves are neither acoustic (from 2 kHz to 20 kHz) nor ultrasonic (over 20 kHz) [141]. AE sensors are typically piezoelectric or PZT devices that transform the motion produced by the transient elastic wave into an electrical signal, which is digitized and stored [142]. The selection of the transducer's sensitivity and frequency response is critical for the effectiveness of the AE technique and depends on the characteristics of the monitored structure [143]. Capacitive MEMS AE transducers have been recently designed and tested [144], [145]; they are smaller and less expensive than piezometric sensors but have limited sensitivity and a working direction only normal to the surface on which they are installed [34].

When an elastic wave reaches the sensor, it is transduced into an electrical signal, recorded, amplified, and typically represented in a diagram with the time expressed in seconds (s) on the horizontal axis and the signal amplitude expressed in volts (V) on the vertical axis. The

signal is usually affected by background and environmental noise due to the wind and passers-by; therefore, the reduction of such noises requires a band-pass filter [141].

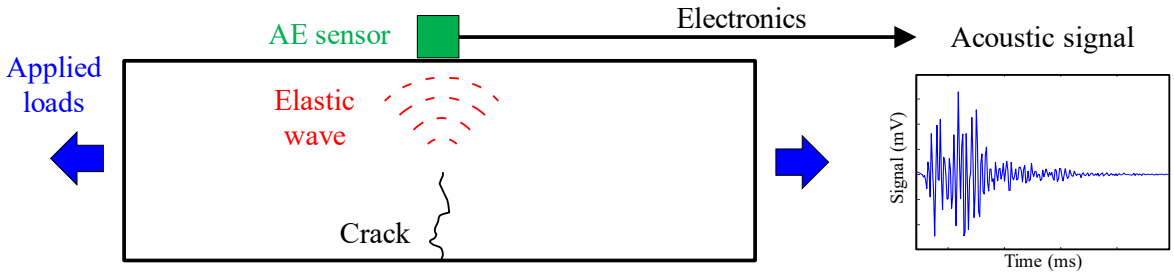

Figure 5.1 Working principle of an AE monitoring system.

5.2.2 AE Signal Parameters

The electrical signal identifies an acoustic event, also called a hit [146], when it crosses a certain threshold, expressed in volts (V) or similarly in decibels (dB). This threshold is defined as the minimum amplitude that the signal must have to be considered in the analysis [147]: typical values for reinforced concrete structures are around 40–45 dB [148], but sometimes it can be up to 60 dB [50], [149]. Moreover, the signal must cross the threshold at least three times consecutively to be one hit.

A hit can be described by characteristic parameters [147], which are defined in the time-domain, as represented in Figure 5.2, or in the frequency-domain, as represented in Figure 5.3. Here is a summary of the parameters we considered in our analysis.

- Amplitude: it is the maximum amplitude of the signal in the time-domain after its amplification. It is expressed in decibels and Vref = 1 μV from the sensor corresponds to 0 dB.
- Duration: it is the time interval between the first and the last threshold-crossing of a hit.
- Count: it is the number of times that the signal exceeds the threshold within the duration: it strongly depends on the threshold and the sampling frequency.
- Signal strength (energy): it is the measured area of the rectified signal envelope (MARSE). Typically, it includes the absolute value of areas of both the positive and negative envelopes. Its unit of measure is Volts × second [V·s], and it is a function of both the amplitude and the duration. It is preferred over count to interpret the magnitude of the event.

- Peak frequency: it is the frequency corresponding to the peak observed in the power spectrum resulting from an FFT (Fast Fourier Transformation) of the signal.

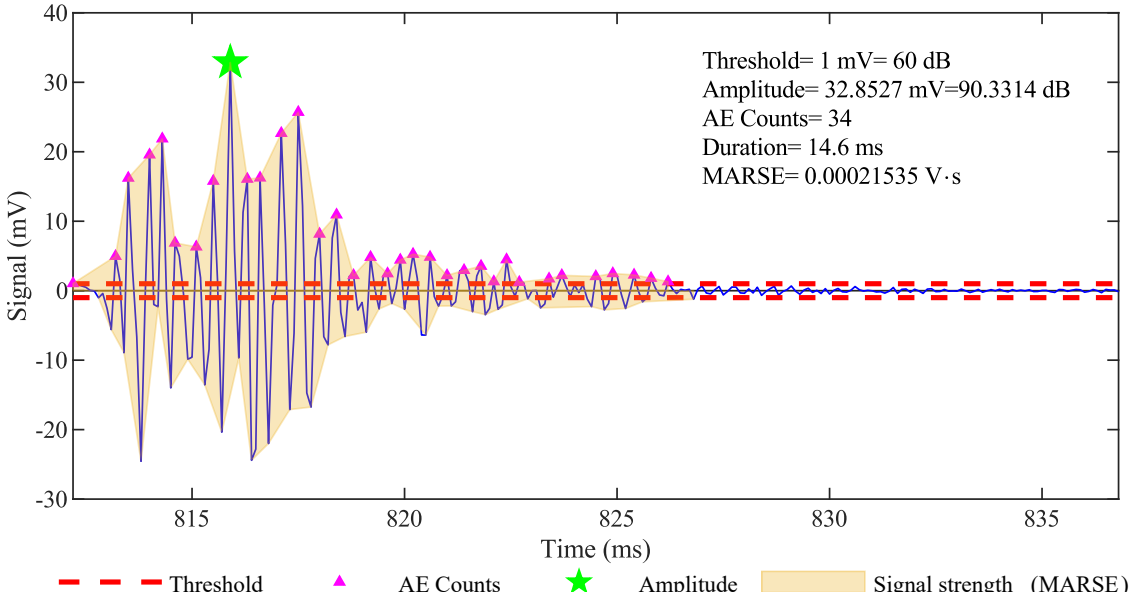

Figure 5.2 AE signal and parameters expressed in the time-domain.

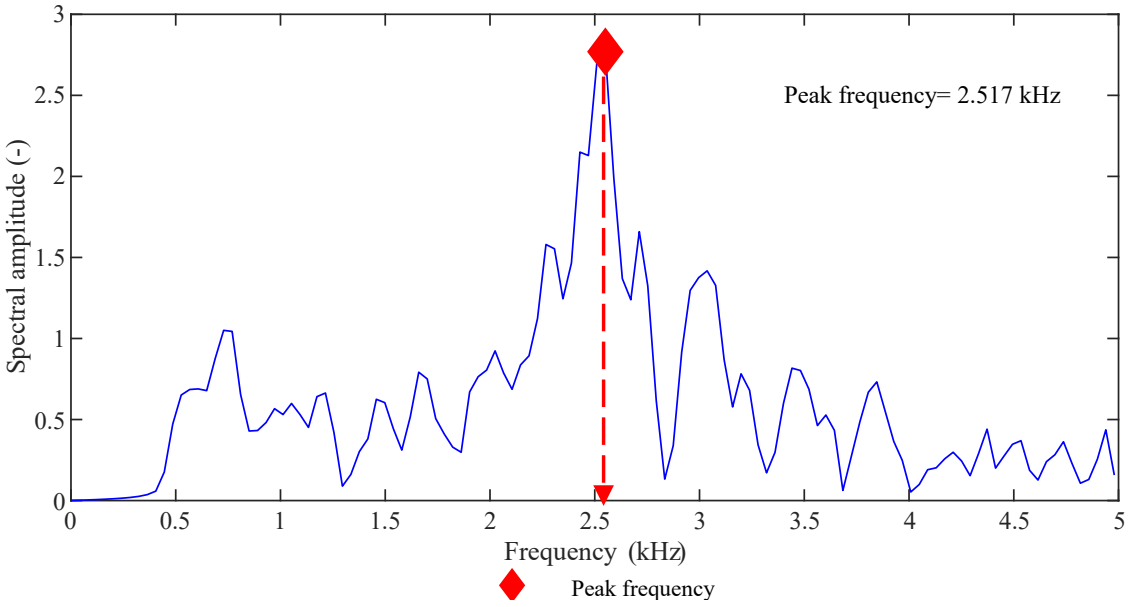

Figure 5.3 AE signal and parameters expressed in the frequency-domain.

To discriminate different acoustic events, we must select three time-parameters, PDT, HDT, and HLT, [150], [151], [152], represented in Figure 5.4. Their choice is critical for the correct identification of hits.

- Peak definition time (PDT): it is the time after the peak amplitude in which a new greater peak amplitude can replace the original one; after the PDT has expired, the original peak-amplitude is not replaced.

- Hit definition time (HDT): it is the time after the last threshold-crossing that defines the end of the hit.
- Hit lockout time (HLT): it is the time after the HDT during which a threshold-crossing will not trig a new hit. A new hit can start only after the HLT has expired.

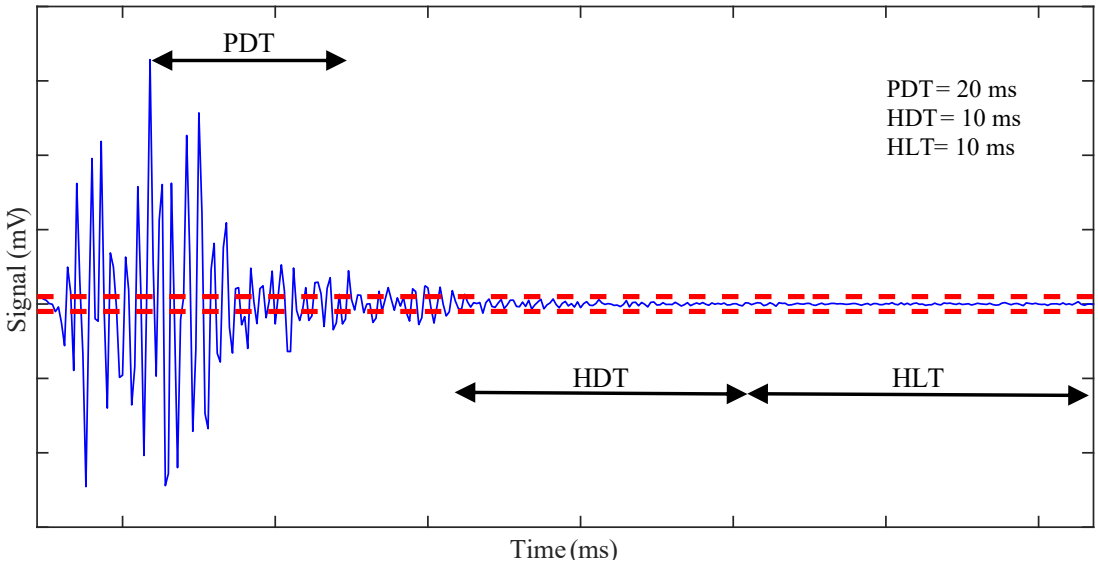

Figure 5.4 Peak definition time (PDT), hit definition time (HDT), and hit lockout time (HLT). They discriminate one hit from another.

5.2.3 AE Analysis for Load Tests

A structural element subjected to loading and unloading cycles experiences a propagation of damages and emits acoustic waves only when the previous maximum load level is exceeded [45]. The absence of AE during a loading phase is called the Kaiser effect [153] and happens only with an elastic behavior of the material. In the case of plastic deformations, the Kaiser effect is violated, and acoustic waves are emitted during all the loading phase; this phenomenon is called the Felicity Effect [153]. The Kaiser and the Felicity effects identified during load tests can highlight the presence of flaws or other structural damages and help to assess the integrity of the structural element.

5.3 Case Study of a Prestressed Concrete Bridge Tested to Failure

5.3.1 Alveo Vecchio Viaduct

In Chapter 3, we comprehensively examine the case study, the Alveo Vecchio viaduct. To enhance clarity, we present the viaduct's top view, lateral view, and cross-section in Figure 5.5. Additionally, Figure 5.6 showcases a transversal section of the girders with the prestressing cables, offering detailed insights into the structural configuration of the viaduct.

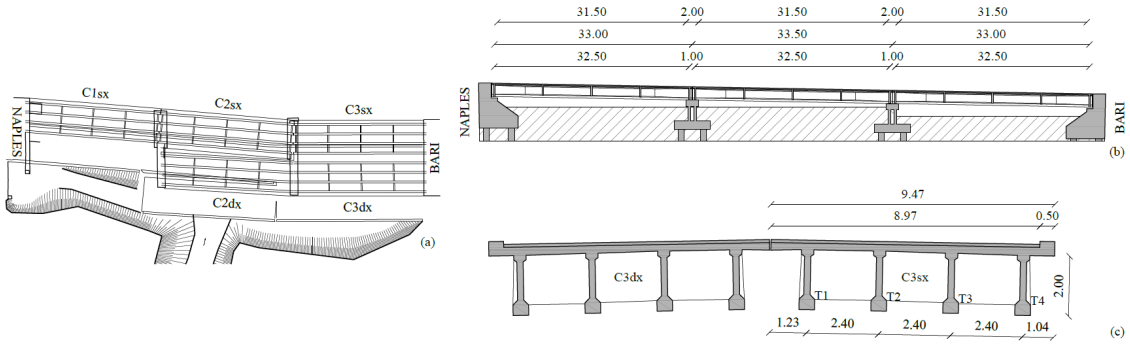

Figure 5.5 (a) top view; (b) lateral view; and (c) cross-section of the Alveo Vecchio viaduct (Italy)

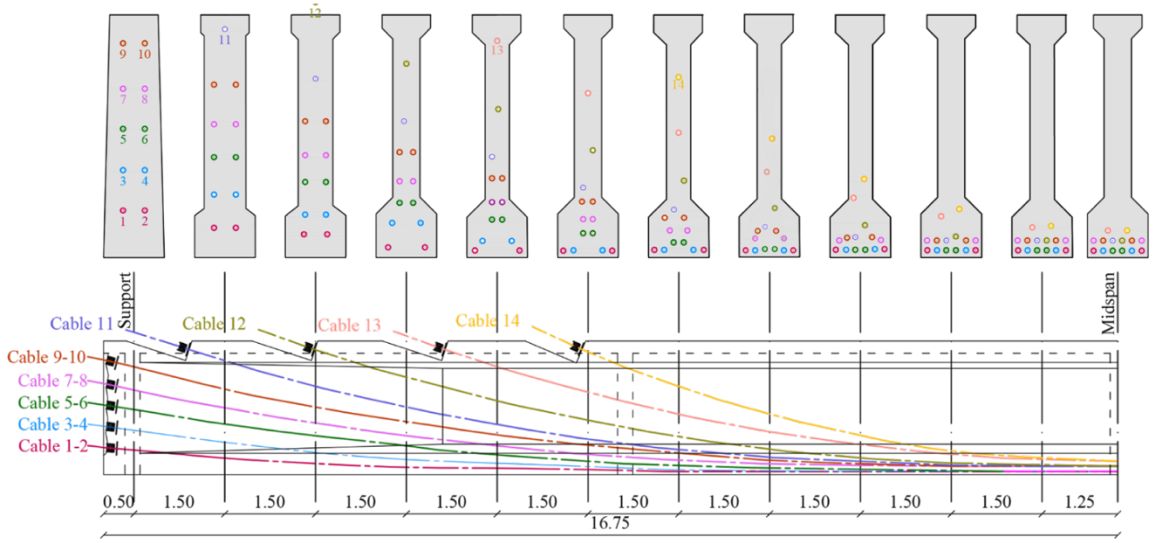

Figure 5.6 Longitudinal and transversal section of girders with post-tensioned cables

5.3.2 Structural Health Monitoring System

The monitoring system designed for the load test consists of 119 sensors divided into eight types: wire displacement sensors (RVDT), deformation sensors (strain gauges), crack-opening sensors (LVDT), electronic level, temperature sensors (RTD), inclinometers, accelerometers, and AE sensors. Furthermore, we monitored air temperature, air humidity, and wind speed. Details about the SHM system installed on the viaduct are in [154] (in Italian).

We focus on wire displacement sensors, crack-opening sensors, and AE sensors. Figure 5.7 shows the layout of these sensors on the viaduct, while Table 5.1 reports their technical features. The LVDT sensors are Gefran PZ12, while the RVDT sensors are PT1DC from Celesco Transducer Products, Inc. Their acquisition system consists of a central acquisition unit with eight signal conditioning units both from IO Tech Group Ltd. They measure displacements with a sampling frequency of 1 kHz and record data continuously. On the other hand, the AE sensors are Endevco® Isotron® wide frequency bandwidth accelerometer,

Model 42A18. Their acquisition system is the WaveBook/516E from IO Tech Group Ltd. They measure accelerations with a sampling frequency of 10 kHz and record a 2100 ms long sample every time the acceleration exceeds 10 mg (time t0 of the sample). The sample starts 100 ms before t0 and ends 2000 ms after that.

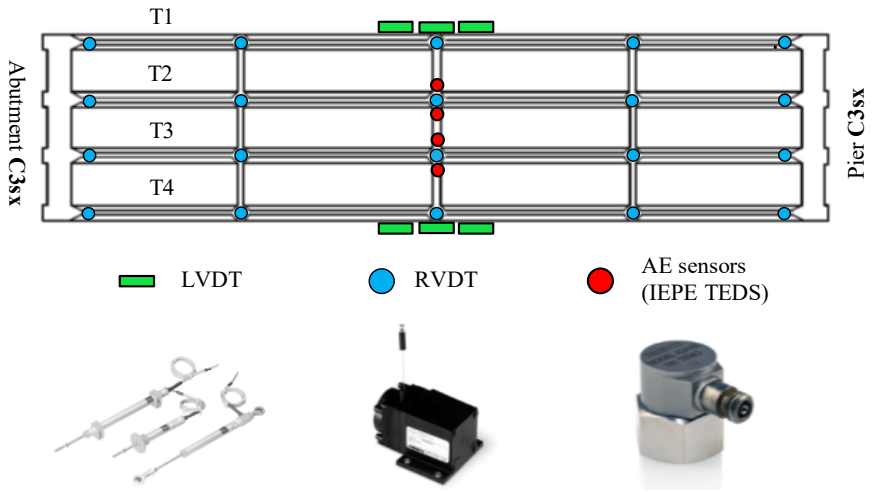

Figure 5.7 Monitoring system layout (only sensors relevant in our analysis).

Type	Full-Scale (FS)/Range	Accuracy	Sampling Frequency	Number
RVDT (deflection)	50–100 mm	1.5‰ FS	1 Hz	20
RVDT (deflection)	500 mm	5‰ FS	1 Hz	12
LVDT (crack-opening)	10 mm	1‰ FS	1 Hz	22
AE sensors	50 Hz–10 kHz	500 mV/g	10 kHz	4

Table 5.1 Technical features of sensors installed on the viaduct (only sensors relevant in our analysis).

5.3.3 Load-Test Protocol

The load-test protocol consists of five loading and unloading phases with a progressive number of steel ballast weights with a size of 2.35 × 1.84 × 0.45 m and a weight of 100 kN each. They are placed in the middle of the span C3sx in layers of 12 ballast each. The load unit is 2400 kN: two layers of ballast, which produces a bending moment in the girders' middle cross-section of 4200 kNm, corresponding to the load effect resulting from the design traffic load [109].

Figure 5.8 illustrates the five loading phases, identified with codes P1 (1200 kN), P2 (2400 kN), P3 (4800 kN), P4 (7200 kN), and P5 (bridge's ultimate capacity). Figure 5.9 shows a picture of the bridge in phase 5, loaded with 93 ballast—9300 kN. Details about the load-test protocol are in [154] (in Italian).

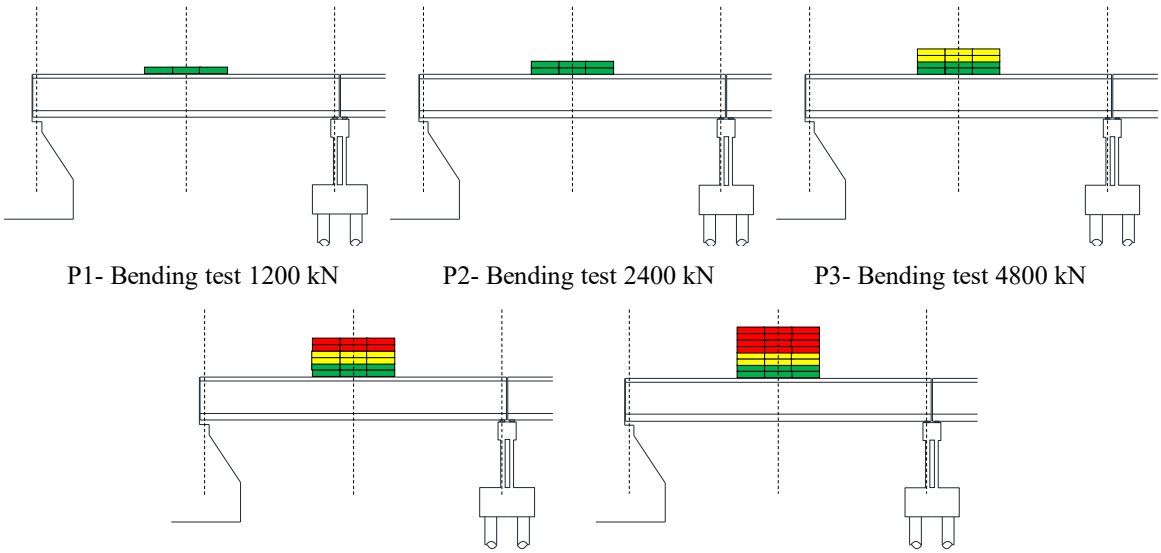

Figure 5.8 Load-test protocol: five loading phases with an increasing number of ballast weights.

Figure 5.9 The Alveo Vecchio viaduct during the loading phase 5, loaded with 93 weights—9300 kN.

5.4 Results of the Case Study

In this Section, we report the most important results about the bridge deflection and the crack opening at the bottom of the prestressed girders. Data come from the sensors installed on the external girder T1, which experienced the greatest deflection and deformation. Figure 5.6 represents the locations of girders, displacement sensors (RVDT), and crack-opening sensors (LVDT).

Then, we report some significant results from the two AE sensors, T2AE1 and T2EA2, installed on the girder T2 during the loading phases P3 and P4. No AE sensors have been installed on the girder T1, and no relevant results came from the last phase P5 due to the damage of such sensors during that phase. The location of AE sensors is also represented in Figure 5.6. We analyze raw-data samples with the software MATLAB®. We did not use any

other commercial software. The parameters investigated include amplitude, signal strength, and peak frequency. Table 5.2 shows the values of the threshold, the sampling frequency, the high-pass filter, and the three time-parameters PDT, HDT, and HLT, which we calibrated to recognize correctly at least 95% of the hits from a sample of 500 AE randomly extracted from those recorded in the loading phases P3 and P4.

After recording the acoustic signals identified in steps P1, P2, and P3, we set the threshold value at 60 dB to filter out noise and minimize false positives. This threshold allowed us to effectively discriminate relevant acoustic signals. This threshold value is consistent with other studies in the literature [51], [149].

During the four days of load test, the temperature was between 18 °C and 34 °C; the relative humidity was in the range 56–60%.

Amplitude Threshold	Sampling Frequency	High-Pass Filter Frequency	Peak Definition Time (PDT)	Hit Definition Time (HDT)	Hit Lockout Time (HLT)
1 mV; 60 dB	10 kHz	500 Hz	20 ms	10 ms	10 ms

Table 5.2 Threshold, sampling frequency, high-pass filter, and time-parameters PDT, HDT, and HLT.

5.4.1 Results from Displacement and Crack-Opening Transducers

Figure 5.10a shows the vertical displacements of the girder T1 recorded by RVDT sensors during the different phases of the load test, while Figure 5.10b shows the load-deflection curve of the girder T1 midspan, along with its envelope representing its trilinear idealized flexural response. It is easy to recognize stage I—elastic, stage II—cracks initiation and propagation, and stage III—after the yielding of post-tensioned cables. According to this trilateral load-deflection model of the girder T1, the first-crack load is 3700 kN, while the ultimate capacity is 8700 kN.

Regarding the cracks opening, Figure 5.11 shows the longitudinal strain recorded by LVDT sensors at the bottom of the middle cross-section of girder T1: Figure 10a is about the loading phase P3—4800 kN, while Figure 10b is about the loading phase P4—7200 kN. In Figure 5.10a, a change from stage I—elastic—and state II—cracked is visible, corresponding to a load of 3300 kN. In contrast, Figure 5.10b shows a softer change in the behavior, confirming the cracked condition of the girder from the beginning of P4. The colors green, yellow, and red in the background of graphs represent the layers of steel ballast weights loaded on the

viaduct: two green layers for 2400 kN, two additional yellow layers for 4800 kN, and two additional red layers for 7200 kN (see Figure 5.8 for the load-test protocol).

Figure 5.12 is a picture of the visible cracks (on girder T1) opened during the loading phase P3. Figure 5.13 is a picture of the visible cracks (on girder T1) opened during the loading phase P4.

Additional results from the monitoring system, like girders' deflections, strain measurements, rotations of pier and abutment, and temperatures, are in the load test report [155] (in Italian).

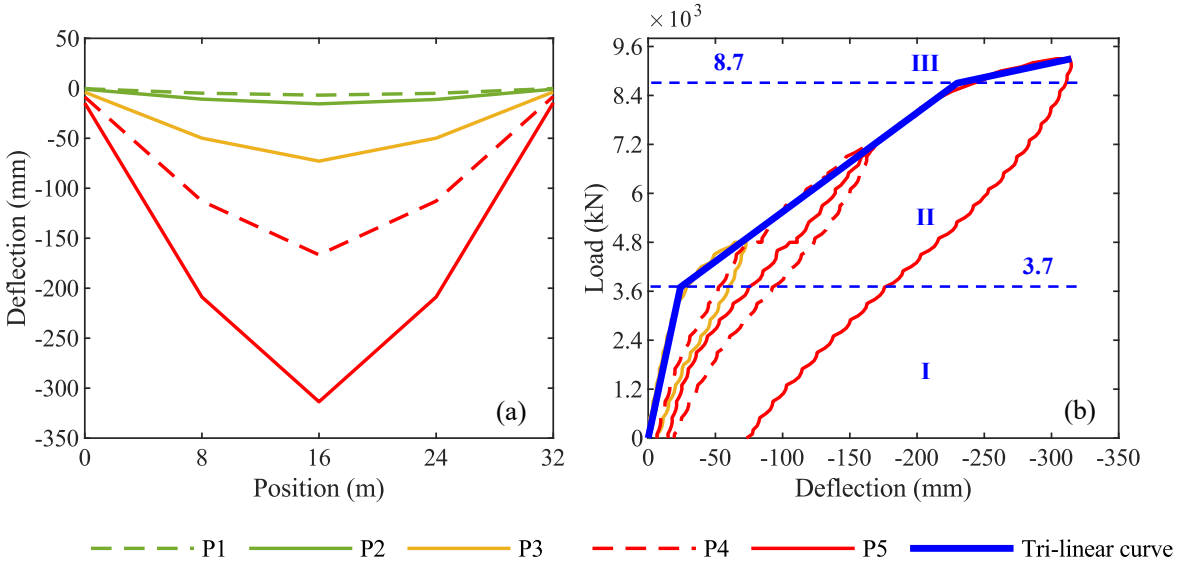

Figure 5.10 (a) Vertical displacements along girder T1 in the five loading phases; (b) load-deflection curve of girder T1 and its trilinear idealized flexural response.

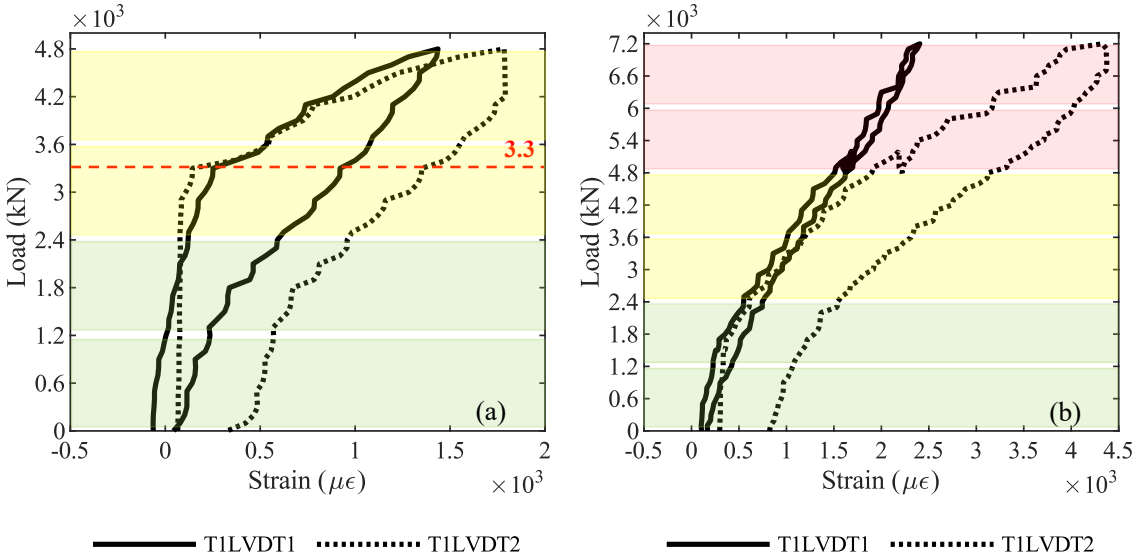

Figure 5.11 Longitudinal strain at the bottom of the middle cross section of girder T1: (a) loading phase P3; (b) loading phase P4. The red dashed line represents the first-crack load identified by crack-opening sensors.

Figure 5.12 Visible cracks on girder T1 opened during the loading phase P3 4800 kN.

Figure 5.13 Visible cracks on girder T1 opened during the loading phase P4 7200 kN.

5.4.2 Results from AE Sensors – P3 4800 kN

In this subsection, we report the results of the analysis performed on the AE acquired during the loading phase P3 4800 kN. In Figure 5.14, we report four graphs with the load from 0 to 4800 kN on the horizontal axis and the amplitude (Figure 5.14a), the cumulative number of hits (Figure 5.14b), the signal strength—MARSE (Figure 5.14c), and the cumulative MARSE (Figure 5.14d) on the vertical axis. In all of them, the red dashed line represents the first-crack load: 3300 KN; it has been identified by the crack-opening sensors and represented also in Figure 10a. The colors green, yellow, and red in the background of graphs represent the layers of loads on the viaduct, as explained in Section 5.4.1.

To discriminate different types of damage, such as concrete cracks and failure of steel wires, we analyzed the AE in the frequency domain. We aimed to investigate the presence of clusters in amplitude—peak-frequency graphs and load—peak-frequency graphs. Such clusters may represent different sources of the elastic waves [147]. Figure 5.15a shows these graphs for both the sensors installed on the girder T2. Two clusters are clearly visible in data from sensor T2AE1, while data are more scattered from sensor T2AE2. We reported the distributions of peak-frequencies from AE recorded by both sensors in a histogram represented by Figure 5.15b.

Finally, we compared the results from the AE acquired on the girder T2 with the results from the crack-opening sensors LVDT installed on the girder T1. Figure 5.16a shows the hit

amplitudes recorded during the loading phase P3, Figure 5.15b shows the cumulative MARSE, and Figure 5.16c shows the strain at the bottom of the girder T1. The blue dashed line at 4300 kN represents the value of the load when we recorded the AE generated by the opening of the first crack in the girder T2; after that, AE increase considerably. In contrast, the red dashed line represents the first-crack load (3300 kN) identified by LVDT, as already explained in Subsection 5.4.1.

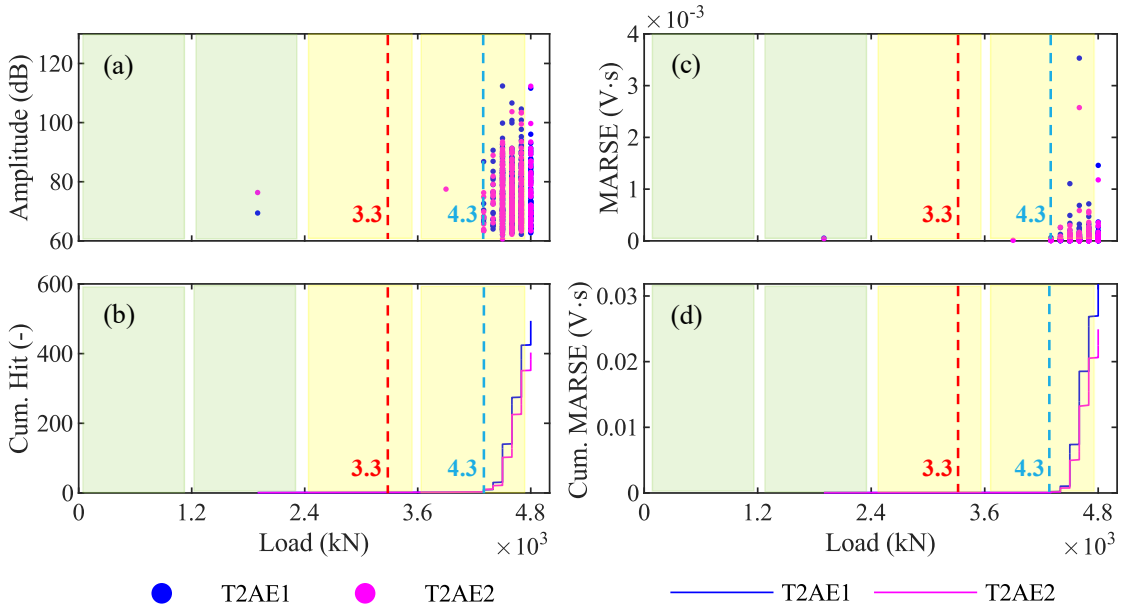

Figure 5.14 Results in the time-domain from the loading phase P3 4800 kN: (a) amplitude; (b) cumulative number of hits; (c) signal strength; and (d) cumulative signal strength.

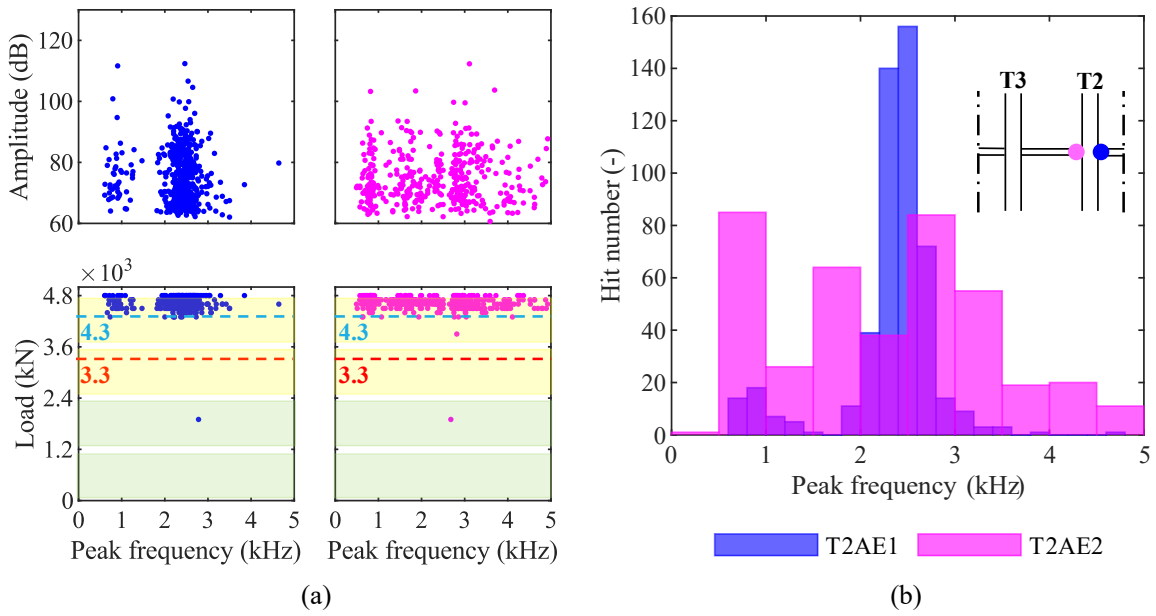

Figure 5.15 Results in the frequency-domain from the loading phase P3 4800 kN: (a) amplitude and load—peak-frequency; (b) peak frequency distribution among hits.

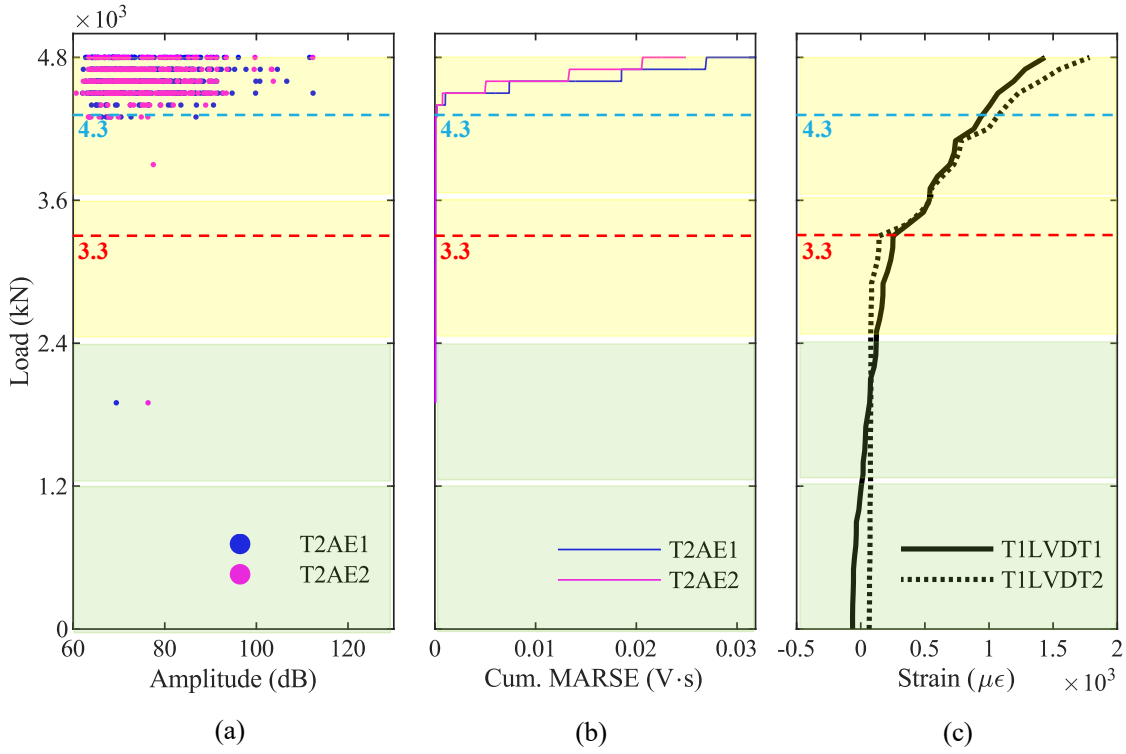

Figure 5.16 . Results from AE and crack-opening sensors during phase P3: (a) amplitude from girder T2; (b) cumulative signal strength from girder T2; (c) longitudinal strain at the bottom of girder T1.

5.4.3 Results from AE Sensors – P4 7200 kN

The same graphs as those shown by Figures 5.14–5.16 for the loading phase P3 are here reported for the loading phase P4 in Figures 5.17–5.19.

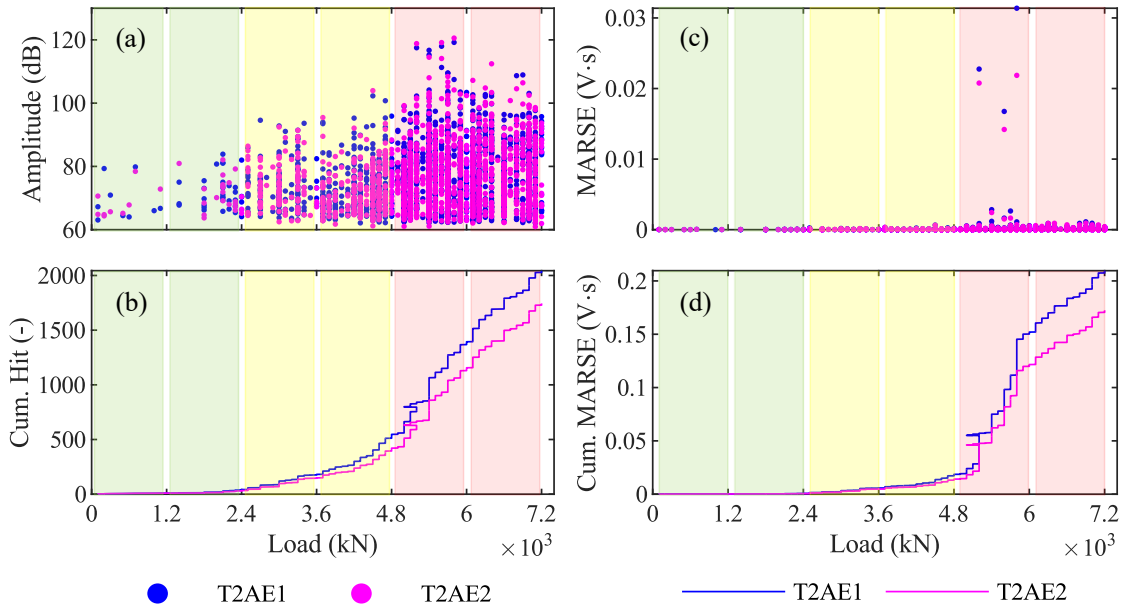

Figure 5.17 Results in the time-domain from the loading phase P4 7200 kN: (a) amplitude; (b) cumulative number of hits; (c) signal strength; and (d) cumulative signal strength.

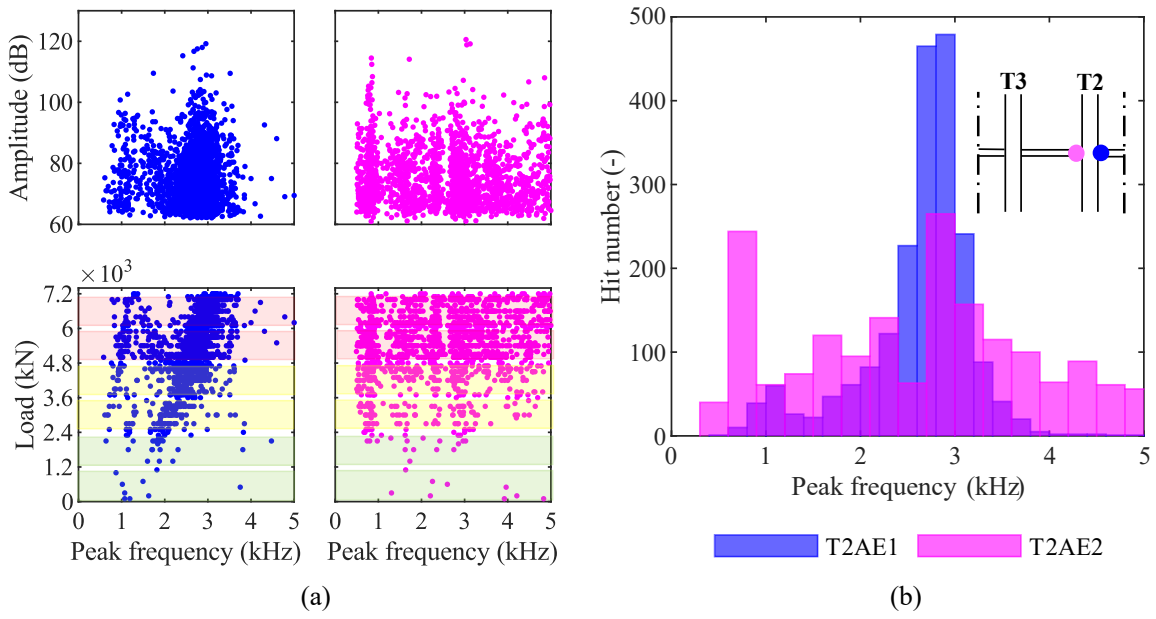

Figure 5.18 Results in the frequency-domain from the loading phase P4 7200 kN: (a) amplitude and load—peak-frequency; (b) peak frequency distribution among hits.

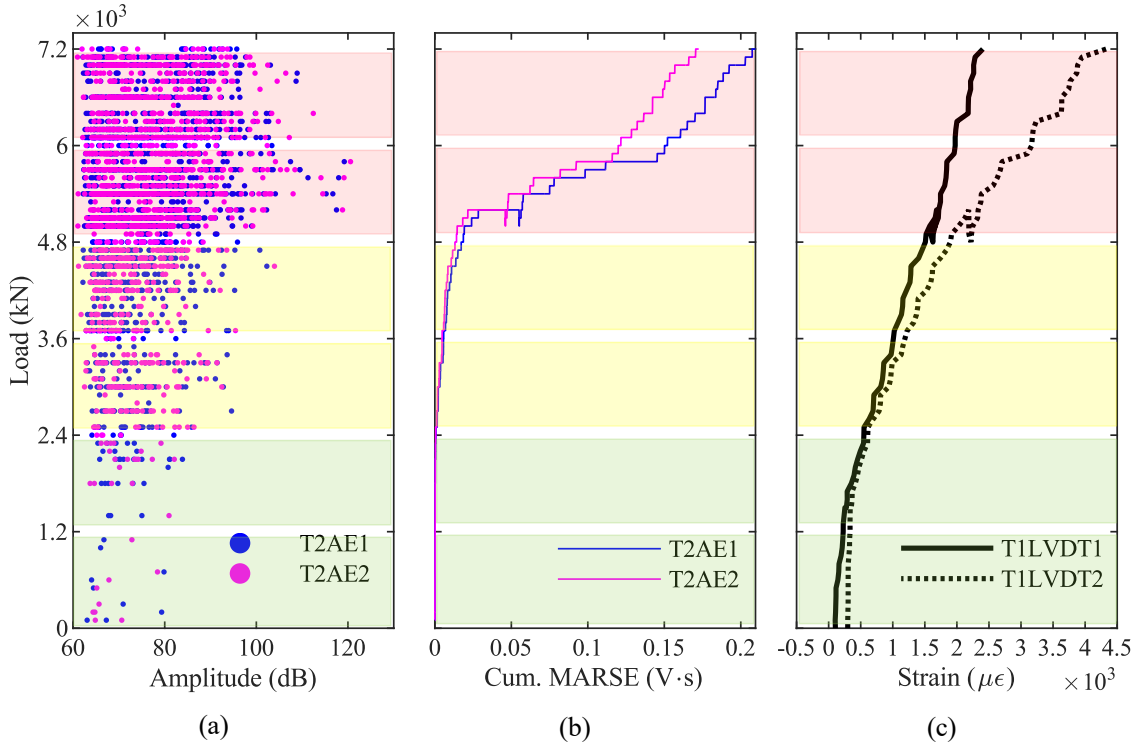

Figure 5.19 Results from AE and LVDT sensors during phase P4: (a) amplitude from girder T2; (b) cumulative signal strength from girder T2; (c) longitudinal strain at the bottom of girder T1.

5.5 Discussion of Results

We discuss the results of the AE analysis reported in the previous section. Here, we start with the loading phase P3; then, we move on to the phase P4; finally, we present a comparison between results from phases P3 and P4 to identify what AE can effectively suggest in terms

of pre-existent cracks or other damages, maximum load withstood, opening of the first crack, and damage recognition.

5.5.1 Discuss of AE Results from P3 – 4800 kN

Based on the AE results of the loading phase P3, we can identify the opening of the first crack on the girder T2. Indeed, the absence of cracks for low values of the load suggests that the girder T2 was not cracked before the beginning of P3 [153]. We can recognize the opening of the first crack in the graph of the amplitude plotted against the load (Figures 5.14a and 5.16a) as the first AE after which the number of AE increases significantly. We can identify it also in the graph of the cumulative MARSE plotted against the load (Figures 5.14d and 5.16b) as the point in which the curve has a sharp change of slope. In particular, the first crack opens for a load of 4300 kN, represented by blue dashed lines in those graphs. Figure 5.14a also shows some AE for loads lower than 4300 kN. However, they are characterized by low values of the MARSE (Figure 5.14c), which do not change the slope in the cumulative MARSE (Figure 13d); therefore, they are probably related to bearing deformations or thermal effects [47], [156]. On the other hand, the crack-opening sensors (LVDT) at the bottom of the girder T1 suggest that the first crack opens for a load of 3300 kN (Figure 5.16c). The difference between these two values is mainly due to the difference in the girders monitored by the two technologies: girder T1 by LVDTs, and girder T2 by AE sensors. Indeed, during the load test, the girder T1 experienced the greatest deflection and deformation; therefore, it is reasonable to assume that cracks have opened first on the girder T1 and then on the girder T2. As a result, we can conclude that the AE technique can effectively identify the opening of the first crack. However, additional studies and load tests are necessary to directly compare the observation from AE sensors and crack-opening sensors installed on the same girder.

As far as the analysis in the frequency domain is concerned, Figure 5.15 shows two clusters in data from the sensor T2AE1 (blue dots): around 1 kHz and 2.5 kHz. They may represent different sources of the elastic waves, such as different types of damage; for instance, some authors have recognized that tensile-cracks have a higher average frequency than shear-cracks' [157], [158]. On the other hand, data from the sensor T2EA2 (magenta dots) are more scattered. The reason for this difference is not clear since the two sensors were placed on opposite sides of the same girder's middle cross-section. The outcomes of our experiment are not enough to univocally establish which types of damage correspond to those clusters. That would require multiple load tests on bridges monitored by AE sensors carried on until different loads followed by autopsies of the monitored girders; that would allow correlating

the damages occurred with the AE acquired in each test. In conclusion, AE can recognize clusters of acoustic events, which are probably related to different types of damage. However, further experiments are needed to establish and validate a robust identification procedure.

5.5.2 Discuss of AE Results from P5 – 7200 kN

Results from AE acquired during the loading phase P4 confirm that the AE technique can effectively discriminate whether a prestressed concrete structure is affected by pre-existent cracks and identify the maximum load withstood by the structure. Indeed, the amplitude—load graph of data recorded during P4 (Figures 5.17a and 5.17a) shows several AE for low values of the load. These AE are generated by the friction between the two surfaces of a crack [159]: this confirms the presence of pre-existent cracks in the girder T2 before the beginning of P4. On the other hand, the cumulative-MARSE—load graph (Figures 5.17d and 5.19b) shows a change in the curve slope around 4800 kN: this confirms that the maximum load withstood by this viaduct is 4800 kN (at the end of P3) and that the damage propagation starts only after that the maximum load withstood has been exceeded. This last consideration is in line with the Kaiser and Felicity effects, which we will focus on in Subsection 5.5.3. The LVDTs installed on the girder T1 (Figure 5.19c) confirm that such girder experiences a non-elastic behavior starting from the beginning of the loading phase P4, exceeding a strain of 0.8 με for a load of 3300 kN, while the strain was around 0.2 με for 3300 kN during P3. Since AE allow to recognize the maximum load withstood by a bridge, their application is particularly effective in statically indeterminate structures designed to achieve robustness [160], where the ultimate capacity is preceded by a progressive state of damage.

As far as the classification of different types of damage based on the AE technique is concerned, in the MARSE—load graph (Figure 5.17c), we can recognize three events between 5200 kN and 5800 kN with a signal strength around ten times higher than the others. They may have been generated by different sources than concrete cracks, such as post-tensioned steel wires failure. Again, a campaign of load tests on girders monitored by AE sensors followed by their autopsy would help in the correlation between the AE results and the types of damage that occurred during the load tests. Such a campaign would offer useful insights also into the difference between results from sensors T2AE1 and T2AE2 in the frequency domain (Figure 5.18): data from the first sensor point out two clusters around 1 kHz and 2.8 kHz, while data from the second sensor provide more scattered peak-frequencies.

5.5.3 Comparison of Results from P3 and P4 for Low Values of the Load (0–2400 kN)

Permanent AE monitoring is supposed to provide information also on the condition state of in-service structures, which typically do not experience a load exceeding the load of the design test. Therefore, AE monitoring is effective only if it allows us to understand whether that structure has pre-existent cracks only based on data acquired during low values of the load. In our case study, the maximum weight allowed to transit on the viaduct produces a bending moment equal to the one produced by the unit load 2400 kN. Therefore, AE monitoring is effective only if it can identify a difference in the viaduct behavior in the cases without and with pre-existent cracks only based on data acquired between 0 kN and 2400 kN. Consequently, the comparison between the results from the loading phase P3 and P4 in the range of load 0–2400 kN is particularly interesting. Indeed, the results from the phase P3 are those from a structure without pre-existent cracks, whose response is elastic until the first crack occurs at around 3300 kN; in contrast, results from the phase P4 are those from a structure with pre-existent cracks.

Figure 5.120a,b show the amplitude–load graphs of AE acquired during loading phases P3 and P4, respectively. Their difference is visible even for low values of the load: the girder with pre-existent cracks (T2 during P4) emits a higher number of AE than the one without cracks (T2 during P3). The cumulative number of hits–load graph (Figure 20c) and the cumulative MARSE–load graph (Figure 19d) show this difference even more clearly: solid lines (T2 during P3) are almost linear, while dotted lines (T2 during P4) have a sharp change in the slope between 1200 kN and 2400 kN.

The difference between P3 and P4 in terms of the cumulative number of hits is consistent with the Kaiser and the Felicity effects, which are visible in Figure 5.21. Note that Figure 5.21 is the union of the cumulative number of hits during P3 (Figure 13b), during P4 (Figure 16b), and during the unloading phase between P3 and P4. During the loading phases P3, it is possible to observe the Kaiser effect [153] since any permanent damages have never occurred within the girder before P3: as the load increases from 0 kN to 4800 kN, no AE are generated until the exceedance of the first-crack load. In contrast, during the loading phase P4, it is possible to observe the Felicity effect [153] since some permanent damages have occurred in the previous phase: as the load increases from 0 kN to 7200 kN, some AE are generated starting from 1200 kN, before the previous maximum load (4800 kN) is exceeded. This difference in the AE recorded during phases P3 and P4 for low values of the load points out a difference in the structural behavior and can discriminate the presence of pre-existent cracks.

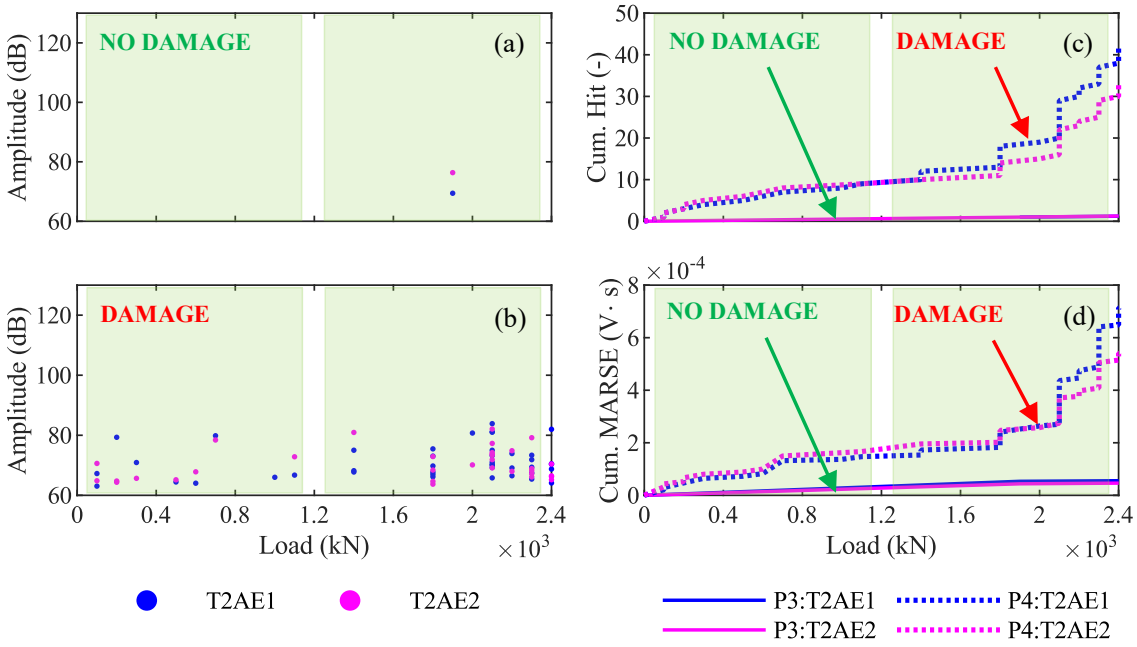

Figure 5.20 Differences in amplitude (a,b) and cumulative signal strength (c,d) between the AE acquired from the viaduct without pre-existent cracks (phase P3) and with pre-existent cracks (phase P4) for loads between 0 kN and 2400 kN.

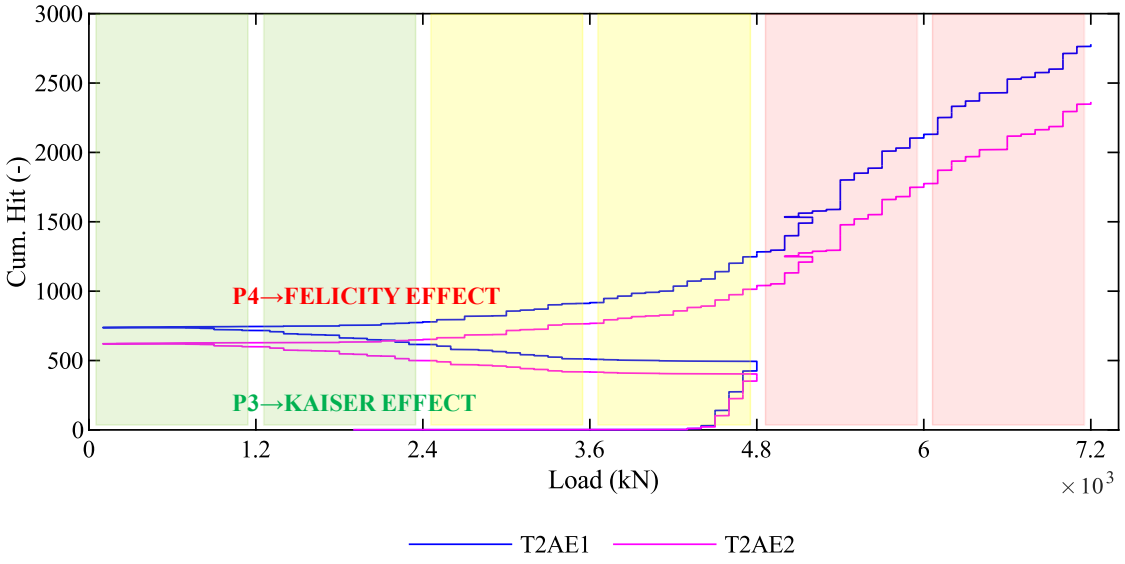

Figure 5.21 Kaiser and Felicity effects in the AE acquired during the loading phases P3 and P4.

5.6 Conclusions

In this contribution, we presented an application of the AE technique to a real-life case study, the Alveo Vecchio viaduct, a prestressed-concrete highway-viaduct that underwent a sequence of loading and unloading cycles with progressively increasing loads up to three times the design load. Each test phase was monitored by an extensive monitoring system, which included a network of AE sensors. The most significant results have been observed

during test phases P3 (maximum load of 4800 kN, corresponding to two times the design load) and P4 (maximum load of 7200 kN, corresponding to three times the design load).

We analyzed the AE signals recorded during the load test and extracted the following parameters: amplitude, signal strength (MARSE), and peak frequency. We examined how far these signal features can detect, quantify, and classify damage on the bridge. The main outcomes of this research are:

(i) AE allow easy recognition of whether a prestressed concrete bridge is cracked or not: a bridge with pre-existent cracks produces several AE under service load, whereas virtually no hit is recorded on a bridge with no cracks. The different behavior is evident by plotting the amplitude, the cumulative number of hits, or the cumulative MARSE against the load (compare Figures 5.16a,b, and 5.20a with Figures 5.19a,b, and 5.20b, and note the difference between the curves with label DAMAGE and NO DAMAGE in Figure 5.20c,d).

(ii) AE also allow clear identification of the opening of the first crack, as this is typically accompanied by the first-time emission of a high-intensity signal, followed by several more as the cracks propagate. The opening of the first crack is easily detected by plotting the amplitude or the cumulative number of hits against the load (see Figure 5.14a,b). The first-crack also corresponds to the first of a series of AE with a high MARSE in the MARSE graph and to a sharp change in the slope in the cumulative MARSE graph (see Figure 5.14c,d).

(iii) The AE technique also allows us to identify the maximum load withstood by the bridge: it corresponds to a sharp change in the slope of the cumulative MARSE graph, as shown in Figure 5.19b.

(iv) In principle, it is possible to classify the damage by type by analyzing the AE in the frequency domain. In our experiment, the AE occur grouped in well-separated clusters in the amplitude–peak frequency graph, suggesting that each cluster corresponds to a different source of AE, and therefore to a different damage episode. While it is possible, in principle, with further experiments, to define a general correlation between clusters and types of damage (cracking, deboning, failure of steel wires, etc.), the outcomes of our experiment are not enough to univocally establish such a correlation.

In summary, the outcomes of this experiment suggest that AE can be used successfully in permanent monitoring of prestressed concrete bridges to provide information on the cracking state and maximum load withstand. They can also be used as a non-destructive technique in short-term monitoring to discriminate whether a structural member has pre-existent cracks or

not. Apparently, AE also allow the classification of different types of damage, although further experiments are needed to establish and validate a robust identification procedure.

6 METROLOGICAL VALIDATION OF NON-DESTRUCTIVE TESTING METHODS FOR ASSESSING THE CONDITION STATE OF POST-TENSIONED PRESTRESSING SYSTEMS

Abstract. The evaluation of the condition of the prestressing system plays a crucial role in the reliability assessment and maintenance planning of post-tensioned (PT) concrete bridge decks. This evaluation should not rely uniquely on visual inspections, due to the many limitations inherent to them. Several non-destructive testing (NDT) techniques have been developed over the years for investigating the state of the prestressing system, yet their effectiveness in detecting defects remains largely unknown. This study aims to address this knowledge gap by performing a comprehensive metrological validation of three NDTs for PT concrete bridges, namely Digital Radiography (DR), Ground Penetration Radar (GPR), and Reflectometric Impulse Measurement Test (RIMT). The validation study is carried out by quantifying the correlation between the NDT outcomes and the level of defects observed during the autopsy of the prestressing system of a decommissioned bridge in Italy, the Alveo Vecchio viaduct. The correlation analysis utilizes contingency tables, conditional probability tables, and various correlation coefficients to determine the relationship between the NDT results and the actual defects in the prestressing system. The findings indicate the superior performance of the DR method in detecting grouting void and grout fracturing, compared to the GPR and RIMT methods. Notably, none of the methods effectively identified steel cable corrosion. The results provide valuable guidance for assessing prestressing system components and inform future inspection and maintenance strategies.

6.1 Introduction

The ageing of post-tensioned (PT) concrete bridges has become a concern for infrastructure managers and control authorities due to the increasing number of structures that have surpassed their expected lifespan. These bridges may exhibit various issues such as concrete carbonization, concrete cracks, steel corrosion, local damage, loss of prestress, and abnormal deflection at the midspan [6]. Monitoring and maintaining these structures are crucial to ensure their safety and prevent potential hazards. Accurate knowledge of the bridges' degradation, particularly regarding the most fragile and critical components, is essential. The scientific literature on risk assessment and bridge maintenance emphasizes the significant role of the prestressing system's condition state in maintaining the integrity and stability of prestressed concrete (PC) bridges under load [10]. Therefore, precise monitoring and

assessment of the condition state of prestressing systems are necessary to ensure the safety and longevity of PC bridges. For instance, the Italian Guidelines for Risk Classification, Safety Assessment, and Monitoring of Existing Bridges [11] classify PT structures as particularly critical, as conventional investigation techniques and visual inspections may not provide sufficient insight into their actual condition state. These guidelines recommend employing different Non-Destructive Test (NDT) methods and combining their results to improve the knowledge of these structures' condition state and prioritize maintenance actions.

Currently, several NDT methods are commonly used to evaluate the condition state of prestressing systems. A study conducted on behalf of Highway England [1], reports the most common NDTs adopted to investigate this structural type, specifying their strengths, weaknesses, primary use, and in some cases, indicates potential use with further development of the technology. The document discusses technologies such as Ground Penetration Radar (GPR), mainly used for identifying the prestressing cable path and potentially useful for identifying the grouting void within nonmetal ducts; Impact Echo (IE), which instead promises to identify the grouting void within metal ducts contained in prestressed concrete girders; Digital Radiography (DR), which can highlight defects in both the grout and tendons to a high degree of accuracy; Ultrasonic Tomography (UT), used to detect corrosion of tendons, bond quality and grouting voids within ducts. Moreover, according to the Research report of S. Hurlebaus, et al., 2017 [28], suggests the desirability of combining multiple NDTs to improve their capabilities.

In this paper we focus on three of these NDTs: Digital Radiography (DR), Ground Penetration Radar (GPR), and Reflectometric Impulse Measurement Test (RIMT) have emerged as very promising ones and they are increasingly applied and recommended in guidelines for non-destructive assessment of PT bridges. DR allows the inspection of internal material structures using X-rays. It works by emitting controlled X-rays through the material, which are then detected by a digital detector on the other side. X-rays are absorbed exponentially by materials based on their thickness and density, resulting in a black and white image similar to medical X-rays. DR is claimed to effectively detect grouting void in metal ducts, cable breaks, and defects in concrete in PT structures [78] [161] [77]. GPR, on the other hand, relies on the reflections of short pulses of electromagnetic energy transmitted and received by an antenna when they encounter interfaces between materials with different dielectric properties [161]. Currently, GPR is mainly used for locating cables and ordinary reinforcement in PT structures [79]. Lastly, RIMT relies on the generation of high-frequency

electromagnetic pulses along the wires of a PT cable, and on the analysis of the signal that is reflected by corrosion pits, wire breaks, and grouting void within the ducts [80]. This technique is not widely recognized as an effective NDT method for assessing the condition state of prestressing systems. For example, a fib Bulletin published in 2001 [68] discouraged its use as a diagnostic technique for grouted tendons.

The outcomes of NDT methods allow infrastructure managers and control authorities to detect defects in prestressing systems and address potential issues before they develop into significant structural problems. However, some critical question remains still unanswered: how reliable are these NDT methods? Do we gain a better understanding of the prestressing system's condition state when we have the results of one or more NDTs available? Some studies in the literature have attempted to answer these questions by comparing the outcomes of NDT methods regarding the prestressing system's condition state with the results obtained from an autopsy of the analysed structural components [162]. Nevertheless, a comprehensive and rigorous evaluation of the effectiveness of the most used NDT methods in PT bridges is still lacking.

In this paper, a metrological validation of the DR, GPR, and RIMT techniques for the identification of defects in the prestressing system of concrete bridge girders is carried out. Specifically, the study examines the effectiveness of DR in assessing the grout quality i.e., the presence of grouting voids and fracturing; the capability of GPR to detect defects in the prestressing system besides locating their positions along the girders; and finally, the actual performance of RIMT in recognising presence of grouting void and the corrosion of steel cables.

The study exploits the results of an extensive experimental campaign carried out on Alveo Vecchio viaduct. Constructed in 1968 and decommissioned in 2005 after being affected by a landslide, this PT bridge is representative, in terms of type, age, and deterioration state, of over 50% of the bridges currently in operation in the Italian highway network. In 2019, the viaduct was transformed into a full-scale open-air laboratory, enabling various NDTs, semi-destructive tests (SDTs), proof load tests, and dynamic tests to be conducted [9].

The validation study is carried out by quantifying the correlation between the outcomes of NDT of few girders of Alveo Vecchio viaduct, with the level of defects observed during the autopsy of the prestressing system. In particular, the following procedure has been adopted: (i) conducting NDTs on four girders of the full-scale decommissioned PT viaduct and

recording their outcomes; (ii) performing a dissection of these girders by demolishing them, extracting the prestressing system, opening the metallic ducts, and recording the observed defects in the grout and steel wires along the cables; (iii) comparing the NDT outcomes with the observed defects along the cables and quantifying the effectiveness of these NDT methods through correlation analyses. For this purpose, contingency tables [163] are developed, with the degree of correlation measured using the Spearman's correlation coefficient [164]. In order to mitigate any potential bias introduced by the choice of the correlation metric, comparison are made also with other correlation measures, namely the Pearson correlation coefficient [165], the Polychoric correlation coefficient [166], [167], the Goodman-Kruskal Gamma [168], and the Stuart-Kendall Tau-c [169], [170]. The analysis results provide valuable insights into the performance of the investigated NDT methods for assessing the health of the PT system and are compared to the findings of previous research on the topic.

The rest of the paper is organised as follows: section 6.2 introduces the open-air laboratory at Alveo Vecchio viaduct; Section 6.3 provides a detailed description of the metrological validation method; Section 6.4 describes statistical tools used to perform the correlation analysis; Section 6.5 presents the outcomes of the NDTs and the dissection of the girders; Section 6.6 reports the results of the correlation analysis and discusses them; Section 6.7 reports a discussion of the results obtained. Finally, conclusions are drawn in section 6.8.

6.2 Case Study – The Alveo Vecchio viaduct

In Chapter 3, we comprehensively examine the case study, the Alveo Vecchio viaduct. To enhance clarity, we present the viaduct's top view, lateral view, and cross-section in Figure 6.1. Additionally, Figure 6.2 showcases a transversal section of the girders with the prestressing cables, offering detailed insights into the structural configuration of the viaduct.

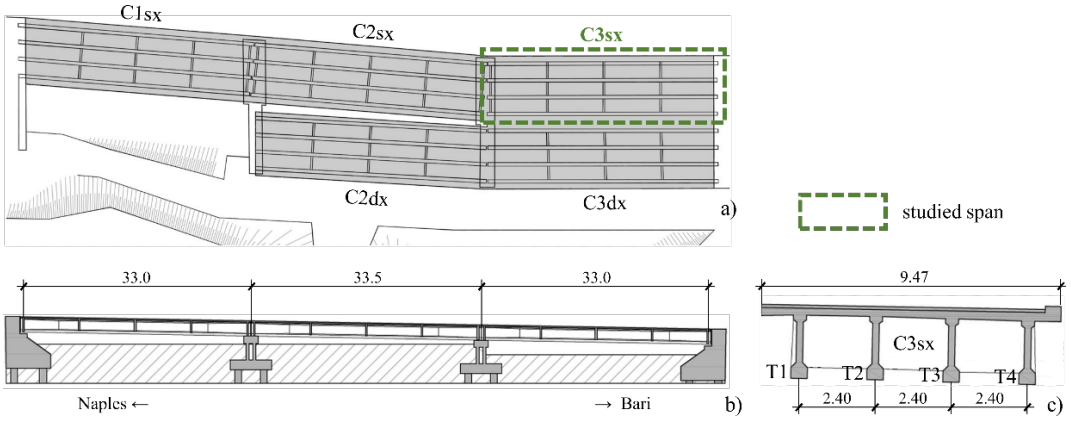

Figure 6.1 (a) top view; (b) lateral view; and (c) cross-section of the Alveo Vecchio viaduct (Italy)

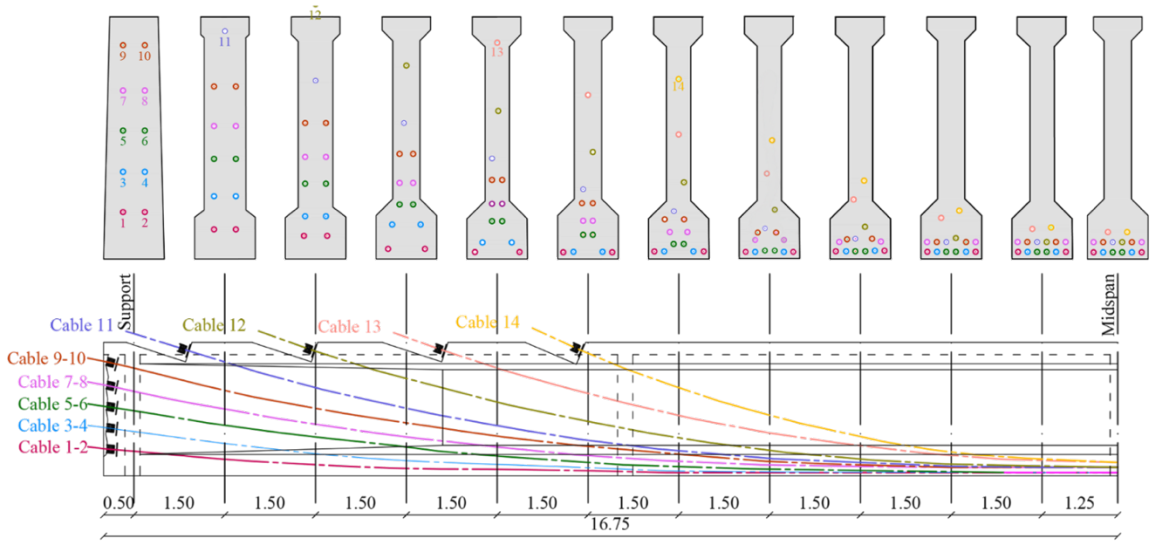

Figure 6.2 Longitudinal and transversal section of girders with post-tensioned cables

6.3 Experimental campaign

This section briefly illustrates the methodology employed for the metrological validation of three NDT methods, namely Digital Radiography (DR), Ground Penetration Radar (GPR), and Reflectometric Impulse Measurements Test (RIMT). The methodology aims to determine whether the condition state of the PT system of Alveo Vecchio viaduct identify by these NDT methods corresponds to the actual condition state, which is observed through a dissection of the tested girders. The methodology encompasses the following steps:

1. *Application of NDT Methods:* DR, GPR, and RIMT are employed to detect defects in the prestressing system of the girders.
2. *Autopsy Procedure:* after the NDT methods are performed, a dissection is conducted on the four tested girders. This involves the extraction of the cables, allowing for a direct observation of their actual condition state.
3. *Correlation Analysis:* A correlation analysis is conducted to evaluate the relationship between the outcomes of the NDT methods and the observed condition state of the prestressing system.

6.3.1 Experimentation setup

The experimentation carried out for the metrological validation of the NDT methods has involved a series of activities performed between May 2019 and September 2022 on the C3sx span of the Alveo Vecchio viaduct. The NDT activities were carried by specialized practitioners and partner university laboratories, whereas the controlled demolition was carried out by an external contractor under University of Trento's supervision. The

interpretation of DR and GPR outputs was aided by developing defect intensity scales; in contrast, the interpretation of RIMT outcomes was provided directly by the practitioner who performed the test. It is important to note that the RD and RIMT were conducted on the same span where the load test up to failure had previously been performed (details on the load test are provided in Chapter 4). In contrast, the GPR test was conducted prior to the load test up to failure.

The study focuses on investigating two types of defects:

1. Defects related to the injected grout in the metal ducts, including the grade of grout fracturing and the presence of grouting voids.
2. The presence of corrosion in steel cables.

The metrological validation of the different NDT methods follows a standardized procedure specifically developed for the purpose of this study and consisting of the following steps:

1. Discretization: each prestressing cable is divided into 10 cm-long segments referred to as "samples".
2. Location identification: locations on the girders where NDTs will be performed and correlated with the dissection outcomes are identified.
3. NDTs: the NDT methods are performed, and the outcomes are recorded. Thresholds are established to classify each type and intensity of defect based on the NDT results. Each sample is assigned a set of classes corresponding to the defect types and intensity based on the NDT outcomes. As a results, each cable is assigned a set of arrays of classes based on the NDT outcomes.
4. Autopsy: the girders are demolished, the cables are extracted, their defects are directly observed, and the outcomes of the dissection are recorded. Thresholds are established to classify the intensity of each type of defect. Each sample is assigned a set of classes corresponding to the defect types and intensity based on the dissection outcomes. As a results, each cable is assigned a set of arrays of classes based on the dissection outcomes.
5. Correlation analysis: a correlation analysis compares the classes assigned to each pair of samples provided by NDT outcomes and the dissection outcomes. Contingency tables and a specific metric are used to quantify the level of correlation to validate the NDT methods.

It is worth noting that that the classes chosen to describe the severity of defects detected by various NDTs and to identify the state conditions of the prestressing system were selected based on the principle of maximizing distinguishable classes. Each scale includes as many distinct classes as possible to ensure a reliable assessment.

6.3.2 Non-destructive tests (NDTs)

Digital Radiography (DR). DR utilizes X-rays to penetrate materials and create images of their internal structures. X-rays are attenuated by the material depending on its thickness and density. The attenuated X-rays reach a receiver panel, which converts the X-ray energy into a digital image. Defects in the inspected object, such as cavities or cracks, appear as darker spots on the DR image. More absorbent elements, like reinforcing bars or prestressing cables, appear as lighter spots [77].

In the test campaign, two types of X-ray sources were used: a low-intensity source, with a peak energy equal to 300 kV, for inspecting structural elements less than 30 cm thick (girder webs), and a high-intensity source, with a peak energy equal to 7.5 MV, for thicker elements (girder lower flanges and near the supports). The DR outcomes were captured on a receiver panel with dimensions 40x35 cm. Inspectors placed the source on one side of the inspected element and the receiver on the other side to perform the DR. Figure 6.3 shows inspectors at work with the two X-ray sources, the receiver panel, and the real-time outcome on a mobile screen. DR inspections were primarily focused on girder T1 and a few 60 cm-wide portions of the other girders' webs (Figure 6.4).

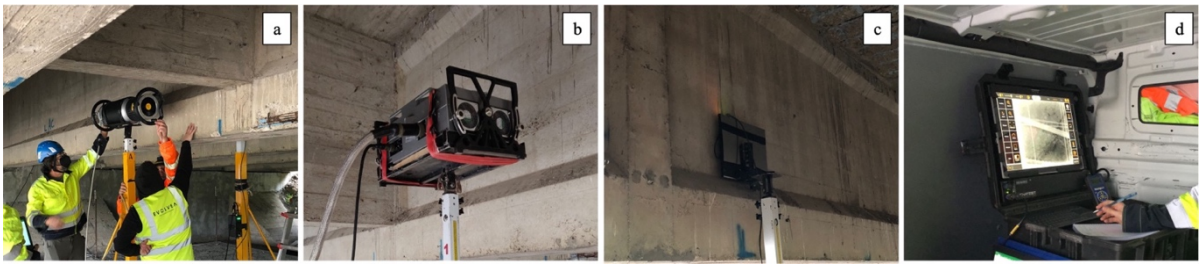

Figure 6.3 a) Inspectors at work with the X-ray low-intensity source; (b) the high-intensity source; (c) the receiver panel; (d) the real-time outcome on a mobile screen.

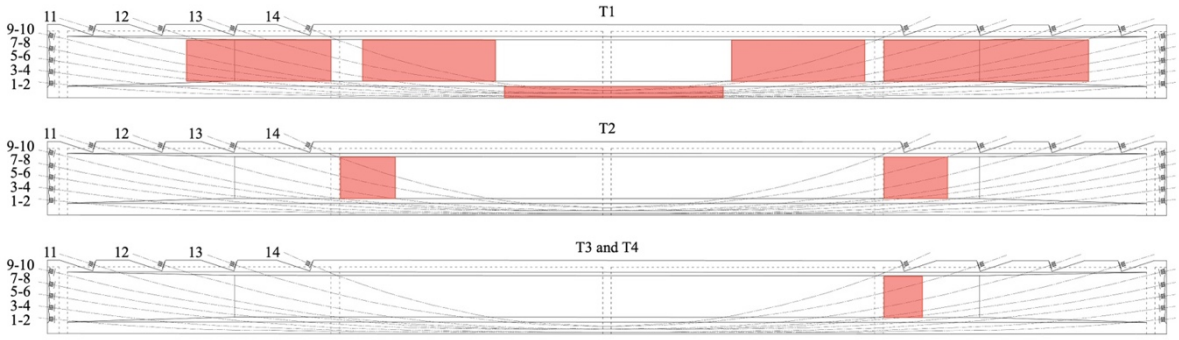

Figure 6.4 Portions of girders inspected with DR.

The defect of interest for DR is the presence of grouting voids, which was assigned the code DR.V. Figure 6.5 illustrates three the defects intensity scale used to interpret the DR outcomes. The scale shows three 10 cm long samples with the three different defect intensity levels chosen to quantify the defectiveness of each section of the cables analysed with RD. Level "0" describes a sample with no grouting void; level "1" describes a sample with some areas between the cable and metal duct or between the cable wires affected by grouting void; and level "2" describes a sample with several areas affected by grouting void, either between the cable and metal duct or between the cable wires.

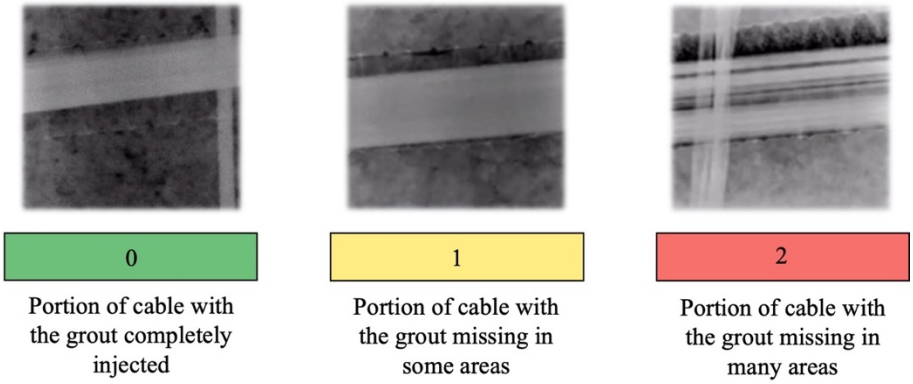

Figure 6.5 Defect intensity scale to interpret DR outcomes and identify the presence of grouting void in the prestressing cable.

The DR outputs (black & white images) were overlapped with the girders' longitudinal sections reconstructed in a CAD environment based on design documentation and accurate survey of their geometry, as shown in Figure 6.6. The intensity of the grouting void was assigned to each segment of the prestressing cables (sample) identified based on the DR outcomes.

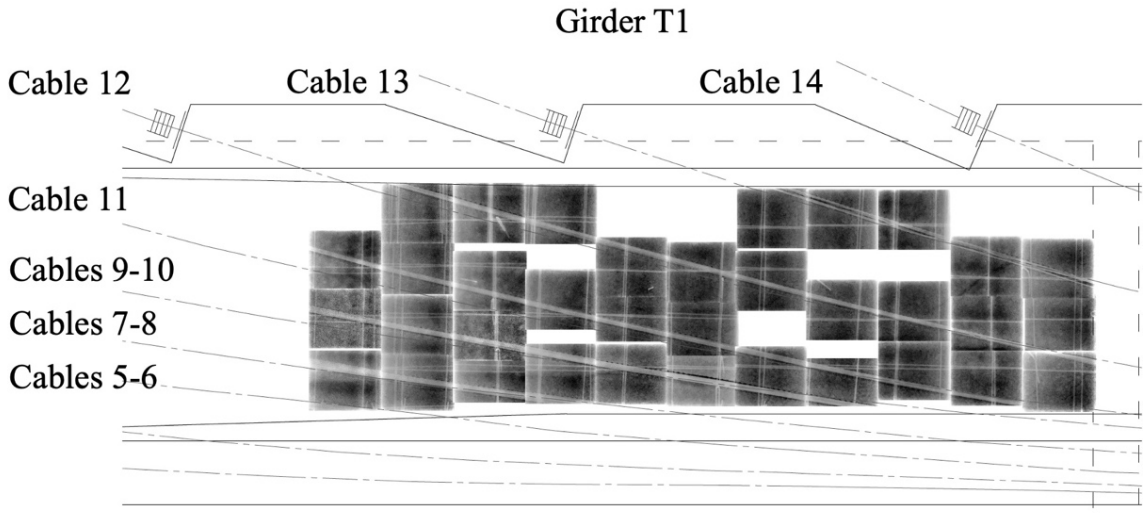

Figure 6.6 Superposition of a portion of DR outputs over the corresponding area of the longitudinal section of the girder T1.

Ground Penetration Radar (GPR). GPR works by emitting electromagnetic short pulses into the bridge structure and analysing the reflected signals. During an inspection, a GPR system with a transmitting antenna is placed on the surface of interests, and pulses are sent into the concrete deck. The reflected signals, captured by a receiving antenna, are processed to identify voids, corrosion, or variations in concrete cover thickness. GPR can also provide depth and alignment information. It is a rapid and NDT that covers a large area, but its accuracy can be influenced by signal attenuation, interference, and data interpretation. Currently, in the field of PT structures, GPR is mainly used to identify the location and diameter of steel reinforcement and prestressing cables [161].

In this study, an attempt was made to determine the corrosion rate of steel cables based on the concept that as the concentration of moisture and salts increases, the relative dielectric constant and conductivity of the concrete also increase—an increase in the dielectric constant increases, in turn, the amplitude of the reflections. The GPR equipment employed in the study included an antenna, control unit, display unit, and data recording device. A new concept of array antennas composed of 32 dipoles 3 cm apart with a frequency of 1 GHz was used to scan the faces of the girders and the underside of them.

Figure 6.7 shows the practitioners using the GPR at the Alveo Vecchio viaduct. GPR inspections were performed at the same locations on all four girders (Figure 6.8).

Figure 6.7 Inspectors performing GPR on: (a and b) the girder's web; (c and d) the girder's lower flange.

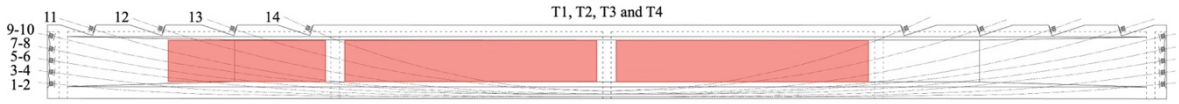

Figure 6.8 Portions of girders inspected with GPR

For GPR, the detection of corrosion in prestressing cables was the defect of interest, assigned the code GPR.C. The GPR outcomes were presented as amplitude maps, representing the reflected electromagnetic energy recorded by the antenna. The specialized practitioners interpreted areas coloured in red as areas with corrosion in prestressing cables; therefore, based on these line guides, the defect intensity scale represented in Figure 6.9 was defined to interpret the GPR outcomes. The scale shows three 10 cm long samples with the three different defect intensity levels chosen to quantify the defectiveness of each section of the cables analysed with GPR. Level "0" describes a sample without the presence of corrosion; level "1" describes a sample with a light level of corrosion; and level "2" describes a sample with a high level of corrosion.

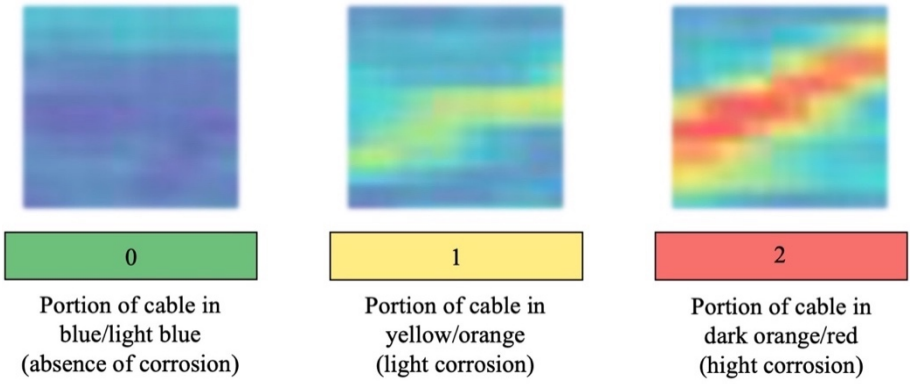

Figure 6.9 Defect intensity scale to interpret GPR outcomes and identify corrosion in the prestressing system.

The GPR outcomes were overlapped with the girders' longitudinal sections reconstructed in a CAD environment, as shown in Figure 6.10. The intensity of steel corrosion identified based on the GPR outcomes was assigned to each segment of the prestressing cables (sample).

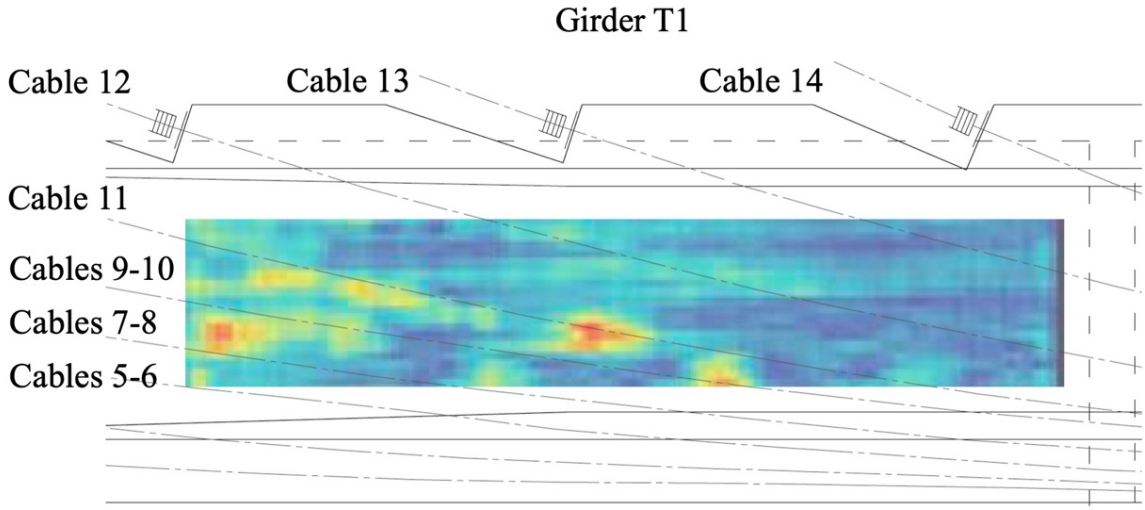

Figure 6.10 Superposition of a portion of GPR outputs over the corresponding area of the longitudinal section of the girder T1.

Reflectometric Impulse Measurements Test (RIMT). RIMT works by sending a high-energy electromagnetic pulse into the cable and analysing the reflected signal. By measuring the time delay and amplitude of the reflections, RIMT can detect anomalies such as corrosion, cracks, and voids within the cable. During the test, a RIMT instrument is connected to one end of the cable, and the pulse is generated and sent through the cable. The instrument records the reflections that occur along the cable's length. RIMT relies on the principle that changes in the cable's physical properties, such as corrosion or damage, will cause variations in the reflected signals. These variations are then analysed to determine the location and severity of any anomalies present in the cable [171] [172].

In this study, the RIMT2® instrumentation was used, which included a transmitter with adjustable impulse duration (2 ns – 1 ms) and amplitude (0 V - +16 V), and max sampling frequency equal to 1 GHz. The device was connected to the prestressing steel cables at the anchorages after removing the concrete cover and cleaning the rust from the steel wires with a metallic brush. RIMT was applied to ten cables anchored at the end of girders T1 and T2 in the Naples direction. The access was possible thanks to the displacement experienced by the

span C2sx during the 2005 landslide, which opened some space between the inspected span and the adjacent one.

Figure 6.11 shows RIMT2® instrumentation and the inspector performing the test. Figure 6.12 shows the tested cables.

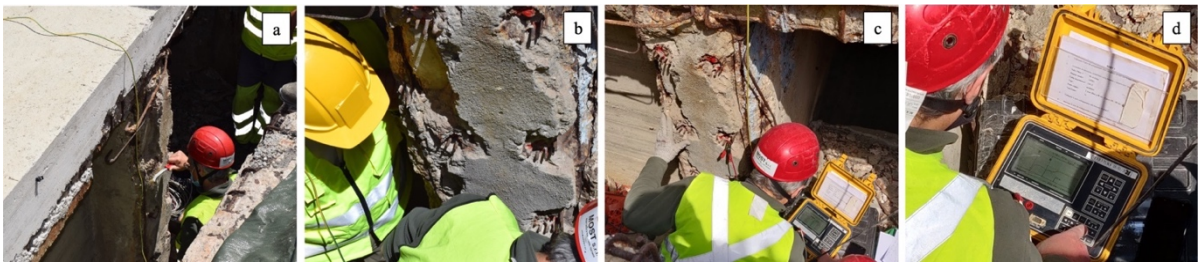

Figure 6.11 a) Inspector cleaning the rust from the steel wires with a metallic brush; (b) the cleaned steel cables 'anchorages; (c) Inspectors performing RIMT; (d) real-time outcome.

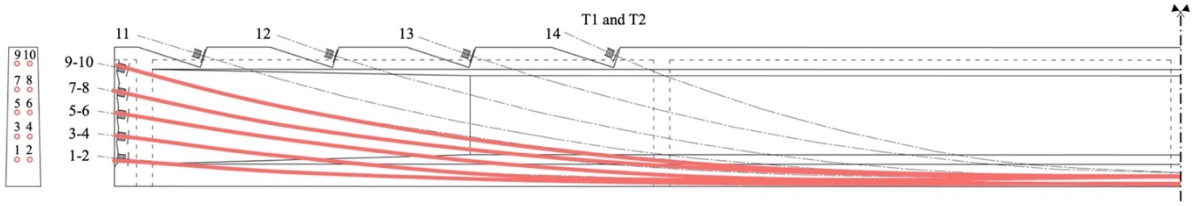

Figure 6.12 Prestressing cables investigated with RIMT.

For RIMT, the defects of interest were the presence of grout void (code RIMT.V) and the presence of corrosion along the cable (code RIMT.C). The interpretation of RIMT outcomes was performed by specialized practitioners who assigned classes of defect intensity levels based on the classification method reported in Table 6.1.

Level		**Type of signal recorded**	**Possible defect**	**Qualitative scale and suggestions**
Injected grout anomaly	1	Very slight signal variation from the ideal trend	Micro-fracture of the injected grout; very small absence of grout (10-15 %)	Negligible defect if no aggressive agents are present or they cannot reach the cable
	2	Small signal variation from the ideal trend	Small fracture of the injected grout; small absence of grout (20-25 %)	Small defect if no aggressive agents are present or they cannot reach the cable
	3	Medium signal variation from the ideal trend	Moderate fracture of the injected grout; moderate absence of grout (30-35 %)	Moderate defect if no aggressive agents are present or they cannot reach the cable
	4	Significant signal variation from the ideal trend	Significant fracture of the injected grout; significant absence of grout (>35 %)	Severe defect that requires prompt repair action and a retrofit of the cable

	5	Hight signal variation from the ideal trend	Total absence of injected grout	Severe defect that requires a prompt visual inspection to understand whether the cable can be repaired
Corrosion anomaly	1	Very slight signal variation from the ideal trend	Superficial oxidation of the steel components of the cable	Small defect with neglectable area reduction
	2	Small signal variation from the ideal trend	Local oxidation the steel components and diffuse pitting (at least 7-10 cm)	Small defect. The monitoring of the corrosion is recommended every 1-2 years
	3	Medium signal variation from the ideal trend	Severe and diffuse pitting in steel components.	Medium defect with presence of area reduction. The monitoring of the corrosion is recommended every 6-12 months with endoscopic inspection
	4	Significant signal variation from the ideal trend	Diffuse and severe corrosion of steel elements	Severe defect with significant area reduction. The monitoring of the corrosion is recommended every month with endoscopic inspection
	5	Hight signal variation from the ideal trend	Highly diffuse and severe corrosion of steel elements	Severe defect with area reduction that compromises the cable function. Urgent visual inspection and retrofit are required.

Table 6.1 Defect intensity scale to interpret RIMT outcomes and identify the presence of grouting voids and corrosion in the prestressing system.

6.3.3 Dissection of the prestressing system

After completing the testing campaign, a controlled demolition of the analysed span, C3sx, was carried out. The primary objective was to extract the prestressing system. The demolition process involved removing the concrete slab and the cross-girders from the four girders. The girders were then moved to the ground using a mobile crane and demolished using an excavator hydraulic crusher pliers, with precautions taken to avoid disturbing the prestressing system. The extracted cables were placed on the ground, and their dissection was performed to assess their actual condition state. Figure 6.13 illustrates the various steps of the demolition and mapping process.

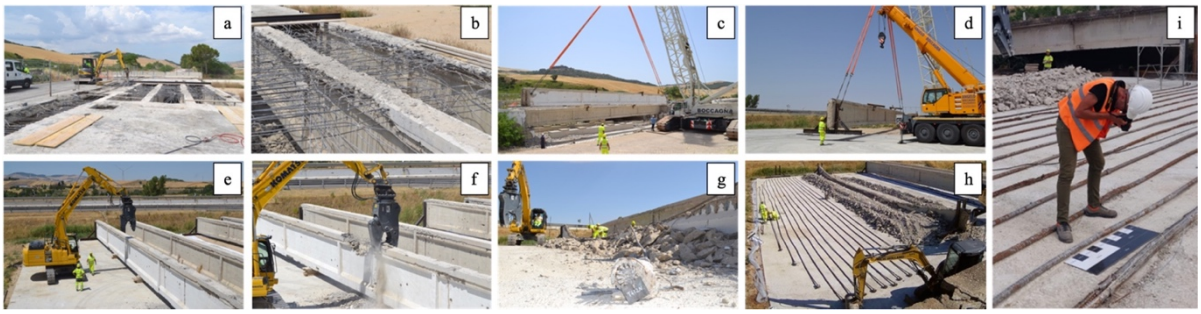

Figure 6.13 a) demolition of the concrete slab; (b) demolition of the 5 cross-girders; (c) movement of the girders; (d) positioning of the girders on the ground; (e) excavator with the hydraulic crusher pliers; (f) demolition of the girders; (g)

extraction of the prestressing system; (h)positioning of the prestressing cables on the ground; (i) mapping of the actual state of the prestressing system.

As described in subsection 6.3.1, the cables were discretised into 10 cm-long segments called samples and assigned the intensity classes for the defects observed during the autopsy to each sample. For each cable, arrays of defect intensity classes were created, with one array per defect type. Specifically, the actual condition state of three main components of the prestressing system was mapped: the metal ducts, the injected grout, and the steel wires.

The following subsections detail the intensity scales used to map each of the defects describing the condition state of the three main components of the analysed prestressing system.

Condition state of the metal ducts. This subsection describes the quantity scales used to map the intensity of the three defects identified to describe the actual condition state of the steel corrugated metal ducts: corrosion (defect individuated with the D.C code, describes the fraction of area of the 10 cm sample of the corroded or oxidised metal duct), absence of integrity (defect individuated with the D.A code, describes the fraction of area of the 10 cm sample not intact, i.e. with cuts, tears, perforations or wherever the duct is missing), and perforation (defect individuated with the D.P code, describes the fraction of area of the 10 cm sample of the missing metal duct). An intensity scale was defined to quantify the fraction of surface area (expressed in sixteenths) affected by the deficiency. For this purpose, the surface area of a 10 cm long duct sample is conceptually divided into sixteen portions, with each of the four corrugation rings that make up a segment divided into quarters.

Figure 16.4 illustrates the various portions of the sample of the metal duct sample.

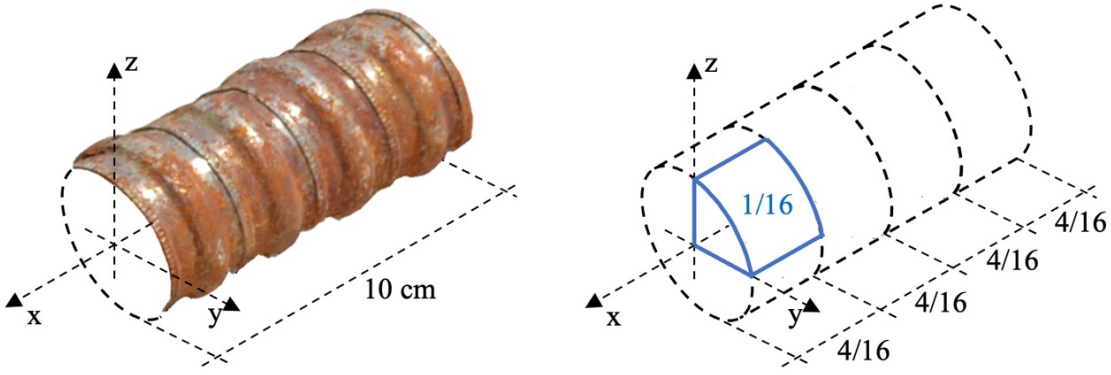

Figure 6.14 Discretisation in sixteenths of the samples used to map the actual condition state of the metal ducts.

In Figure 6.15, photographic documentation illustrates the mapping of the three types of defects that can impact the condition of metal ducts. Varying intensity levels represent each

defect: no defect, indicated by a defect intensity of 0/16; an intermediate defect, represented by a defect intensity of 8/16; and a severe defect, represented by a defect intensity of 16/16.

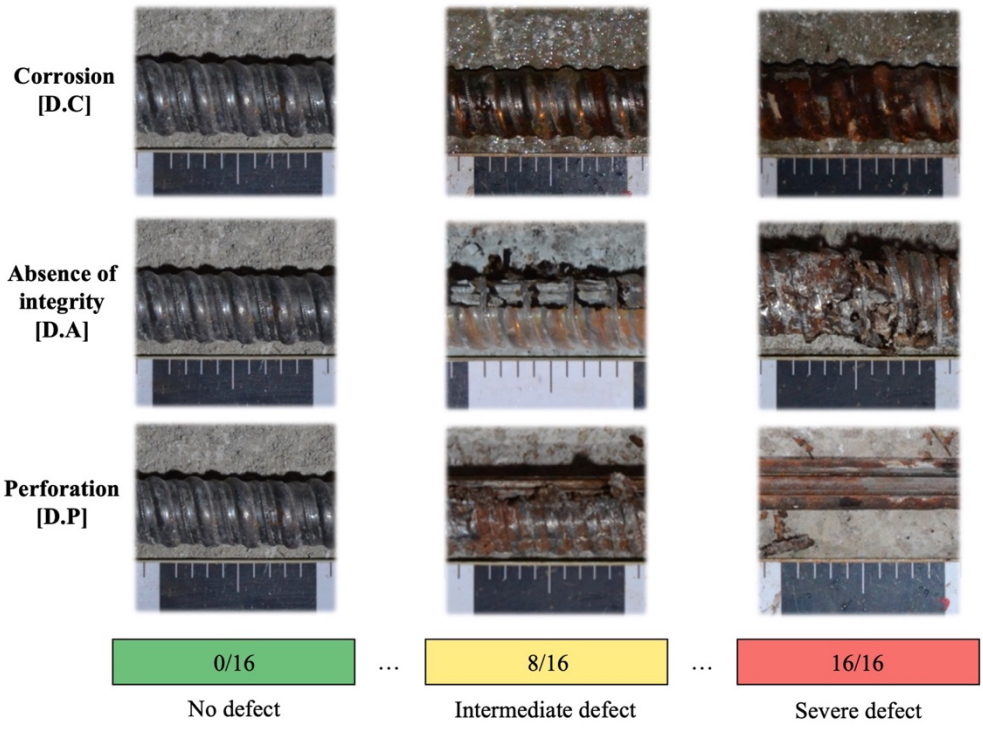

Figure 6.15 Intensity scales to quantify the defects which can affect the metal ducts in the prestressing system.

Condition state of the injected grout. This subsection details the quality scales used to map the intensity of the two defects affecting the condition state of the injected grout. A five-class scale was used for describing the grade of grout fracturing (defect individuated with the G.F code, describes the grade of grout fracturing of the 10 cm sample analysed), while a six-class scale composed was used to describe the percentage of grouting void (defect individuated with the G.V code, describes in percentage the presence of grout void of the 10 cm sample analysed). Figure 6.16 and Figure 6.17 show the quality scales introduced above. It is essential to consider that a high level of grout fracturing defect (G.F) in an analysed 10 cm long sample does not exclude the possibility that the same sample is completely or partially injected. Conversely, a sample with a complete lack of injected grout is not assigned any level of grout fracturing.

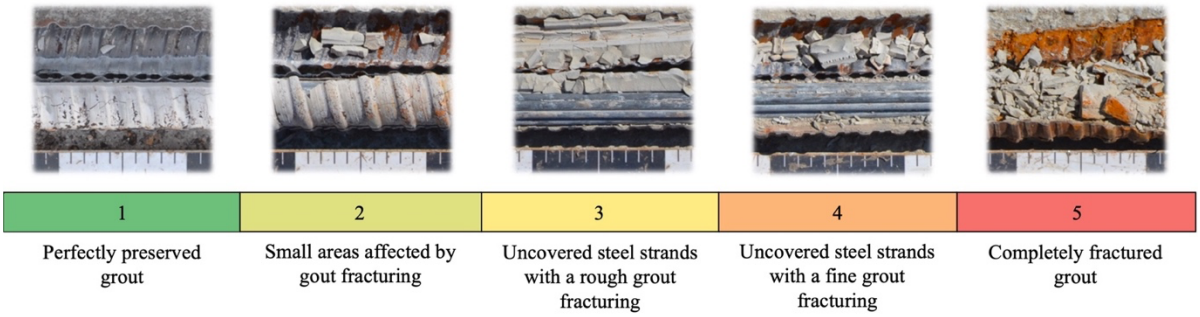

Figure 6.16 Intensity scale used to classify the grade of grout fracturing (G.F) in the prestressing system.

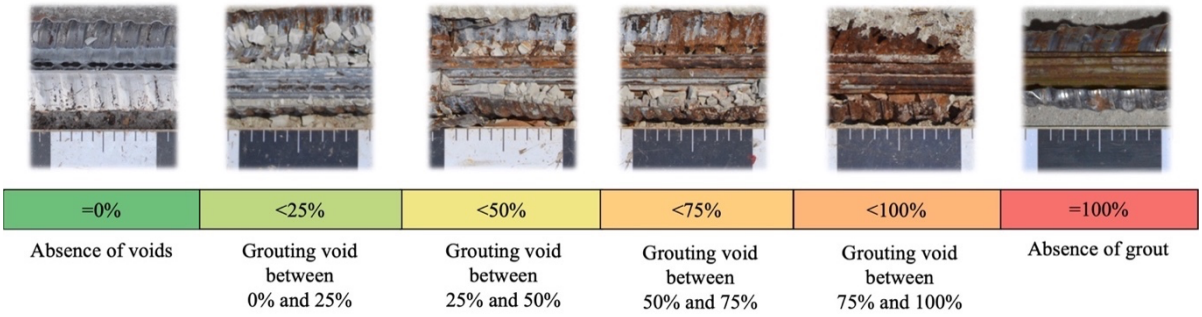

Figure 6.17 Intensity scale used to classify percentage of grouting void (G.V) in the prestressing system.

Condition state of the steel wires. This subsection reports the quantity scales used to quantify the intensity of three defects that characterise the actual condition state of the steel wires: the presence of corrosion (defect individuated with the S.C code, quantifies the number of wires within the analysed 10 cm sample affected by corrosion or oxidation), the area reduction (defect individuated with the S.R code quantifies the percentage of loss of resistant area in the 10 cm long sample analysed), and the presence of interruptions (defect individuated with the S.I code, it quantifies the number of wires within the analysed 10 cm sample affected by breaks).

An intensity scale based on twelfths was used to quantify the corrosion and interruption defects. This scale was chosen because each cable comprises twelve 7 mm diameter steel wires. Figure 6.18 illustrates the discretisation of the samples used to map the actual condition state of these two defects in the last component of the mapped prestressing system.

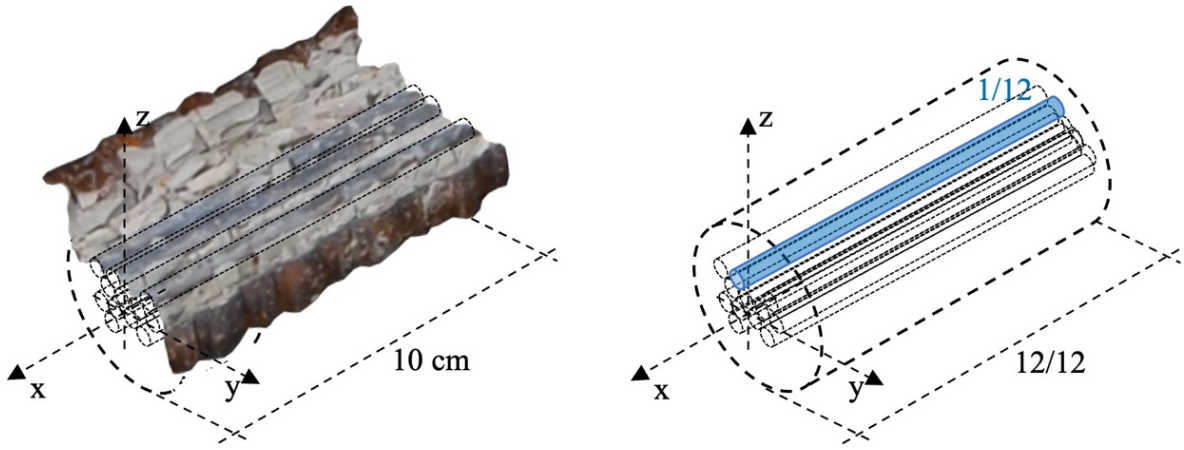

Figure 6.18 Discretisation in twelfths of the samples used to map the actual condition state of two defects which can affect the steel wires.

In Figure 6.19, photographic documentation illustrates the mapping of the corrosion and interruption defects that can impact the condition state of the steel wires. Varying intensity levels represent each defect: no defect, indicated by an intensity of 0/12; an intermediate defect, represented by a defect intensity of 6/12; and a severe defect, depicted by a defect intensity of 12/12.

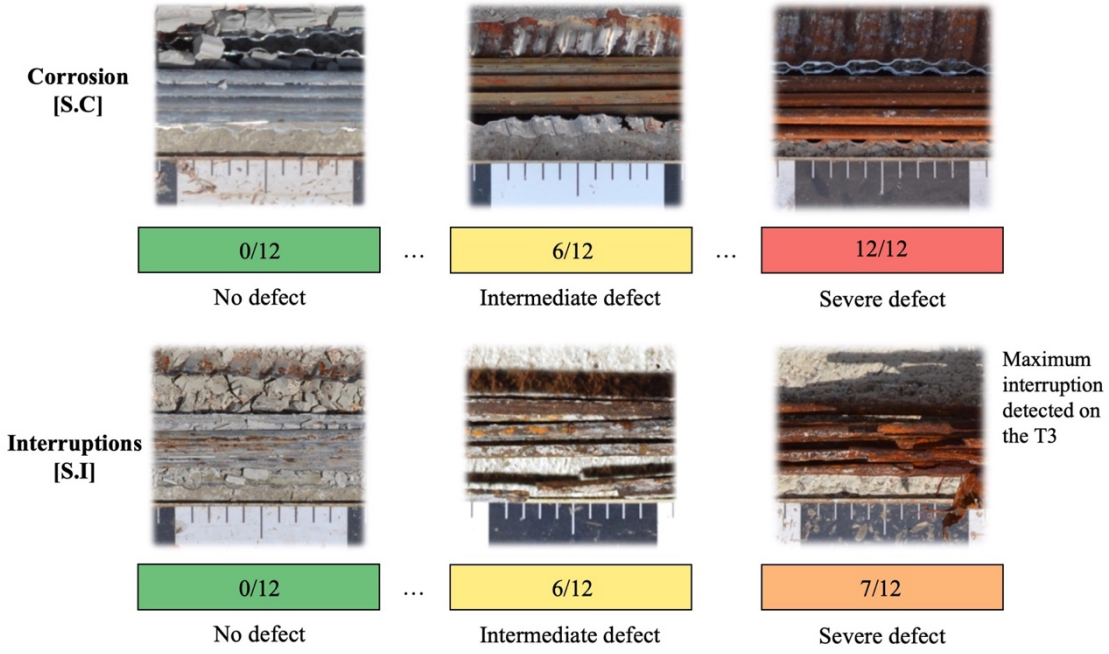

Figure 6.19 Intensity scales used to quantify the steel wires corrosion (S.C) and the steel wires interruptions (S.I) in the prestressing system.

Regarding the mapping of the actual condition state of the other defect, which describes the actual condition state of the steel wires, the area reduction (S.R), was made transverse cuts to obtain a cross-sectional view of the cable. In this way, it was possible to quantify the loss of

resistant cross-section as accurately as possible through a post-processing elaboration of the transverse cut picture. It was decided to make the cut in the sample with the most significant area reduction and then proceed with linear interpolation to where the phenomenon within the meter analysed was observed. For example, in Figure 6.20, within the meter of cable represented, corrosion was observed only in the 10-cm long samples 7-10, with sample 9 characterised by the highest area reduction. Therefore, sample 9 was cut, measured the area reduction, assigned zero area reduction to segments 6 and the end of segment 10, and calculated the area reduction of segments 7, 8, 10 through linear interpolation.

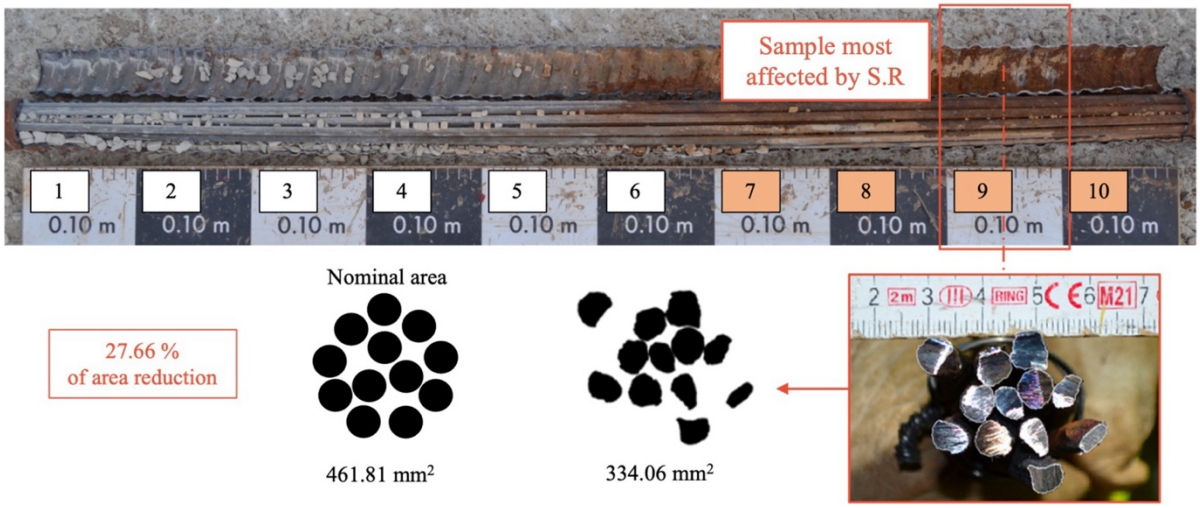

Figure 6.20 Example of quantification of the area reduction (S.R) in the corroded samples.

The area reduction defect was expressed in terms of the percentage of area loss with respect to the nominal one. Six discrete classes of percentage reduction of area were considered to homogenise this correlation analysis with respect to the others. For this purpose, the level variation range was divided into six classes that made it possible to have sufficient samples in each class.

Figure 6.21 illustrates, as an example, three different intensities of area reduction detected: without defect (defect intensity = 0%), with intermediate defect intensity (defect intensity ≤ 5%) and with maximum defect intensity (defect intensity of > 20%).

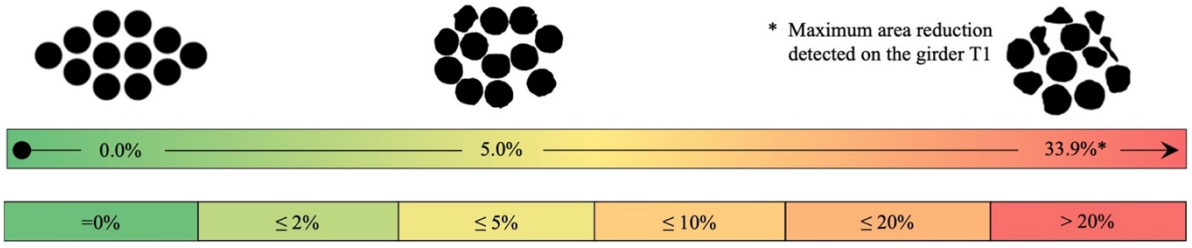

Figure 6.21 Intensity scale used to classify the steel threads area reduction (S.R) in the prestressing system.

6.4 Correlation analysis

This subsection describes the correlation analysis performed to quantify the effectiveness of the various NDT methods and the metrics used. In statistics, association and correlation are often used interchangeably; however, these have different meanings [173]. Association refers to any relationship between two variables (i.e., one variable provides information about another). In contrast, correlation qualifies as measuring the strength and direction of the relationship between the two variables. In this context, the direction of a relationship stands for the tendency of two variables to increase or decrease simultaneously (direct correlation-positive) or not simultaneously (inverse correlation-negative).

To evaluate the correlation between the NDTs outcomes and the intensity classes of defects, contingency tables are considered [163]. Contingency tables (also known as cross-tabulations or two-way tables) are a statistical tool used to analyse the relationship between two categorical variables, often used in social science, medical research, and economic research. Categorical variables represent characteristics or attributes that can be classified into two or more specific classes [174]. These classes are not characterized by a continuous measurement scale but discrete, qualitative values. Ordinal variables are involved in this study. These are categorical variables whose classes have a specific logical order despite not providing a mathematically meaningful numerical quantity [175]. An example of ordinal variables are Likert scales [176], [177], such as the 5-point scale ["Very poor," "Poor," "Acceptable," "Good," "Very good"]. Note that the classes of such variables are discrete and qualitative, following a definite logical order; however, it is not possible to uniquely quantify the distance between two classes, although it is certain that there is a certain threshold separating them.

Given two ordinal variables, a contingency table reports the frequency of occurrence for each combination of their classes. The rows and columns of the contingency tables represent the classes of the two variables of interest. The row indices and column indices follow the logical order of the classes of the variables. The frequency of occurrence of each combination of classes is reported in the corresponding cell of the contingency tables.

As mentioned above, this study aims to verify the correlation between two different variables: the outcomes of a specific NDT (on the rows) and the intensity classes of a particular defect in the prestressing system resulting from its autopsy (on the columns). These two variables are represented by the ordered discrete sets Ω_y and Ω_θ, respectively. These sets are defined in

Equation (6.1), where y_i is the *i*-th class of Ω_y, θ_j is the *j*-th class of Ω_θ, and m_y and m_θ are the number of classes included in Ω_y and Ω_θ, respectively.

$$\Omega_y \coloneqq \{y_1, y_2, \dots, y_{m_y}\}; \qquad \Omega_\theta \coloneqq \{\theta_1, \theta_2, \dots, \theta_{m_\theta}\}; \tag{6.1}$$

It is possible to verify whether two variables are correlated by analysing the contingency table (CT) defined in Equation 6.2, where n_{ij} is the frequency of occurrence of the pair $(\mathrm{y_i}, \theta_\mathrm{j})$.

$$CT \in \mathbb{N}^{m_y} \times \mathbb{N}^{m_\theta} \quad \text{and} \quad \{CT\}_{ij} = n_{ij} \tag{6.2}$$

By normalising the frequencies reported in a contingency table with respect to the sum of the rows or with respect to the sum of the columns, it is possible to obtain a conditional probability table [175], [178]. This table is a discrete representation of a conditional probability distribution, quantifying the probability of a certain event or outcome based on a conditional variable.

Since the objective is to test whether the NDT outcomes Y are correlated with the defect in the prestressing system of interest Θ, the frequencies n_{ij} are normalised by dividing them by the number of entries in the various defect classes. Thus, the conditional probability table (CPT) defined in Equation 6.3 is obtained, where $p_{ij} = p(y_i|\theta_j)$ is the conditional probability of having result y_i given defect class θ_j, whereas n_j is the recurrence frequency of defect class θ_j, i.e., the sum of the frequencies in the *j*-th column of the contingency table.

$$CPT \in \mathbb{R}^{m_y} \times \mathbb{R}^{m_\theta} \quad \text{and} \quad \{CPT\}_{ij} = p_{ij} = n_{ij}/n_j \tag{6.3}$$

Finally, by normalizing the frequencies n_{ij} with respect to the total number of occurrences n it is possible to obtain the joint probability table (JPT) [175], as in Equation 6.4.

$$JPT \in \mathbb{R}^{m_y} \times \mathbb{R}^{m_\theta} \quad \text{and} \quad \{JPT\}_{ij} = \pi_{ij} = n_{ij}/n \tag{6.4}$$

When an NDT is not correlated with a defect, the relative contingency table will be characterized by approximately evenly distributed columns (i.e., approximately equal numbers of occurrences in each cell). In fact, in this case, the results of the NDT do not depend on the intensity of the defect. In contrast, when the NDT outcomes Y are strongly correlated with a defect Θ, the relative contingency table elements (and the correlated conditional probability table elements) follow approximately a monotonic trend.

In the scientific literature, several metrics measure the degree of correlation between two variables, i.e., the relative measure of correlation. This study uses the Spearman's correlation coefficient (SpearCC) [164]. This coefficient is a real number between -1 and 1 with a value equal to 1, identifying a perfect and direct correlation between the variables. A correlation coefficient equal to -1 identifies a perfect and inverse correlation between the variables, whereas a correlation coefficient equal to 0 implies a lack of a monotonous dependency between the variables. In all other cases, a correlation (direct or inverse, depending on the sign) between the variables exists but is imperfect. An example of this is shown in Figure 6.22.

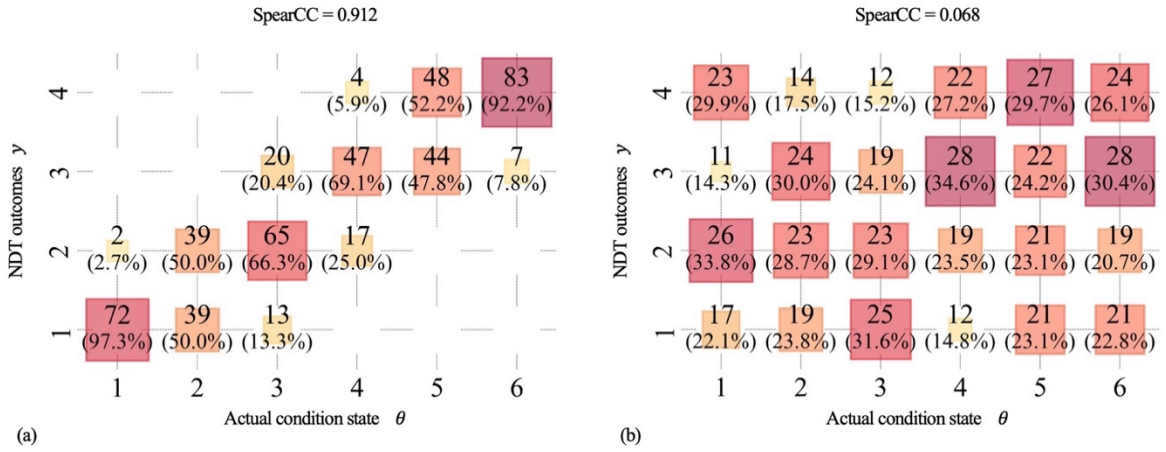

Figure 6.22 Examples of contingency tables. a) case with very strong correlation; b) case with poor correlation.

The Spearman's correlation coefficient is chosen because it measures the monotonic relationship between two variables, evaluated with respect to the ordinal ranks of the variables [165], i.e., a general relationship (not necessarily linear) in which its direction remains constant. Alternative correlation metrics are considered to ensure that the choice of metric does not influence the result obtained on the level of correlation between the ordinal variables. These include the Pearson's correlation coefficient (PearsCC) [165], the Polychoric correlation coefficient (PolyCC) [14] [167], the Goodman-Kruskal Gamma (GKγ) [168], and the Stuart-Kendall Tau-c (SKτ) [169], [170].

The metrics listed above are suitable for interpreting non-square contingency tables of ordinal variables, although, for some of these, it is necessary to introduce some assumptions. The Pearson correlation coefficient, also known as Pearson's linear correlation, is a statistical metric that indicates the strength and the direction of the linear relationship between two continuous variables. The Pearson Correlation Coefficient is calculated by dividing the covariance between the two variables by the product of their standard deviations. Since the

variables involved are not continuous but ordinal, using Pearson's coefficient might be inappropriate if the variable are not ranked [179].

Another alternative to Spearman's correlation coefficient is the Kendall rank correlation coefficient (also known as the Kendall Tau coefficient). The Kendall Tau coefficient evaluates the strength of the correlation between the two variables based on the number of concordances and discordances between all possible realizations of the two variables, Y and Θ. The pair of realizations (y_i, θ_j) and (y_k, θ_p) is said to be concordant if it is true that if $y_i < y_k$ and $\theta_j < \theta_p$ or if it is true that $y_i > y_k$ and $\theta_j > \theta_p$. Oppositely, such a pair of realizations is said to be discordant if $y_i < y_k$ and $\theta_j > \theta_p$ or if it is true $y_i > y_k$ and $\theta_j < \theta_p$. Usually, the Kendall-Tau coefficient returns smaller values than the analogous Spearman's Correlation Coefficient [180]. In this work the Stuart-Kendall variant (or simply named Tau-c) of the Kendall Tau coefficient is considered. This is better suited to non-square contingency tables [181] and is defined in Equation 6.5:

$$\mathrm{SK}\tau_c = \frac{2\,(n_c - n_d)}{n^2} \cdot \frac{m}{m-1} \tag{6.5}$$

where n_c is the number of concordant pairs, n_d is the number of discordant pairs, n is the total number of occurrences, and m is the minimum between the number of rows m_y and the of columns m_θ.

A similar metric to the Kendall Rank correlation coefficient is the Goodman-Kruskal Gamma [175], [182], evaluated as in Equation (6.6).

$$\mathrm{GK}\gamma = \frac{n_c - n_d}{n_c + n_d} \tag{6.6}$$

Finally, Polychoric correlation is a technique aimed at estimating the correlation between two ordinal variables assuming the existence of two continuous latent variables distributed according to a multivariate distribution with correlation coefficient ρ [183], [184]. Latent variables (also known as hidden or unobservable variables) cannot be measured or observed directly but can influence the relationships between the observed variables [26]. In this case, latent variables represent a continuous equivalent of the observed ordinal variables. Moreover, the ordinal variables are subsets of the latent variables separated by thresholds t not generally specified. In a nutshell, the Polychoric correlation technique finds the best combination of the thresholds t^* and the best correlation coefficient ρ^* that returns an

estimated joint probability table JPT (see Equation 6.4) as close as possible to the observed one. The corresponding correlation coefficient ρ^* is the actual Polychoric Correlation Coefficient. The Polychoric correlation comes from the Polychoric Series, which was used to estimate the Polychoric correlation coefficient [36]. However, nowadays, this coefficient is estimated more reliably through the maximum likelihood (ML) method [185] or by other numerical methods (i.e., MCMC methods) [186]. In this work, the Polychoric correlation coefficient is estimated through the ML method using the *polycor* package [187] in R Studio [188].

6.5 Results

This section presents the results obtained by assigning intensity classes to the samples along the cables based on the defects detected through NDTs and the results observed during the dissection. Subsection 6.4.1 focuses on the interpretation of the NDT outcomes provided by DR, GPR, and RIMT, whereas Subsection 6.4.2 focuses on two defects observed during the dissection in the injected grout and the corrosion defect that affects the steel wires, which serve as ground truth for the correlation analysis presented in section 6.

6.5.1 Interpretation of the NDTs outcomes

This subsection provides a graphical representation of the defect intensity classes assigned to the samples based on the NDTs outcomes. The classes are represented in colour scale and the samples are represented in their location along the prestressing cables. The defect intensity classes have been introduced in subsection 6.3.2; in the figures, the colours depend on the intensity of the defects and the colour scale goes from green – no defect – to red – severe defect.

Digital Radiography (DR). DR was used to investigate the presence of grouting void (DR.V) within the metal ducts of the prestressing system. Different portions of cables were tested in different girders, mostly in the girder T1, as indicated in Figure 6.23. Specifically, the following cables were inspected: cables 5 to 14 in the girder T1, cables 9 to 14 in the girder T2, and cables 12 to 14 in girders T3 and T4. It is recalled that T1 and T4 are the external girders.

DR revealed a high presence of grouting void near the anchorages of the cables, with no significant differences between cables anchored at the end of the girders and those anchored in the slab. According to the practitioners who performed the DR tests, with DR tests it was not possible to distinguish between parallel cables within the same girder. Therefore, the

same defect intensity classes were assigned to cable pairs that are horizontally overlapped along the girders. Furthermore, it was impossible to interpret the results of the investigations carried out in the lower flange of the girder T1, because the high concentration of cables did not allow the interpretation of the X-ray images and the identification of the different cables present.

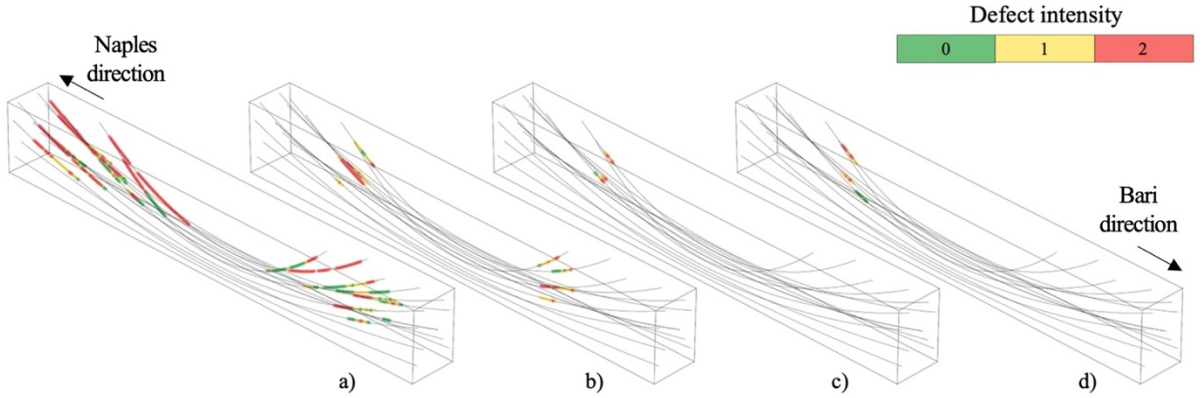

Figure 6.23 Intensity of grouting void (G.V) defect of the samples in the portions of cables investigated with DR (DR.V). (a) Girder T1, 721 samples; (b) girder T2, 152 samples; (c) girder T3, 20 samples; (d) girder T4, 31 samples.

Ground Penetration Radar (GPR). GPR was used to investigate the presence of corrosion along the cables (GPR.C). The same portion of cables – from number 7 to 14 – were tested in the four girders, as shown in Figure 6.24. GPR revealed a high presence of corrosion in the external girders (T1 and T4), with the highest level of defect concentrated near the cable anchorages. Similar to DR tests, it was not possible to distinguish horizontally overlapped cables within the same girder, so the same defect intensity classes were assigned to cable pairs that run parallel along the girders.

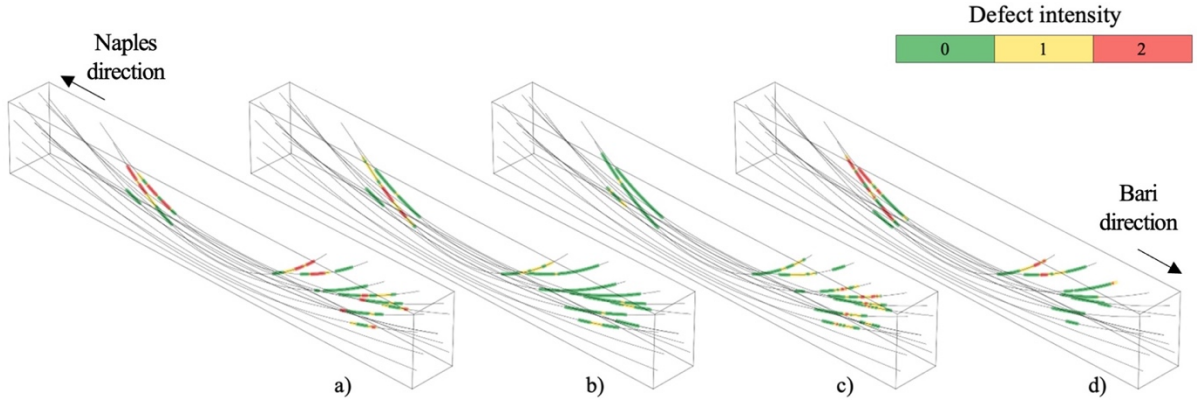

Figure 6.24 Intensity of corrosion of the samples in the portions of cables investigated with GPR (GPR.C). (a) Girder T1, 325 samples; 8b) girder T2, 486 samples; (c) girder T3, 406 samples; (d) girder T4, 308 samples.

Reflectometric Impulse Measurements Test (RIMT). RIMT was used to investigate the presence of grouting void (RIMT.V) and corrosion of the steel cables (RIMT.C). All ten cables anchored at the end of girders T1 and T2 were inspected using RIMT, as indicated in Figures 25 and 26. RIMT revealed a higher level of grouting void and steel cable corrosion near the anchorages and in the midspan sections. The similarity of the outcomes among all cables of the same girder and the regularity of the sequence of green - light-green colours along the cables in Figures 6.25 and 6.26 are peculiar and rise some doubts on the outcomes provided by this technology.

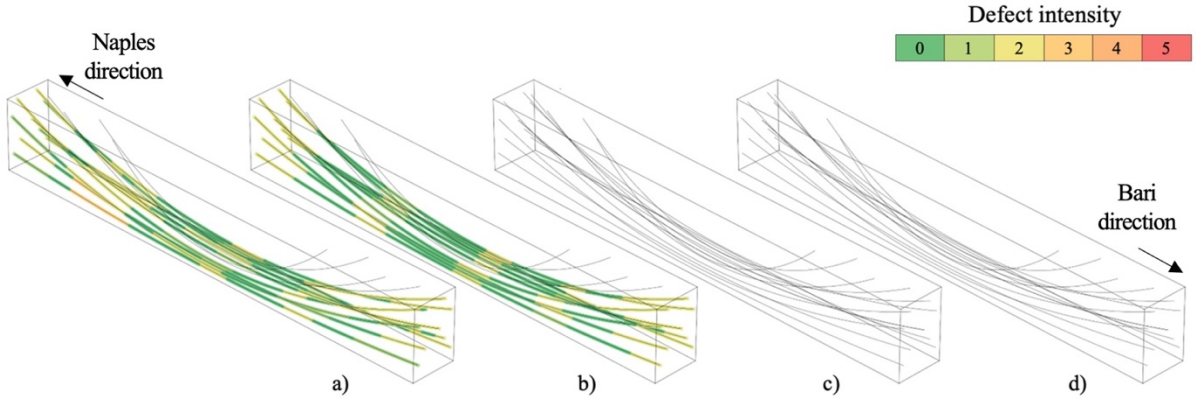

Figure 6.25 Intensity of grouting void of the samples in the portions of cables investigated with RIMT (RIMT.V). (a) Girder T1, 3348 samples; (b) girder T2, 3348 samples; (c) girder T3, 0 samples; (d) girder T4, 0 samples.

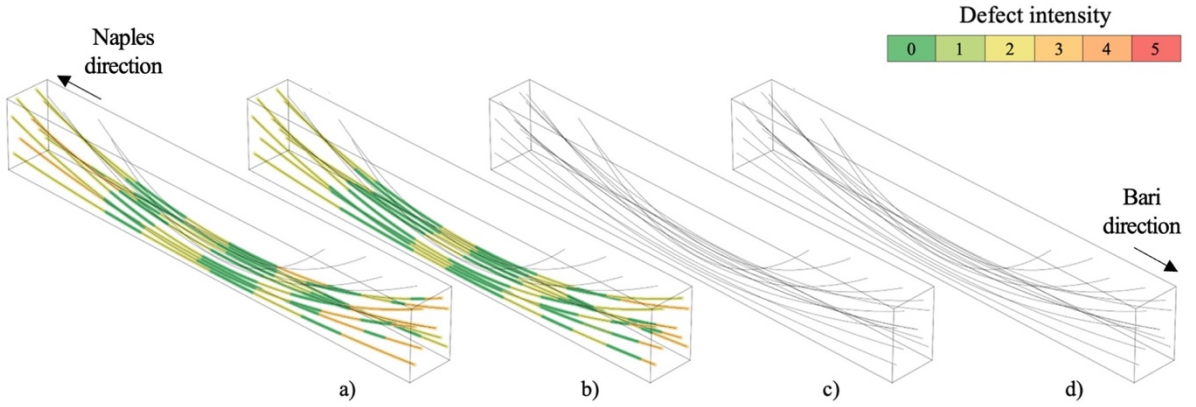

Figure 6.26 Intensity of corrosion of the samples in the portions of cables investigated with RIMT (RIMT.C).
(a) Girder T1, 3348 samples; (b) girder T2, 3348 samples; (c) girder T3, 0 samples; (d) girder T4, 0 samples.

6.5.2 Condition state of the prestressing system

This subsection provides a graphical representation of the actual defect state of the analysed span, especially for the injected grout and steel threads defects. The classes are represented in colour scale and the samples are represented in their location along the cables. The defect intensity classes have been introduced in subsection 6.3.3; in the figures, the colours depend

on the intensity of the defects and the colour scale goes from green – no defect – to red – severe defect. These results are used as ground truth in the correlation analysis presented in section 6.5. During the dissection, the entire length of all cables from all the girders was inspected.

Condition state of the injected grout. The injected grout was examined for the grade of grout fracturing (G.F) and the percentage of grouting void (G.V) along the entire prestressing system of the C3sx span's girders. It was observed high levels of G.F near the anchorages, both in cables anchored at the end of the girders and those anchored in the slab. Girders T1, T2 and T4 also exhibited a high grade of G.F in the midspan sections. A high percentage of G.V was observed near the anchorages as well. These findings suggest a correlation between the presence of G.F and G.V along the cables. In girders T1 and T2, two cables were found to be completely empty of grout – specifically cable 13 in girder T1, and cable 12 in girder T2. Figures 6.27 and 6.28 display the defect intensity classes assigned to the samples for G.F and G.V, respectively.

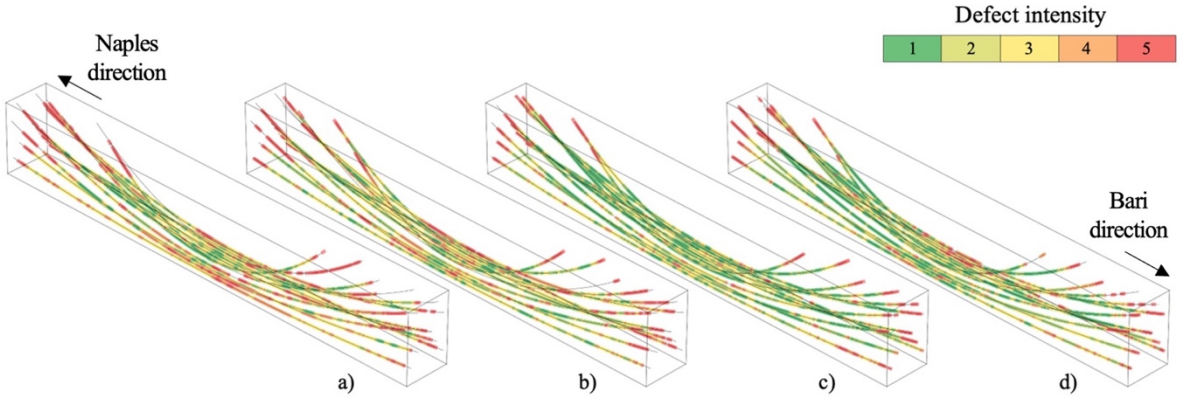

Figure 6.27 Actual grade of grout fracturing (G.F) of the samples observed during the dissection. (a) Girder T1, 3871 samples; (b) girder T2, 3871 samples; (c) girder T3, 4158 samples; (d) girder T4, 4030 samples.

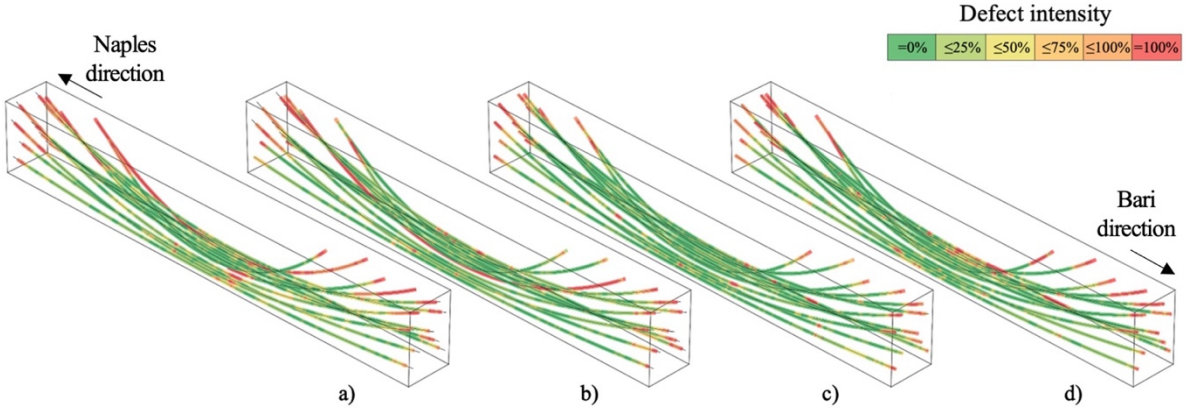

Figure 6.28 Actual percentage of grouting void (G.V) of the samples observed during the dissection.
(a) Girder T1, 4217 samples; (b) girder T2, 4234 samples; (c) girder T3, 4247 samples; (d) girder T4, 4245 samples.

Condition state of the steel cables. The condition state of the steel cables was investigated by examining the level of corrosion in the steel wires (S.C) for each sample. Contrary to expectations, it was observed a high level of steel wires corrosion not in all samples characterized by a high presence of grouting void (G.V). In general, the level of steel wires corrosion (S.C) was low along most cables, with local defects primarily located at the girder edges in cables anchored in the slab, particularly near the anchorages. Surprisingly, cables anchored at the end of the girders rarely exhibited high levels of corrosion. The cable in girder T2 that was not injected with grout showed a high level of corrosion, but contrary to expectations, the cable in girder T1 that was also not injected did not display a similar level of corrosion. Figure 6.29 illustrates the defect intensity classes assigned to the samples for S.C.

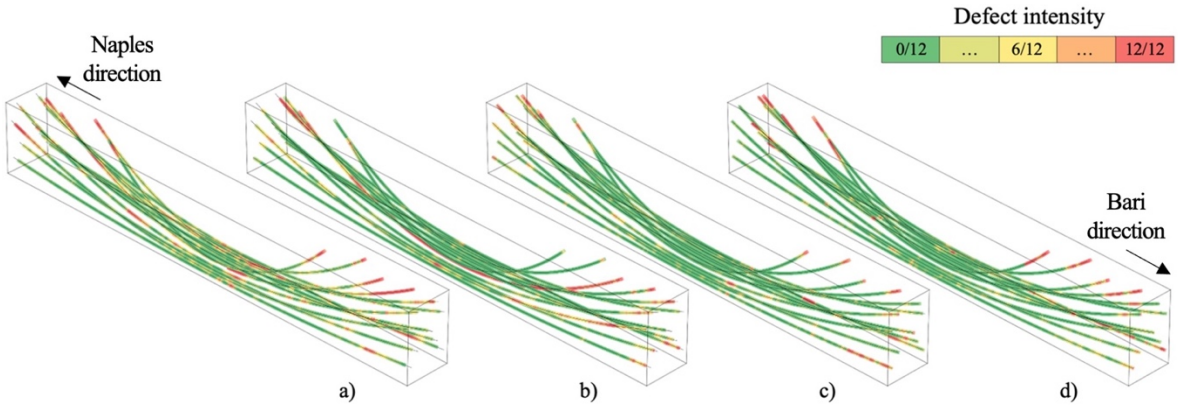

Figure 6.29 Actual intensity of steel corrosion (S.C) of the samples observed during the dissection.
(a) Girder T1, 4219 samples; (b) girder T2, 4235 samples; (c) girder T3, 4252 samples; (d) girder T4, 4256 samples.

6.6 Correlation analysis

This section presents the results of the correlation analysis between the NDTs and the dissection outcomes, considered as the ground truth for this analysis. Subsection 6.5.1 deals with the condition state of the injected grout and Subsection 6.5.2 with the condition state of the steel wires. For each pair of NDT outcome and type of defect, the relative contingency table, the conditional probability table, the Spearman's Correlation Coefficient, and their interpretation are provided.

6.6.1 Condition state of the injected grout

The NDT outcomes considered are DR.V and RIMT.V. These are paired with the defects in the injected grout, specifically, the grade of grout fracturing (G.F) and the percentage of

grouting void (G.V). Figure 6.30 provides a qualitative comparison between these NDT outcomes and the defects observed in the injected grout during the autopsy of cables C8, C9, and C10 of girder T1. The colour map used in the comparison ranges from green to red, representing the severity class of the defect, from no defect to severe defect, respectively.

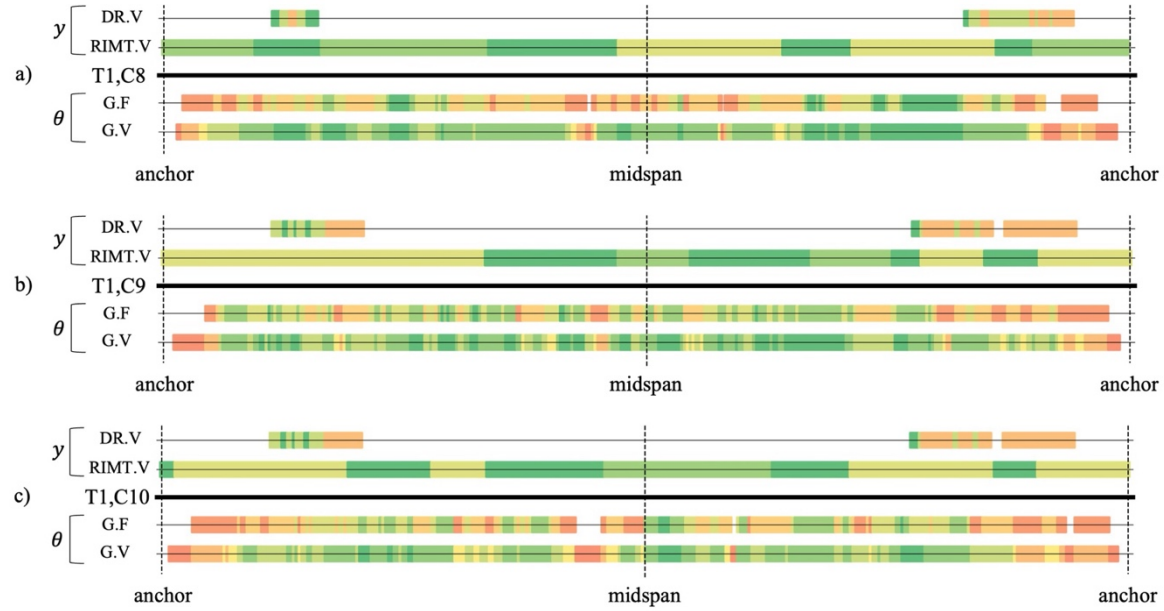

Figure 6.30 Comparison between NDTs outputs and the actual intensity of defects observed in the injected grout. (a) Cable 8, (b) cable 9, (c) cable 10 of the girder T1.

The comparison of the outcomes of the DR method (DR.V) with the actual condition state of the grout fracturing (G.F) and grouting void (G.V) shows values of the Spearman's correlation coefficient of 0.415 and 0.474 (Figure 6.31 and Figure 6.32), which indicates a moderate correlation. These findings demonstrate a significant correlation between the DR outcomes and the actual condition of the injected grout in both cases, as the contingency tables and conditional probability tables mostly showed diagonal elements.

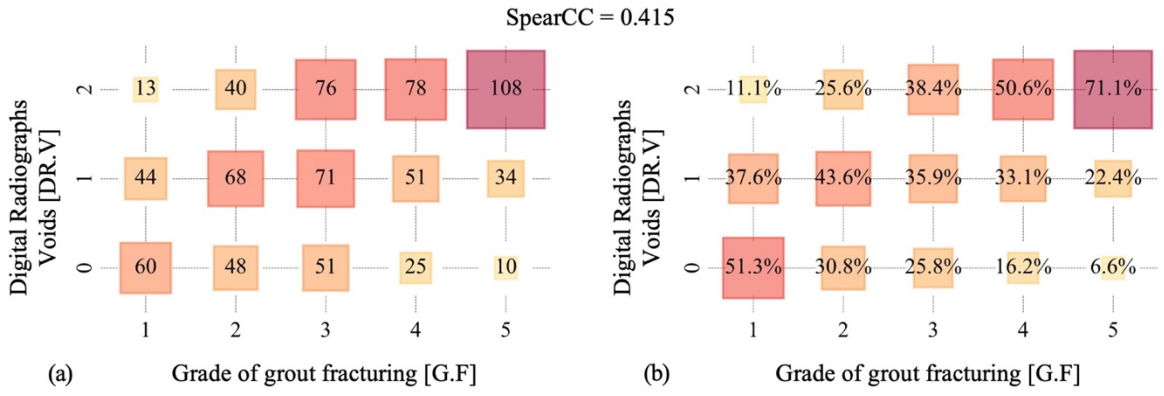

Figure 6.31 Comparison between DR.V and G.F.

(a) Contingency table; (b) Conditional probability table. Above the tables the corresponding Spearman's correlation coefficient is reported.

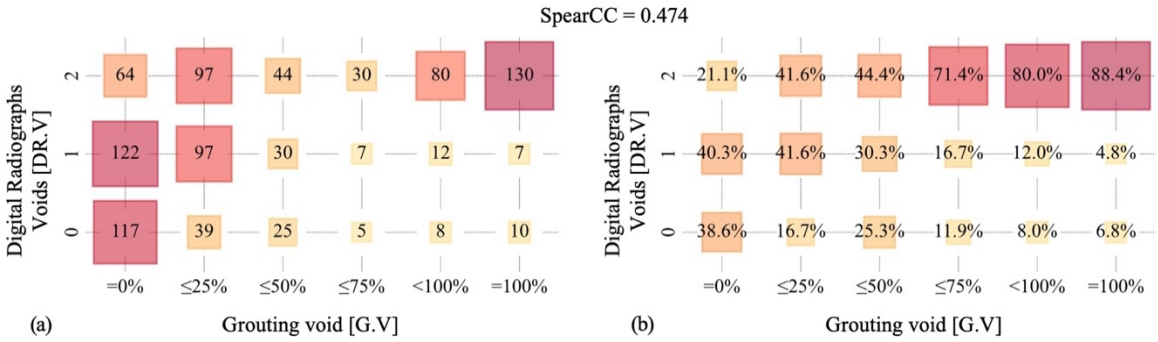

Figure 6.32 Comparison between DR.V and G.V.

(a) Contingency table; (b) Conditional probability table. Above the tables the corresponding Spearman's correlation coefficient is reported.

For the reasons reported in Subsection 6.4.1, the same defect intensity classes were assigned to cable pairs, which are horizontally overlapped along the girders. Thus, there could be misclassifications due to this approximation. In fact, by confining the correlation analysis between the DR outcomes (DR.V) with the actual condition state grouting void (G.V) only to the cables anchored at the slab (cables 11, 12, 13 and 14), which are single, a better Spearman's correlation coefficient value was obtained. Figure 6.33 shows the corresponding contingency table and conditional probability table.

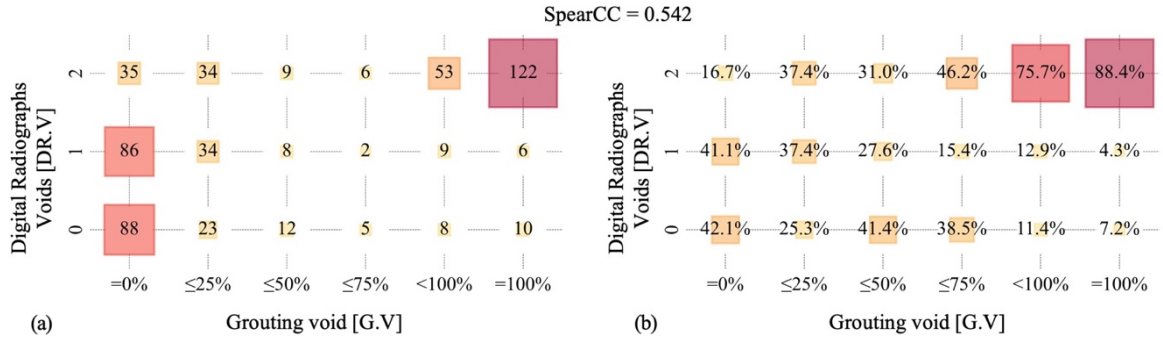

Figure 6.33 Comparison between DR.V and G.V limited at the cables anchored at the slab. (a) Contingency table; (b) Conditional probability table. Above the tables the Spearman's correlation coefficient is reported.

Finally, comparing RIMT outcomes (RIMT.V) with the actual condition state of the grout fracturing (G.F) and grouting void (G.V), low values of Spearman's correlation coefficient were obtained, ranging from 0.101 to 0.167 (Figure 6.34 and Figure 6.35), which suggests a poor correlation.

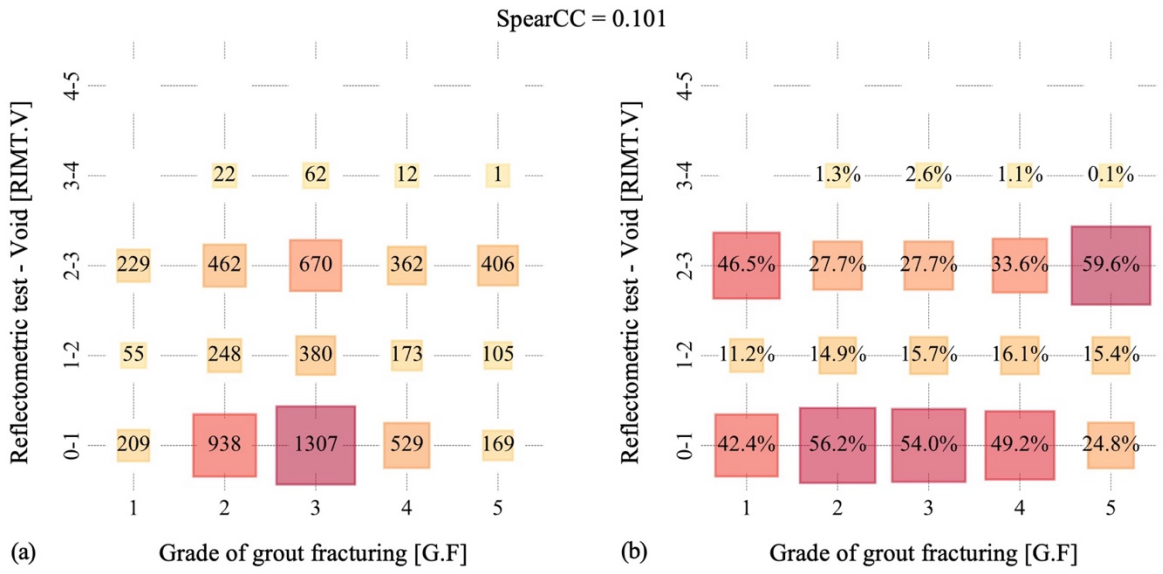

Figure 6.34 Comparison between RIMT.V and G.F. (a) Contingency table; (b) conditional probability table. In the upside the Spearman's correlation coefficient obtained.

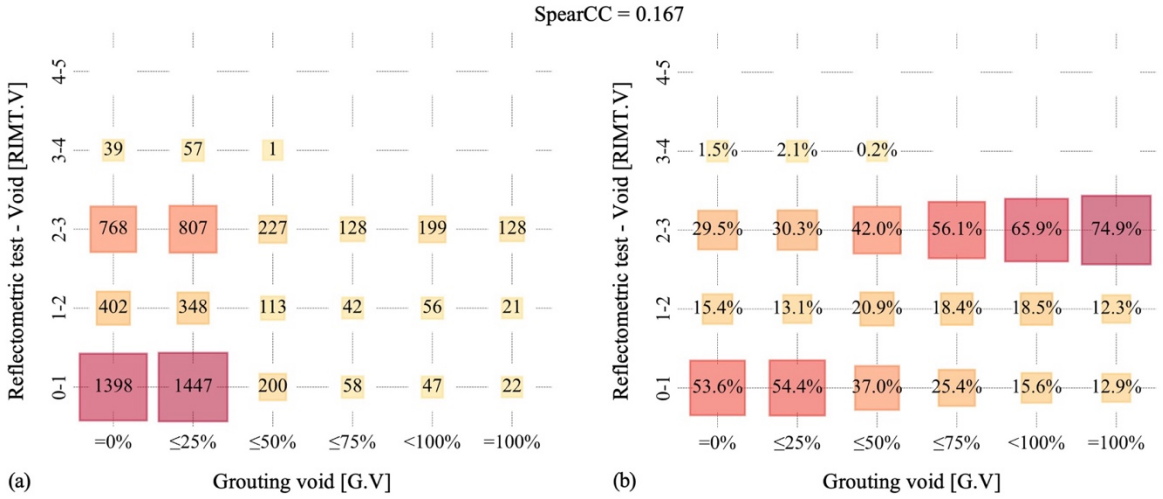

Figure 6.35 Comparison between RIMT.V and G.V. (a) Contingency table; (b) conditional probability table. In the upside the Spearman's correlation coefficient obtained.

6.6.2 Condition state of the steel wires

This subsection focuses on the NDT outcomes with codes GPR.C and RIMT.C for the defects in the steel wires, specifically, the corrosion (S.C). Figure 6.36 provides a qualitative comparison between these NDT outcomes and the defects observed in the steel cables during the dissection of cables C8, C9, and C10 of girder T1. The colour map used in the comparison ranges from green to red, representing the severity class of the defect, from no defect to severe defect, respectively.

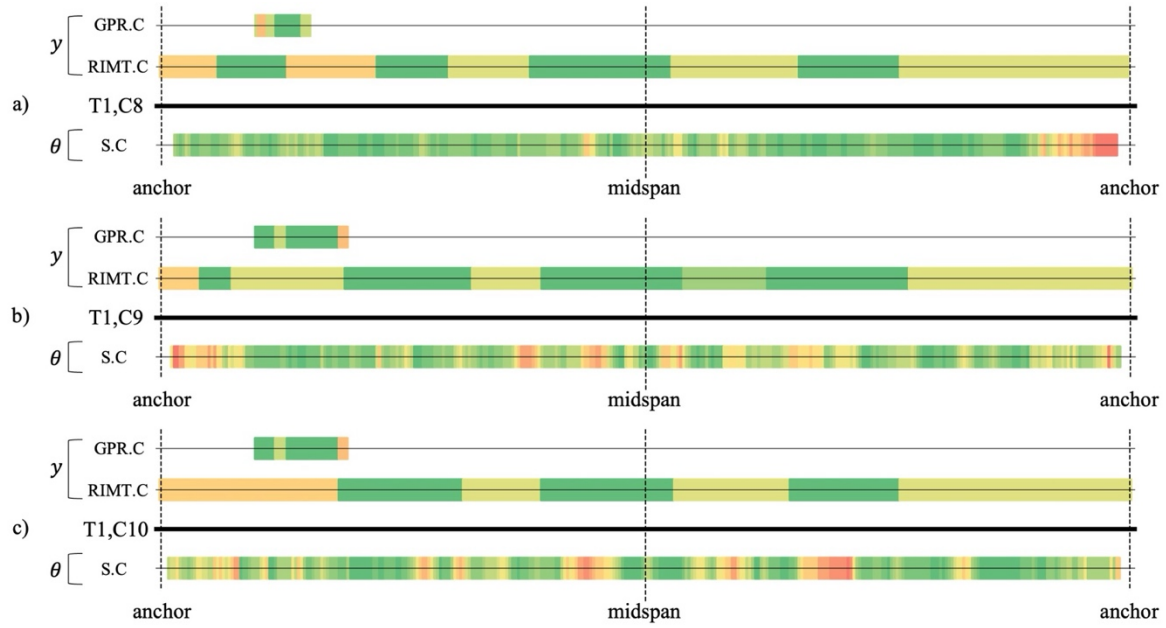

Figure 6.36 Comparison between NDTs outputs and the actual intensity of corrosion observed in the steel wires.

The results of the correlation analysis suggests no clear correlation between the steel wires corrosion (S.C) defect and the GPR outcomes (GPR.C), with a Spearman's correlation coefficient of 0.035 (Figure 6.37) which indicates no correlation. The contingency table and conditional probability table elements are mostly concentrated in the first raw.

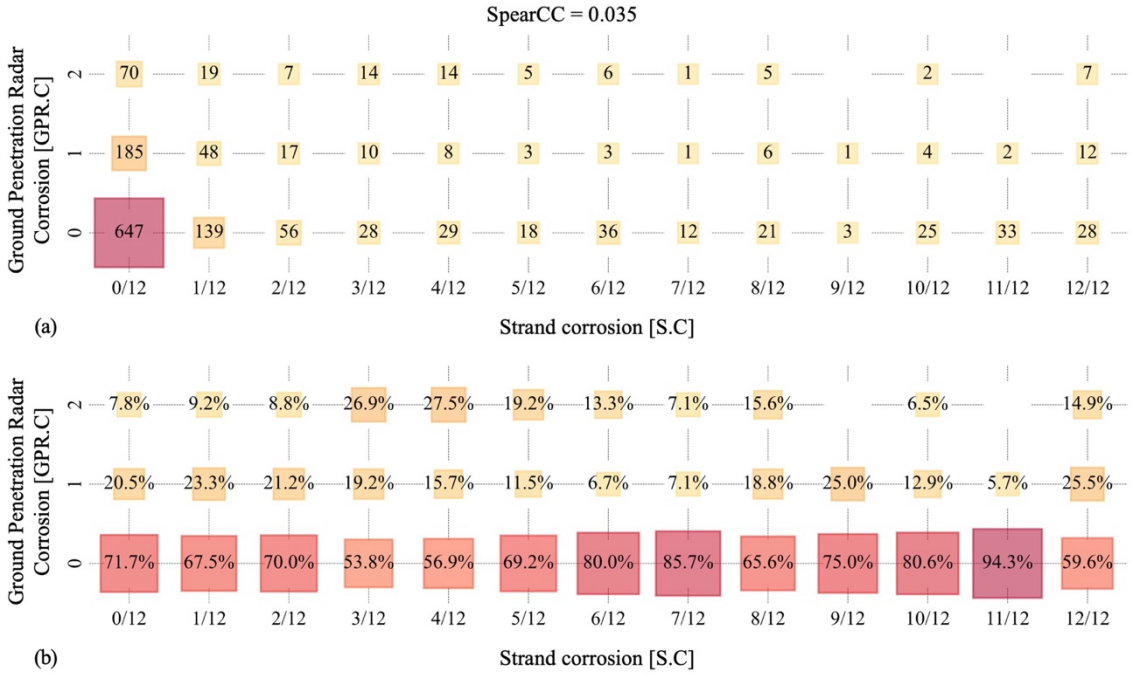

Figure 6.37 Comparison between GPR.C and S.C.

(a) Contingency table; (b) conditional probability table. In the upside the Spearman's correlation coefficient obtained.

As discussed in Subsection 6.4.1, considering that similar to DR, also for the GPR, was confined the correlation analysis between the GPR outcomes (GPR.C) with the actual condition state of the steel wires corrosion (S.C) only to the cables anchored at the slab (cables 11, 12, 13 and 14), which are single. Nevertheless, a similar value of Spearman's correlation coefficient was obtained, equal to 0.006. Figure 6.38 illustrates the corresponding contingency and conditional probability tables.

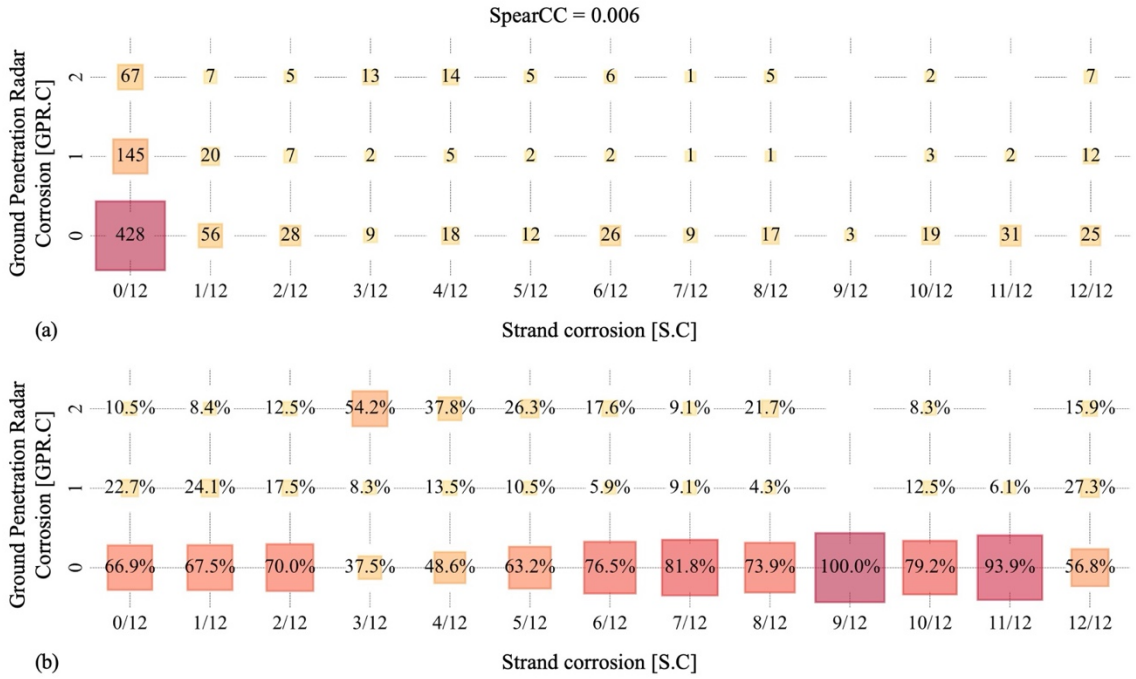

Figure 6.38 Comparison between GPR.C and S.C limited at the cables anchored at the slab.

(a) Contingency table; (b) conditional probability table. In the upside the Spearman's correlation coefficient obtained.

A final comparison is reported between the reflectometric outcomes regarding the investigation of the cables corrosion (RIMT.C) and the actual condition state of corrosion of the steel wires (S.C). In this case, a Spearman's correlation coefficient value of 0.177 is obtained, which suggests a poor correlation. Figure 6.39 shows that the contingency table and the conditional probability table elements are randomly distributed.

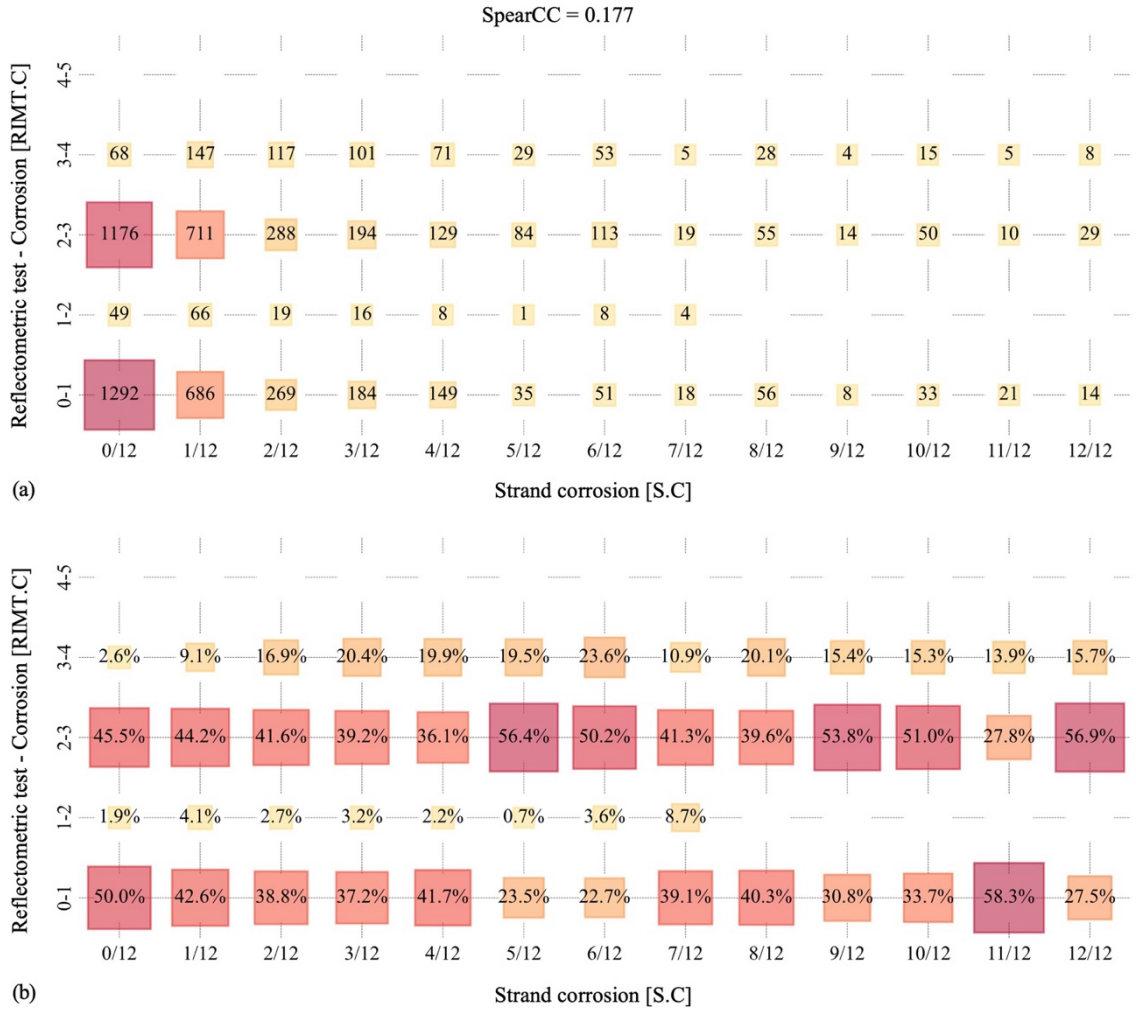

Figure 6.39 Comparison between RIMT.C and S.C.

(a) Contingency table; (b) conditional probability table. In the upside the Spearman's correlation coefficient obtained.

6.6.3 Summary

This subsection summarises the Spearman's correlation coefficient values obtained from the correlation analysis between all the defects mapped during the dissection of the prestressing system and the results of NDTs. Table 6.2 reports the values correlated with colours that describe the correlation strength between the two variables.

As emphasized in subsections 6.6.1, it is essential to note that only the DR outcomes exhibit a moderate correlation with the actual condition of one component of the mapped prestressing system, the injected grout. Indeed, DR is the most successful test in identifying areas with significant grade of grout fracturing (G.F) and percentage of grouting void (G.V). By limiting the reference sample for correlation analysis exclusively to the cables anchored at the slab, higher correlation is obtained. This is because these cables are singular and not prone to

errors that may arise when assigning the same defect intensity classes to cables that are horizontally overlapped along the girders. In contrast, RIMT results appear not particularly correlated to grouting void (G.V) or increased of grout fracturing (G.F).

As denoted in subsections 6.6.2, instead, neither reflectometric test (RIMT.C) nor radar test (GPR.C) seems to be particularly effective in identifying steel wires corrosion (S.C). Indeed, contrary to expectations, the reflectometric (RIMT.C) outcomes exhibit a higher Spearman's correlation coefficient value with the grouting void (G.V) defect than with steel wires corrosion (S.C) defect.

	D.C	D.A	D.P	G.F	G.V	S.C	S.R	S.I
DR.V	0.000 -0.037*	0.151 0.108*	0.150 0.107*	0.415 0.431*	0.474 0.542*	0.162 0.174*	-0.026 -0.074*	0.056 0.073*
GPR.C	0.076 0.085*	0.099 0.121*	0.129 0.149*	0.013 0.019*	0.049 0.028*	0.035 0.006*	0.028 0.032*	0.071 -0.081*
RIMT.V	-0.049	0.058	0.041	0.101	0.167	0.154	0.032	0.009
RIMT.C	-0.095	0.099	0.080	0.170	0.238	0.177	0.018	0.009

Table 6.2 Spearman's Correlation Coefficient. (*) denoted SpearCC with confined reference sample at the cable anchored at the slab.

To ensure independence from the metric chosen, Table 6.3 presents a comparison of the correlation measures reported in subsection 6.3.4 with the defects investigated by the NDTs analysed. In particular, the Pearson's correlation coefficient (PearsCC), the Polychoric correlation coefficient (PolyCC), the Goodman-Kruskal Gamma (GKγ), and the Stuart-Kendall Tau-c (SKτ) are considered.

It can be observed in Table 6.3 that the metrics generally have similar values. Similar values of the SpearCCt and the PearsCC indicate linear correlation between the variables. In the correlation analysis between the radiographic and radar outcomes with the steel wires interruptions (S.I) defect, due to the extreme non-uniformity of elements in the contingency tables, it was impossible to obtain the PolyCC and the GKγ correlation coefficient values.

		D.C	D.A	D.P	G.F	G.V	S.C	S.R	S.I
DR.V	SpearCC	0.000	0.151	0.150	0.415	0.474	0.162	-0.026	0.056
	PearsCC	-0.037	0.040	-0.010	0.414	0.452	0.129	-0.051	0.051
	PolyCC	-0.014	0.148	0.144	0.484	0.565	0.164	-0.072	-
	GKγ	0.001	0.203	0.224	0.481	0.570	0.180	-0.083	-
	SKτ	0.001	0.131	0.124	0.384	0.431	0.146	-0.011	0.005
GPR.C	SpearCC	0.076	0.099	0.129	0.013	0.049	0.035	0.028	0.071
	PearsCC	0.100	0.144	0.159	0.059	0.113	0.013	0.026	0.088
	PolyCC	0.126	0.184	0.235	0.044	0.096	0.059	0.071	-
	GKγ	0.101	0.185	0.269	0.017	0.080	0.059	0.174	-
	SKτ	0.059	0.062	0.071	0.009	0.035	0.026	0.006	0.005
RIMT.V	SpearCC	-0.049	0.058	0.041	0.101	0.167	0.154	0.032	0.009
	PearsCC	-0.057	0.058	0.032	0.109	0.216	0.114	0.052	0.007
	PolyCC	-0.056	0.070	0.047	0.116	0.216	0.168	0.099	0.069
	GKγ	-0.051	0.083	0.068	0.129	0.228	0.189	0.160	0.194
	SKτ	-0.040	0.041	0.027	0.079	0.127	0.120	0.007	0.001
RIMT.C	SpearCC	-0.095	0.099	0.080	0.170	0.238	0.177	0.018	0.009
	PearsCC	-0.098	0.090	0.054	0.174	0.258	0.141	0.040	0.008
	PolyCC	-0.104	0.146	0.116	0.213	0.315	0.225	0.063	0.059
	GKγ	-0.100	0.142	0.133	0.220	0.329	0.220	0.099	0.211
	SKτ	-0.075	0.070	0.051	0.131	0.180	0.138	0.004	0.001

Table 6.3 Metrics comparison

6.7 Discussion of the results

The comparison between Non-Destructive Testing (NDT) outcomes and the actual state condition of the PT system sheds light on how effective different methods are for evaluating prestressing systems. In this study, we dive into Digital Radiography (DR), Ground Penetration Radar (GPR), and Reflectometric Impulse Measurement Test (RIMT), focusing on their correlations with grout fracturing (G.F), grouting injection voids (G.V), and steel wire corrosion (S.C).

Spearman's correlation coefficients (SpearCC) reveal moderate connections between radiography outcomes, DR.V, and both grout fracturing, G.F, (SpearCC = 0.415) and grouting voids, G.V, (SpearCC = 0.474), respectively. Supported by contingency and conditional probability tables, these correlations highlight the moderate relationship between DR outcomes and the actual condition of injected grout. When explicitly examining single

cables anchored at the slab (cables 11, 12, 13, and 14), the correlation between radiography outcomes, DR.V, and grouting voids defects, G.V, increases, reaching a Spearman's correlation coefficient equal to 0.542. This emphasizes how the cable configurations impact the defect assessment.

Conversely, the correlation analysis between radar outcomes, GPR.C, and steel wire corrosion, S.C, shows poor Spearman's correlation coefficients (SpearCC = 0.035), even when focusing on cables anchored at the slab (SpearCC = 0.006). This evidence suggests that GPR outcomes cannot predict accurately the state of steel wire corrosion. Similarly, RIMT outcomes related to injection defects (RIMT.V) display low Spearman's correlation coefficients with grout fracturing, G.F, (SpearCC = 0.101) and grouting voids, G.V, (SpearCC = 0. 167), indicating a poor capability of RIMT to predict the cables injection defects. This trend persists for RIMT outcomes concerning cable corrosion (RIMT.C) and actual steel wire corrosion defect state ,S.C, (SpearCC = 0. 177).

The comparison of the correlation metrics reported in Table 6.3 assures consistency in results regardless of the chosen correlation metric. Furthermore, the alignment between Spearman and Pearson correlation coefficients suggests a probable linear correlation between variables.

To sum up, this study thoroughly evaluates three primary NDT methods for assessing prestressing systems embedded in a PT structure. While DR shows promising correlations with grout conditions, RIMT and GPR face limitations in predicting grout conditions and steel cable corrosion. These findings stress the importance of a comprehensive approach that meticulously considers cable configurations for precise and reliable evaluations of prestressing systems. Such a holistic understanding has the potential to significantly impact maintenance and reliability planning for post-tensioned concrete bridge decks.

6.8 Conclusions

This study has evaluated the metrological effectiveness of Digital Radiography (DR), Ground Penetration Radar (GPR), and Reflectometric Impulse Measurement Test (RIMT) as non-destructive testing (NDT) methods for detecting defects in the prestressing system of post-tensioned (PT) bridges. This study has been carried out by quantifying the correlation between the outcomes of these NDTs and the level of defects observed during the autopsy of the prestressing system of a decommissioned bridge in Italy, the Alveo Vecchio viaduct. Contingency tables, conditional probability tables, and various correlation coefficients have been employed to determine the correlation between the NDT results and the actual defects in

the prestressing system. Based on the analysis of the results of the study, the following conclusions can be drawn:

- With regards to the condition state of the injected grout, the DR outcomes showed a weak to moderate correlation with the grade of grout fracturing and a moderate correlation with the percentage of grouting void. On the other hand, the correlation between the GPR outcomes and the condition state of the injected grout was poor. Similarly, the RIMT outcomes exhibited a poor to weak correlation. Overall, the DR method proved to be the most effective in identifying areas with significant grouting void.
- With regards to the condition state of the steel threads, both the GPR and RIMT methods showed no clear correlation with the defect of steel threads corrosion. The correlation coefficients indicated a poor to weak correlation for both methods. Therefore, neither the GPR nor RIMT methods were suitable for identifying corrosion in steel cables. On the other hand, DR does not provide information about the steel threads corrosion.

In summary, this study has highlighted both the few strengths and many limitations of various non-destructive testing (NDT) methods in assessing the condition of prestressing system components. The DR method demonstrated superior performance in detecting grouting voids, while the GPR and RIMT methods showed limited effectiveness. Furthermore, none of the methods were effective in identifying corrosion in steel wires. These findings can inform future inspection and maintenance strategies for prestressing systems, helping to ensure their structural integrity and longevity.

Additionally, the results of the NDTs analyzed in this work could be potentially useful for updating numerical models to predict the behavior of structures with characteristics similar to the Alveo Vecchio viaduct. However, the findings indicate that such NDTs are characterized by significant uncertainty. Therefore, if the goal is to update the parameters of numerical models, it is more appropriate to use different investigation techniques. Destructive tests, for instance, provide direct and reliable data, allowing for accurately detecting corrosion in the prestressing system within concrete elements.

7 CONCLUSIONS

Based on extensive research conducted on the Alveo Vecchio viaduct, a decommissioned prestressed concrete bridge representing a significant portion of Italian highway bridges, several crucial conclusions emerge regarding the effectiveness of various assessment and monitoring diagnostic tests.

Regarding load testing and structural modelling, it becomes evident that load testing, particularly up to the design traffic load, offers invaluable insights into a bridge's structural health. These tests reveal crucial parameters such as stiffness and first-crack load. Moreover, the research demonstrates the significant influence of parameters like concrete's elastic modulus and prestressing cables' residual stress on structural response. Analytical and Finite Element Models (FEM), when supplemented with Non-Destructive Test (NDT) techniques of material specimens, prove capable of predicting structural behaviour with reasonable accuracy.

Regarding the Acoustic Emission (AE) technique for monitoring post-tensioned concrete structures, it emerges as a potent tool providing real-time information on bridge cracking and damage. AE effectively distinguishes between cracked and uncracked conditions and detects the opening of the first crack. However, further research is necessary to classify different types of damage based on signal analysis.

Concerning NDT methods, Digital Radiography (DR) effectively identifies significant grouting voids in the prestressing system, offering valuable insights into potential structural weaknesses. However, Ground Penetration Radar (GPR) and Reflectometric Impulse Measurement Test (RIMT) exhibit limitations in detecting defects, particularly steel wires corrosion. None of these methods comprehensively assess steel wires corrosion, highlighting the need for improved techniques in this area.

Given the above conclusions of the extensive experimental activity, it is evident that integrating multiple assessment techniques is crucial to accurately evaluate the condition of prestressed concrete bridges. Load testing, structural modelling, and AE monitoring provide comprehensive insights into bridge behaviour under load, allowing for informed decision-making in maintenance and repair efforts.

Recommendations stemming from this research include the preference for DR in assessing grouting voids due to their effectiveness and the need for further research to enhance the effectiveness of NDT methods, particularly in detecting steel wires corrosion. Future

inspection and maintenance strategies should adopt a holistic approach, combining load testing, AE monitoring, and DR to ensure the safety and longevity of ageing bridge assets in transportation networks.

In conclusion, the research conducted at the Alveo Vecchio viaduct underscores the importance of employing advanced monitoring technologies and refining analytical models to assess post-tensioned concrete bridges' condition. By leveraging these tools, infrastructure managers can make informed decisions to safeguard the integrity and longevity of critical transportation infrastructure.

8 REFERENCES

[1]«Asset Management Transformation Project Post-Tensioned Non-Destructive Testing and Monitoring Techniques - Assessment of Available Methodologies». Highways England, 10 ottobre 2020. [Online]. Available on: https://mininginstitute.org.uk/wp-content/uploads/2021/02/5195381-ATK-ZZ-DO-S-0001-PT-Structures-Literature-Review.pdf

[2]B. Täljsten, B. Paulsson, e L. Elfgren, «Prestressed concrete bridges: condition assessment and future challenges: a state-of-art report», 2019.

[3]Z.-Q. He, Y. Li, T. Xu, Z. Liu, e Z. J. Ma, «Crack-based serviceability assessment of post-tensioned segmental concrete box-girder bridges», *Structures*, vol. 30, pp. 1097–1108, apr. 2021, doi: 10.1016/j.istruc.2021.01.062.

[4]G. Miluccio, D. Losanno, F. Parisi, e E. Cosenza, «Traffic-load fragility models for prestressed concrete girder decks of existing Italian highway bridges», *Engineering Structures*, vol. 249, p. 113367, dic. 2021, doi: 10.1016/j.engstruct.2021.113367.

[5]L. AASHTO, «American association of state highway and transportation officials LRFD bridge design specifications», 2017.

[6]H. Liu, J. Li, J. Zhang, e D. Pang, «Decision Analysis of a Reinforcement Scheme for In-Service Prestressed Concrete Box Girder Bridges Based on AHP and Evaluation of the Reinforcement Effect», *Buildings*, vol. 12, fasc. 10, p. 1771, ott. 2022, doi: 10.3390/buildings12101771.

[7]«2021 Report Card for America's Infrastructure». ASCE American Society of Civil Engineers, 2021. [Online]. Disponibile su: https://infrastructurereportcard.org/

[8]«White paper on land, infrastructure, transport, and tourism in Japan in 2019». Ministry of Land, Infrastructure, Transport and Tourism of Japan, 2019. [Online]. Available on: https://www.mlit.go.jp/en/statistics/white-paper-mlit-2019.html.

[9]D. Tonelli, F. Rossi, F. Brighenti, A. Verzobio, A. Bonelli, e D. Zonta, «Prestressed concrete bridge tested to failure: the Alveo Vecchio viaduct case study», *J Civil Struct Health Monit*, ott. 2022, doi: 10.1007/s13349-022-00633-w.

[10]M. Bonopera, K.-C. Chang, e Z.-K. Lee, «State-of-the-Art Review on Determining Prestress Losses in Prestressed Concrete Girders», *Applied Sciences*, vol. 10, fasc. 20, p. 7257, ott. 2020, doi: 10.3390/app10207257.

[11]«Linee Guida Per La Classificazione E Gestione Del Rischio, La Valutazione Della Sicurezza Ed Il Monitoraggio Dei Ponti Esistenti». Ministero delle Infrastrutture e dei Trasporti; Consiglio Superiore dei Lavori Pubblici, 2020.

[12]D. Bolognani *et al.*, «IWSHM 2017: Quantifying the benefit of structural health monitoring: what if the manager is not the owner?», *Structural Health Monitoring*, vol. 17, fasc. 6, pp. 1393–1409, nov. 2018, doi: 10.1177/1475921718794506.

[13]S. Alampalli *et al.*, «Bridge load testing: State-of-the-practice», *Journal of Bridge Engineering*, vol. 26, fasc. 3, p. 03120002, 2021.

[14]E. O. Lantsoght, C. van der Veen, A. de Boer, e D. A. Hordijk, «State-of-the-art on load testing of concrete bridges», *Engineering Structures*, vol. 150, pp. 231–241, 2017.

[15]N. Bagge, M. Plos, e C. Popescu, «A multi-level strategy for successively improved structural analysis of existing concrete bridges: Examination using a prestressed concrete

bridge tested to failure», *Structure and Infrastructure Engineering*, vol. 15, fasc. 1, pp. 27–53, 2019.

[16]M. A. Zanini, F. Faleschini, e C. Pellegrino, «New trends in assessing the prestress loss in post-tensioned concrete bridges», *Front. Built Environ.*, vol. 8, p. 956066, nov. 2022, doi: 10.3389/fbuil.2022.956066.

[17]L. Deng, W. Wang, e Y. Yu, «State-of-the-art review on the causes and mechanisms of bridge collapse», *Journal of Performance of Constructed Facilities*, vol. 30, fasc. 2, p. 04015005, 2016.

[18]D. M. Frangopol e M. Liu, «Maintenance and management of civil infrastructure based on condition, safety, optimization, and life-cycle cost∗», *Structure and Infrastructure Engineering*, vol. 3, fasc. 1, pp. 29–41, mar. 2007, doi: 10.1080/15732470500253164.

[19]G. M. Calvi *et al.*, «Once upon a Time in Italy: The Tale of the Morandi Bridge», *Structural Engineering International*, vol. 29, fasc. 2, pp. 198–217, apr. 2019, doi: 10.1080/10168664.2018.1558033.

[20]P. Clemente, «Monitoring and evaluation of bridges: lessons from the Polcevera Viaduct collapse in Italy», *J Civil Struct Health Monit*, vol. 10, fasc. 2, pp. 177–182, apr. 2020, doi: 10.1007/s13349-020-00384-6.

[21]E. Farneti *et al.*, «A method for structural monitoring of multispan bridges using satellite InSAR data with uncertainty quantification and its pre-collapse application to the Albiano-Magra Bridge in Italy», *Structural Health Monitoring*, vol. 22, fasc. 1, pp. 353–371, gen. 2023, doi: 10.1177/14759217221083609.

[22]D. Zonta, R. Zandonini, e F. Bortot, «A reliability-based bridge management concept», *Structures & Infrastructure Engineering*, vol. 3, fasc. 3, pp. 215–235, 2007.

[23]«Modalità operative per la gestione del sistema MA.GG.04 ver.1». Provincia Autonoma di Trento (PAT), 18 aprile 2013. [Online]. Available on: http://www.bms.provincia.tn.it/bms/wp-content/uploads/2012/09/MAGG04-1.pdf

[24]«Guide for Commonly Recognized (CoRe) Structural Elements»,. American Association of State Highway and Transportation Officials (AASHTO), 1997.

[25]«Sistema BMS DOMUS». Rete Ferroviaria Italiana (RFI). [Online]. Available on: https://www.rfi.it/it/Sicurezza-e-tecnologie/Infrastruttura-resiliente/Sicurezza-e-diagnostica-opere-d-arte.html

[26]«Manutenzione programmata delle opere d'arte stradali - Catalogo dei difetti». SPEA - Autostrade per l'Italia (ASPI), 2015.

[27]Z. Mirzaei, B. T. Adey, L. Klatter, e J. S. Kong, «Overview of existing bridge management systems-report by the IABMAS Bridge Management Committee», presentato al 6th International Conference on Bridge Maintenance, Safety and Management (IABMAS 2012), International Association for Bridge Maintenance And Safety (IABMAS), 2012.

[28]S. Hurlebaus *et al.*, *Inspection Guidelines for Bridge Post-Tensioning and Stay Cable Systems Using NDE Methods*. Washington, D.C.: Transportation Research Board, 2017, p. 24779. doi: 10.17226/24779.

[29]«CS 465 Management of post-tensioned concrete bridges - Highway Structures & Bridges Inspection & Assessment». Standards for Highways, aprile 2020. [Online]. Available on: https://www.standardsforhighways.co.uk/search/3eab3df6-b87b-412d-ac0b-87a1ea1c325c

[30]F. C. Lea e C. Middleton, *Reliability of visual inspection of highway bridges*. Department of Engineering, University of Cambridge Cambridge, UK, 2002.

[31]M. Moore, *Reliability of visual inspection for highway bridges*. Wiss, Janney, Elstner Associates, 2000.

[32]D. M. Clarke, «The human face of risk», *Nuclear Engineer*, vol. 39, fasc. 4, pp. 115–19, 1998.

[33]D. Balageas, C.-P. Fritzen, e A. Güemes, *Structural health monitoring*, vol. 90. John Wiley & Sons, 2010.

[34]M. Meo, «Acoustic emission sensors for assessing and monitoring civil infrastructures», in *Sensor technologies for civil infrastructures*, Elsevier, 2022, pp. 149–167.

[35]M. A. Hamstad e J. D. McColskey, «Detectability of slow crack growth in bridge seels by acoustic emission», 1998.

[36]T. Morton, R. Harrington, e J. Bjeletich, «Acoustic emissions of fatigue crack growth», *Engineering fracture mechanics*, vol. 5, fasc. 3, pp. 691–697, 1973.

[37]K. Holford, A. Davies, e A. Sammarco, «Analysis of Fatigue Crack Growth in Structural Steels by Classification of Acoustic Emission Signals», presented to Proceedings of the Engineering Systems Design and Analysis Congress, London, UK, 1994, pp. 4–7.

[38]X. Zhang e B. Li, «Damage characteristics and assessment of corroded RC beam-column joint under cyclic loading based on acoustic emission monitoring», *Engineering Structures*, vol. 205, p. 110090, 2020.

[39]S. Yuyama e M. Ohtsu, «Acoustic emission evaluation in concrete», *Acoustic Emission-Beyond the Millennium; Kishi, T., Ohtsu, M., Yuyama, S., Eds*, pp. 187–213, 2000.

[40]D.-J. Yoon, W. J. Weiss, e S. P. Shah, «Assessing damage in corroded reinforced concrete using acoustic emission», *Journal of engineering mechanics*, vol. 126, fasc. 3, pp. 273–283, 2000.

[41]A. Ebrahimkhanlou, J. Choi, T. D. Hrynyk, S. Salamone, e O. Bayrak, «Acoustic emission monitoring of containment structures during post-tensioning», *Engineering structures*, vol. 209, p. 109930, 2020.

[42]R. Goldaran, A. Turer, M. Kouhdaragh, e K. Ozlutas, «Identification of corrosion in a prestressed concrete pipe utilizing acoustic emission technique», *Construction and Building Materials*, vol. 242, p. 118053, 2020.

[43]Y. Wu, S. Li, D. Wang, e G. Zhao, «Damage monitoring of masonry structure under in-situ uniaxial compression test using acoustic emission parameters», *Construction and Building Materials*, vol. 215, pp. 812–822, 2019.

[44]A. Pollock e B. Smith, «Stress-wave-emission monitoring of a military bridge», *Non-destructive testing*, vol. 5, fasc. 6, pp. 348–353, 1972.

[45]A. Nair e C. Cai, «Acoustic emission monitoring of bridges: Review and case studies», *Engineering structures*, vol. 32, fasc. 6, pp. 1704–1714, 2010.

[46]L. Golaski, P. Gebski, e K. Ono, «Diagnostics of reinforced concrete bridges by acoustic emission», *Journal of acoustic emission*, vol. 20, fasc. 1, pp. 83–98, 2002.

[47]R. Anay, A. Lane, D. V. Jáuregui, B. D. Weldon, V. Soltangharaei, e P. Ziehl, «On-site acoustic-emission monitoring for a prestressed concrete BT-54 AASHTO girder bridge», *Journal of Performance of Constructed Facilities*, vol. 34, fasc. 3, p. 04020034, 2020.

[48]S. Chataigner *et al.*, «Acoustic monitoring of a prestressed concrete beam reinforced by adhesively bonded composite», presentato al ICCRRR 2018, International Conference on Concrete Repair Rehabilitation and Retrofitting, EDP Sciences, 2019, p. 8p.

[49]G. Ma e Q. Du, «Structural health evaluation of the prestressed concrete using advanced acoustic emission (AE) parameters», *Construction and Building Materials*, vol. 250, p. 118860, 2020.

[50]S. Yuyama, K. Yokoyama, K. Niitani, M. Ohtsu, e T. Uomoto, «Detection and evaluation of failures in high-strength tendon of prestressed concrete bridges by acoustic emission», *Construction and building materials*, vol. 21, fasc. 3, pp. 491–500, 2007.

[51]S. Fricker e T. Vogel, «Site installation and testing of a continuous acoustic monitoring», *Construction and Building Materials*, vol. 21, fasc. 3, pp. 501–510, 2007.

[52]W. Vélez, F. Matta, e P. Ziehl, «Acoustic emission monitoring of early corrosion in prestressed concrete piles», *Structural Control and Health Monitoring*, vol. 22, fasc. 5, pp. 873–887, 2015.

[53]G. I. Zarate Garnica, E. O. L. Lantsoght, e Y. Yang, «Monitoring structural responses during load testing of reinforced concrete bridges: A review», *Structure and Infrastructure Engineering*, vol. 18, fasc. 10–11, pp. 1558–1580, 2022.

[54]W. Merkle e J. J. Myers, «Use of the total station for serviceability monitoring of bridges with limited access in Missouri, USA», *University of MissouriRolla*, 2004.

[55]E. Lachat, T. Landes, e P. Grussenmeyer, «Investigation of a combined surveying and scanning device: the trimble SX10 scanning total station», *Sensors*, vol. 17, fasc. 4, p. 730, 2017.

[56]P. S. Halding, J. W. Schmidt, T. W. Jensen, e A. Henriksen, «Structural response of full-scale concrete bridges subjected to high load magnitudes», presented to 4th Conference on Smart Monitoring, Assessment and Rehabilitation of Civil Structures, 2017.

[57]W. J. Merkle e J. Myers, «Load testing and load distribution response of Missouri bridges retrofitted with various frp systems using a non-contact optical measurement system», presentato al Transportation Research Board, 85th Annual Meeting January 22nd-26th, 2006.

[58]D. Palazzo, R. Friedmann, C. Nadal, F. Santos, L. Veiga, e P. Faggion, «Dynamic monitoring of structures using a robotic total station», presented to Proceedings of the Shaping the Change XXIII FIG Congress, Munich, Germany, 2006.

[59]M. Ettouney e S. Alampalli, *Infrastructure health in civil engineering*. CRC press Boca Raton, FL, 2012.

[60]«Piezotronics tech support documents». 2011. [Online]. Available on : http://www. pcb.com/techsupport/tech_indaccel

[61]W.-H. Hu, D.-H. Tang, J. Teng, S. Said, e Rolf. G. Rohrmann, «Structural Health Monitoring of a Prestressed Concrete Bridge Based on Statistical Pattern Recognition of Continuous Dynamic Measurements Over 14 Years», *Sensors*, vol. 18, fasc. 12, p. 4117, nov. 2018, doi: 10.3390/s18124117.

[62]S. Quqa, P. F. Giordano, M. P. Limongelli, L. Landi, e P. P. Diotallevi, «Clump interpolation error for the identification of damage using decentralized sensor networks», *Smart Struct. Syst*, vol. 27, fasc. 2, pp. 351–363, 2021.

[63]V. Quaglini, C. Pettorruso, S. Cattaneo, e D. Rossi, «Assessment of bridge Post-Tensioning systems using non-destructive (ND) inspection methods», *ce papers*, vol. 6,

fasc. 5, pp. 9–17, set. 2023, doi: 10.1002/cepa.2065.

[64]M. Abouhamad, T. Dawood, A. Jabri, M. Alsharqawi, e T. Zayed, «Corrosiveness mapping of bridge decks using image-based analysis of GPR data», *Automation in Construction*, vol. 80, pp. 104–117, 2017.

[65]A. Tarussov, M. Vandry, e A. De La Haza, «Condition assessment of concrete structures using a new analysis method: Ground-penetrating radar computer-assisted visual interpretation», *Construction and Building Materials*, vol. 38, pp. 1246–1254, 2013.

[66]A. Ciolko e H. Tabatabai, «Nondestructive methods for condition evaluation of prestressing steel strands in concrete bridges», *Final Report, NCHRP Project*, pp. 10–53, 1999.

[67]A. Rahman e G. Pernica, «Effectiveness of an electromagnetic wave propagation technique for the condition assessment of post-tensioned tendons—an evaluation report», *Canada Mortgage and Housing Corporation*, 1997.

[68]P. Matt, «Non-destructive evaluation and monitoring of post-tensioning tendons», *BULLETIN-FIB*, vol. 15, pp. 103–108, 2001.

[69]W. Liu, R. G. Hunsperger, M. J. Chajes, K. J. Folliard, e E. Kunz, «Corrosion detection of steel cables using time domain reflectometry», *Journal of Materials in Civil Engineering*, vol. 14, fasc. 3, pp. 217–223, 2002.

[70]M. Chajes, R. Hunsperger, W. Liu, J. Li, e E. Kunz, «Time domain reflectometry for void detection in grouted posttensioned bridges», *Transportation research record*, vol. 1845, fasc. 1, pp. 148–152, 2003.

[71]E. Baran, C. K. Shield, e C. E. French, «A comparison of methods for experimentally determining prestress losses in pretensioned prestressed concrete girders», *Special Publication*, vol. 231, pp. 161–180, 2005.

[72]H. Abdel-Jaber e B. Glisic, «Monitoring of prestressing forces in prestressed concrete structures—An overview», *Struct Control Health Monit*, vol. 26, fasc. 8, ago. 2019, doi: 10.1002/stc.2374.

[73]C. Czaderski e E. Fh, «Determining the Remaining Tendon Force of a Large- Scale, 38-Year-Old Prestressed Concrete Bridge Girder».

[74]C. Trautner, M. McGinnis, e S. Pessiki, «Application of the Incremental Core-Drilling Method to Determine In-Situ Stresses in Concrete.», *ACI Materials Journal*, vol. 108, fasc. 3, 2011.

[75]M. J. McGinnis e S. Pessiki, «Experimental study of the core-drilling method for evaluating in situ stresses in concrete structures», *Journal of Materials in Civil Engineering*, vol. 28, fasc. 2, p. 04015099, 2016.

[76]S. K. U. Rehman, Z. Ibrahim, S. A. Memon, e M. Jameel, «Nondestructive test methods for concrete bridges: A review», *Construction and building materials*, vol. 107, pp. 58–86, 2016.

[77]R. D. Innocenzi, G. Pigliapoco, S. Carbonari, F. Gara, e L. Dezi, «Damage Detection of Post-tensioned Cables in Existing Bridges with Digital Radiography», in *Proceedings of the 1st Conference of the European Association on Quality Control of Bridges and Structures*, vol. 200, C. Pellegrino, F. Faleschini, M. A. Zanini, J. C. Matos, J. R. Casas, e A. Strauss, A c. di, in Lecture Notes in Civil Engineering, vol. 200. , Cham: Springer International Publishing, 2022, pp. 662–669. doi: 10.1007/978-3-030-91877-4_75.

[78]S. K. Verma, S. S. Bhadauria, e S. Akhtar, «Review of Nondestructive Testing Methods for Condition Monitoring of Concrete Structures», *Journal of Construction Engineering*, vol. 2013, pp. 1–11, apr. 2013, doi: 10.1155/2013/834572.

[79]M. K. Lim e H. Cao, «Combining multiple NDT methods to improve testing effectiveness», *Construction and Building Materials*, vol. 38, pp. 1310–1315, gen. 2013, doi: 10.1016/j.conbuildmat.2011.01.011.

[80]S. Iyer, A. J. Schokker, e S. K. Sinha, «Ultrasonic imaging–A novel way to investigate corrosion status in post-tensioned concrete members».

[81]M. I. Haith, «Radiographic imaging of subsea pipelines», 2016.

[82]W. Silva, R. Lopes, U. Zscherpel, D. Meinel, e U. Ewert, «X-ray imaging techniques for inspection of composite pipelines», *Micron*, vol. 145, p. 103033, 2021.

[83]M. Beck, J. Goebbels, A. Burkert, B. Isecke, e R. Bäßler, «Monitoring of corrosion processes in chloride contaminated mortar by electrochemical measurements and X-ray tomography», *Materials and corrosion*, vol. 61, fasc. 6, pp. 475–479, 2010.

[84]S. Lim, M. Akiyama, D. M. Frangopol, e H. Jiang, «Experimental investigation of the spatial variability of the steel weight loss and corrosion cracking of reinforced concrete members: novel X-ray and digital image processing techniques», in *Structures and Infrastructure Systems*, Routledge, 2019, pp. 199–215.

[85]T. Terzioglu, M. M. Karthik, S. Hurlebaus, e M. B. D. Hueste, «Nondestructive Evaluation of External Post-Tensioning Systems to Detect Grout Defects», *J. Struct. Eng.*, vol. 145, fasc. 1, p. 05018002, gen. 2019, doi: 10.1061/(ASCE)ST.1943-541X.0002229.

[86]H. England, «Asset Management Transformation Project», 2020.

[87]A. Mortellaro, G. Ievolella, F. Lombardo, C. Nuti, e I. Vanzi, «Relazione della Commissione Ispettiva Ministeriale crollo Viadotto Polcevera», *Ministero delle Infrastrutture e dei Trasporti: Roma, Italy*, 2018.

[88]J. T. Halsey e R. Miller, «Destructive Testing of Two Forty-Year-Old Prestressed Concrete Bridge Beams», *pcij*, vol. 41, fasc. 5, pp. 84–93, set. 1996, doi: 10.15554/pcij.09011996.84.93.

[89]N. Bagge, J. Nilimaa, e L. Elfgren, «In-situ methods to determine residual prestress forces in concrete bridges», *Engineering Structures*, vol. 135, pp. 41–52, mar. 2017, doi: 10.1016/j.engstruct.2016.12.059.

[90]C. V. Shenoy e G. C. Frantz, «Structural Tests of 27-Year-Oid Prestressed Concrete Bridge Beams», *pcij*, vol. 36, fasc. 6, pp. 80–90, set. 1991, doi: 10.15554/pcij.09011991.80.90.

[91]Y. Labia, M. S. Saiidi, e B. Douglas, «Full-scale testing and analysis of 20-year-old pretensioned concrete box girders», *Structural Journal*, vol. 94, fasc. 5, pp. 471–482, 1997.

[92]N. Bagge, C. Popescu, e L. Elfgren, «Failure tests on concrete bridges: Have we learnt the lessons?», *Structure and Infrastructure Engineering*, vol. 14, fasc. 3, pp. 292–319, 2018.

[93]C. S. Cai e M. Shahawy, «Predicted and measured performance of prestressed concrete bridges», *Journal of Bridge Engineering*, vol. 9, fasc. 1, pp. 4–13, 2004.

[94]J. Pressley, C. Candy, B. Walton, e J. G. Sanjayan, «Destructive load testing of bridge no. 1049: analyses, predictions and testing», presented to AUSTROADS BRIDGE CONFERENCE, 5TH, 2004, HOBART, TASMANIA, AUSTRALIA, 2004.

[95]E. G. Burdette e D. W. Goodpasture, «Test to failure of a prestressed concrete bridge», *Pci Journal*, p. 101, 1975.

[96]T. M. Pape e R. E. Melchers, «The effects of corrosion on 45-year-old pre-stressed concrete bridge beams», *Structure and Infrastructure Engineering*, vol. 7, fasc. 1–2, pp. 101–108, 2011.

[97]D. Zonta, B. Glisic, e S. Adriaenssens, «Value of information: impact of monitoring on decision-making: VALUE OF INFORMATION: IMPACT OF MONITORING ON DECISION-MAKING», *Struct. Control Health Monit.*, vol. 21, fasc. 7, pp. 1043–1056, lug. 2014, doi: 10.1002/stc.1631.

[98]D. Tonelli *et al.*, «Expected utility theory for monitoring-based decision support system», presentato al Proceedings of the 11th international workshop on structural health monitoring, 2017.

[99]E. B. Flynn e M. D. Todd, «A Bayesian approach to optimal sensor placement for structural health monitoring with application to active sensing», *Mechanical Systems and Signal Processing*, vol. 24, fasc. 4, pp. 891–903, 2010.

[100]E. B. Flynn e M. D. Todd, «Optimal placement of piezoelectric actuators and sensors for detecting damage in plate structures», *Journal of Intelligent Material Systems and Structures*, vol. 21, fasc. 3, pp. 265–274, 2010.

[101]E. B. Flynn, M. D. Todd, A. J. Croxford, B. W. Drinkwater, e P. D. Wilcox, «Enhanced detection through low-order stochastic modeling for guided-wave structural health monitoring», *Structural Health Monitoring*, vol. 11, fasc. 2, pp. 149–160, 2012.

[102]C. Cappello, D. Zonta, e B. Glisic, «Expected Utility Theory for Monitoring-Based Decision-Making», *Proc. IEEE*, vol. 104, fasc. 8, pp. 1647–1661, ago. 2016, doi: 10.1109/JPROC.2015.2511540.

[103]I. Zambon, A. Vidović, A. Strauss, e J. Matos, «Condition Prediction of Existing Concrete Bridges as a Combination of Visual Inspection and Analytical Models of Deterioration», *Applied Sciences*, vol. 9, fasc. 1, p. 148, gen. 2019, doi: 10.3390/app9010148.

[104]Y. Ma, L. Wang, J. Zhang, Y. Xiang, e Y. Liu, «Bridge remaining strength prediction integrated with Bayesian network and in situ load testing», *Journal of Bridge Engineering*, vol. 19, fasc. 10, p. 04014037, 2014.

[105]I. Mazzatura, J. R. Casas, W. Salvatore, e S. Caprili, «Reliability of ultrasonic tomography in detecting grouting defects in post-tensioned structures by PoD curves», *Engineering Structures*, vol. 302, p. 117352, mar. 2024, doi: 10.1016/j.engstruct.2023.117352.

[106]J. Von Neumann e O. Morgenstern, «Theory of games and economic behavior Princeton», *Princeton University Press*, vol. 1947, p. 1953, 1944.

[107]H. Raiffa e R. Schlaifer, «Applied statistical decision theory», 1961.

[108]G. Parmigiani e L. Inoue, *Decision theory: Principles and approaches*. John Wiley & Sons, 2009.

[109]«Relazione di Calcolo Viadotto Alveo Vecchio alla progr. 39 + 364.21, Opera N*14». SPEA, 1966.

[110]«UNI/TR 11634:2016 Guidelines for structural health monitoring». Italian National Unification - UNI, Rome., 2016.

[111]«Decreto-Legge 28 settembre 2018, n.109 , .» Italian Govenment, 2018.

[112]«Codice della strada». Italian Ministry of Infrastructure and Transport, 2021. [Online]. Disponibile su: https://www.aci.it/i-servizi/normative/codice-della-strada.html

[113]M. Lehman, «The American Society of Civil Engineers' report card on America's infrastructure», in *Women in infrastructure*, Springer, 2022, pp. 5–21.

[114]«EN 1992-2 Eurocode 2 - Design of concrete structures - Concrete bridges - Design and detailing rules». European Committee for Standardization - CEN, Brussels, 2005.

[115]«Norme Tecniche per le Costruzioni D.M. 17/01/2018». Italian Ministry of Infrastructure and Transport, 2018. [Online]. Available on: www.gazzettaufficiale.it/eli/id/2008/02/04/08A00368/sg

[116]P. Bencivenga *et al.*, «Evolution of design traffic loads for Italian road bridges», presentato al Proceedings of the 1st Conference of the European Association on Quality Control of Bridges and Structures: EUROSTRUCT 2021 1, Springer, 2022, pp. 1351–1358.

[117]«Compilation of Existing State Truck Size and Weight Limit Laws». U.S. Department of Transportation Federal Highway Administration, maggio 2015. [Online]. Disponibile su: https://ops.fhwa.dot.gov/freight/policy/rpt_congress/truck_sw_laws/index.htm#back

[118]«The Official Highway Code 2007 Edition». UK Department for Transport, Driving Standards Agency - The Stationery Office, 2017.

[119]V. F. Caspani, D. Tonelli, F. Poli, e D. Zonta, «Designing a Structural Health Monitoring System Accounting for Temperature Compensation», *Infrastructures*, vol. 7, fasc. 1, p. 5, dic. 2021, doi: 10.3390/infrastructures7010005.

[120]«Ministerial circular n. 384 of 14/02/1962 – Rules related to loads for the calculation of road bridges». Italian Ministry of Public Works, 1962.

[121]M. P. Pietrangeli, *Progettazione e costruzione di ponti*. Milano: Casa Editrice Ambrosiana, 2001.

[122]A. Passaro, «Relazione di calcolo, Viadotto Alveo Vecchio - Report Autostrade». Concessioni e Costruzioni Autostrade S.p.A., 1966.

[123]«ISO 15630-1:2010 Steel for the reinforcement and prestressing of concrete - Test methods - Part 1: Reinforcing bars, wire rod and wire». European Committee for Standardization - CEN, Brussels, 2010.

[124]«EN 1992-1-1 Eurocode 2: Design of concrete structures – Part 1-1: General rules and rules for buildings». European Committee for Standardization - CEN, Brussels, 2005.

[125]«OpenSees». Pacific Earthquake Engineering Research, 2006. [Online]. Available on: https://opensees.berkeley.edu/.

[126]S. Mazzoni, F. McKenna, M. H. Scott, e G. L. Fenves, «OpenSees command language manual», *Pacific earthquake engineering research (PEER) center*, vol. 264, fasc. 1, pp. 137–158, 2006.

[127]D. Tonelli, C. Cappello, e D. Zonta, «Performance-based design of structural health monitoring systems», presented to al European Workshop on Structural Health Monitoring: Special Collection of 2020 Papers-Volume 2, Springer, 2021, pp. 238–247.

[128]L. Possidente, A. Weiss, D. De Silva, S. Pustorino, E. Nigro, e N. Tondini, «Fire safety engineering principles applied to a multi-storey steel building», *Proceedings of the Institution of Civil Engineers-Structures and Buildings*, vol. 174, fasc. 9, pp. 725–738, 2021.

[129]M. F. Bado e J. R. Casas, «A review of recent distributed optical fiber sensors applications for civil engineering structural health monitoring», *Sensors*, vol. 21, fasc. 5, p. 1818, 2021.

[130]C. M. Bishop, «Pattern recognition and machine learning», *Springer google schola*, vol. 2, pp. 645–678, 2006.

[131]D. J. Ewins, *Modal testing: theory, practice and application*. John Wiley & Sons, 2009.

[132]D. Tonelli, M. Luchetta, F. Rossi, P. Migliorino, e D. Zonta, «Structural Health Monitoring Based on Acoustic Emissions: Validation on a Prestressed Concrete Bridge Tested to Failure», *Sensors*, vol. 20, fasc. 24, p. 7272, dic. 2020, doi: 10.3390/s20247272.

[133]D. Tonelli *et al.*, «Acoustic emission monitoring of prestressed concrete bridges: Differences before and after the first-crack opening», present to al Civil Structural Health Monitoring: Proceedings of CSHM-8 Workshop 8, Springer, 2021, pp. 389–402.

[134]ASCE, «2017 infrastructure report card», presented to al American Society of Civil Engineers, 2017.

[135]D. Zonta *et al.*, «L'esperienza del campo prove Sicurezza Infrastrutture MIT», *EDI-CEM Srl Strade Autostrade*, vol. 142, pp. 58–65, 2020.

[136]D. Bolognani, A. Verzobio, D. Tonelli, C. Cappello, B. Glisic, e D. Zonta, «An application of Prospect Theory to a SHM-based decision problem», presented to Health Monitoring of Structural and Biological Systems 2017, SPIE, 2017, pp. 524–541.

[137]D. Bolognani, A. Verzobio, D. Tonelli, C. Cappello, B. Glisic, e D. Zonta, «Quantifying the benefit of SHM: what if the manager is not the owner», *Proceedings of the 11th IWSHM, Stanford, CA, USA*, pp. 12–14, 2017.

[138]D. Tonelli *et al.*, «The conditional value of information of SHM: what if the manager is not the owner?», presented to al Health Monitoring of Structural and Biological Systems XII, SPIE, 2018, pp. 542–561.

[139]T. Shiotani, Y. Oshima, M. Goto, e S. Momoki, «Temporal and spatial evaluation of grout failure process with PC cable breakage by means of acoustic emission», *Construction and Building Materials*, vol. 48, pp. 1286–1292, 2013.

[140]K. M. Holford e R. J. Lark, «Acoustic Emission Testing Bridges», 2005.

[141]M. Ohtsu, «History and fundamentals», *Acoustic Emission Testing: Basics for Research–Applications in Engineering*, pp. 11–20, 2022.

[142]D. G. Aggelis, «Classification of cracking mode in concrete by acoustic emission parameters», *Mechanics Research Communications*, vol. 38, fasc. 3, pp. 153–157, 2011.

[143]M. Ohtsu e D. G. Aggelis, «Sensors and instruments», *Acoustic Emission Testing: Basics for Research–Applications in Engineering*, pp. 21–44, 2022.

[144]W. Wu, D. W. Greve, e I. J. Oppenheim, «Characterization and noise analysis of capacitive MEMS acoustic emission transducers», presented to al SENSORS, 2007 IEEE, IEEE, 2007, pp. 1152–1155.

[145]X. Jin, I. Ladabaum, e B. T. Khuri-Yakub, «The microfabrication of capacitive ultrasonic transducers», *journal of microelectromechanical systems*, vol. 7, fasc. 3, pp. 295–302, 1998.

[146]International Organization for Standardization, *Non-destructive Testing, Acoustic Emission Inspection, Vocabulary*. International Organization for Standardization, 2001.

[147]T. Shiotani, «Parameter analysis», in *Acoustic emission testing: basics for research-applications in civil engineering*, Springer, 2008, pp. 41–51.

[148]M. Noorsuhada, «An overview on fatigue damage assessment of reinforced concrete structures with the aid of acoustic emission technique», *Construction and Building Materials*, vol. 112, pp. 424–439, 2016.

[149]A. Schiavi, G. Niccolini, P. Tarizzo, A. Carpinteri, G. Lacidogna, e A. Manuello, «Waveforms and frequency spectra of elastic emissions due to macrofractures in solids», presentato al Experimental and Applied Mechanics, Volume 6: Proceedings of the 2011 Annual Conference on Experimental and Applied Mechanics, Springer, 2011, pp. 613–621.

[150]Z. Moradian e B. Q. Li, «Hit-based acoustic emission monitoring of rock fractures: Challenges and solutions», present to al Advances in Acoustic Emission Technology: Proceedings of the World Conference on Acoustic Emission–2015, Springer, 2017, pp. 357–370.

[151]A. G. Beattie, «Acoustic emission non-destructive testing of structures using source location techniques.», Sandia National Lab.(SNL-NM), Albuquerque, NM (United States), 2013.

[152]A. S. Tillmann, A. E. Schultz, e J. E. Campos, «Protocols and criteria for acoustic emission monitoring of fracture-critical steel bridges», 2015.

[153]Z. Nazarchuk, V. Skalskyi, e O. Serhiyenko, «Acoustic emission», *Foundations of Engineering Mechanics*, 2017.

[154]«Campo Prove Sicurezza Infrastrutture MIT-Protocollo di Prova e Strumentazione Campata C3sx». Università degli Studi di Trento: Trento, Italy., 2019.

[155]«Università degli Studi di Trento. Campo Prove Sicurezza Infrastrutture MIT - Resoconto Prove su Campata C3sx». Università degli Studi di Trento: Trento, Italy, 2019.

[156]M. K. ElBatanouny, A. Larosche, P. Ziehl, e L. Yu, «Wireless acoustic emission monitoring on in situ decommissioning for nuclear structures», presentato al Proc., 8th Int. Conf. on Nuclear Plant Instrumentation, Control, and Human-Machine Interface Technologies (NPIC & HMIT). La Grange Park, IL: American Nuclear Society, 2012.

[157]M. Ohtsu, T. Isoda, e Y. Tomoda, «Acoustic emission techniques standardized for concrete structures», *Journal of Acoustic Emission*, vol. 25, fasc. 2007, pp. 21–32, 2007.

[158]JCMS-III B5706, «Monitoring method for active cracks in concrete by acoustic emission», *Federation of Construction Material Industries, Japan*, pp. 23–28, 2003.

[159]T. J. Hadzor, R. W. Barnes, P. H. Ziehl, J. Xu, e A. K. Schindler, «Development of acoustic emission evaluation method for repaired prestressed concrete bridge girders.», Auburn University. Highway Research Center, 2011.

[160]R. Zandonini, N. Baldassino, F. Freddi, e G. Roverso, «Steel-concrete frames under the column loss scenario: An experimental study», *Journal of Constructional Steel Research*, vol. 162, p. 105527, 2019.

[161]S. Kashif Ur Rehman, Z. Ibrahim, S. A. Memon, e M. Jameel, «Nondestructive test methods for concrete bridges: A review», *Construction and Building Materials*, vol. 107, pp. 58–86, mar. 2016, doi: 10.1016/j.conbuildmat.2015.12.011.

[162]X. Dérobert, C. Aubagnac, e O. Abraham, «Comparison of NDT techniques on a post-tensioned beam before its autopsy», *NDT & E International*, vol. 35, fasc. 8, pp. 541–548, dic. 2002, doi: 10.1016/S0963-8695(02)00027-0.

[163]A. Agresti, *Categorical data analysis*, 3rd ed. in Wiley series in probability and statistics, no. 792. Hoboken, NJ: Wiley, 2013.

[164]J. L. Myers e A. D. Well, *Research design and statistical analysis*, 2. ed. Mahwah, NJ London: Erlbaum, 2003.

[165]D. Freedman, R. Pisani, e R. Purves, *Statistics*, International student ed., 4. ed. New York: Norton, 2007.

[166]K. G. Jöreskog, «On the estimation of polychoric correlations and their asymptotic covariance matrix», *Psychometrika*, vol. 59, fasc. 3, pp. 381–389, set. 1994, doi: 10.1007/BF02296131.

[167]J. Ekström, «A generalized definition of the polychoric correlation coefficient», 2011.

[168]L. A. Goodman e W. H. Kruskal, «Measures of Association for Cross Classifications», *Journal of the American Statistical Association*, vol. 49, fasc. 268, p. 732, dic. 1954, doi: 10.2307/2281536.

[169]M. G. Kendall, «A New Measure of Rank Correlation», *Biometrika*, vol. 30, fasc. 1–2, pp. 81–93, giu. 1938, doi: 10.1093/biomet/30.1-2.81.

[170]A. Stuart, «The Estimation and Comparison of Strengths of Association in Contingency Tables», *Biometrika*, vol. 40, fasc. 1/2, p. 105, giu. 1953, doi: 10.2307/2333101.

[171]L. Taerwe, L. Taerwe, e International Federation for Structural Concrete, A c. di, *Durability of post-tensioning tendons: proceedings of a workshop held at Ghent University on 15 - 16 November 2001 ; technical report*. in Bulletin / International Federation for Structural Concrete, no. 15. Lausanne: International Federation for Structural Concrete, 2001.

[172]«(Pernica & Rahman, 1997) - Effectiveness of an Electromagnetic Wave Propagation Technique for the Condition Assessment of Un... .pdf».

[173]N. Altman e M. Krzywinski, «Association, correlation and causation», *Nat Methods*, vol. 12, fasc. 10, Art. fasc. 10, ott. 2015, doi: 10.1038/nmeth.3587.

[174]D. S. Yates, D. S. Moore, e D. S. Starnes, *The practice of statistics*, 2. ed. New York, NY: Freeman, 2003.

[175]A. Agresti, *Categorical data analysis*, 3rd ed. in Wiley series in probability and statistics, no. 792. Hoboken, NJ: Wiley, 2013.

[176]R. Likert, «A technique for the measurement of attitudes.», *Archives of psychology*, 1932.

[177]I. E. Allen e C. A. Seaman, «Likert scales and data analyses», *Quality progress*, vol. 40, fasc. 7, pp. 64–65, 2007.

[178]K. P. Murphy, *Machine learning: a probabilistic perspective*, 4. print. (fixed many typos). in Adaptive computation and machine learning series. Cambridge, Mass.: MIT Press, 2013.

[179]M. Baak, R. Koopman, H. Snoek, e S. Klous, «A new correlation coefficient between categorical, ordinal and interval variables with Pearson characteristics», *Computational Statistics & Data Analysis*, vol. 152, p. 107043, dic. 2020, doi: 10.1016/j.csda.2020.107043.

[180]P. Capéraà e C. Genest, «Spearman's ρ is larger than Kendall's τ for positively dependent random variables», *Journal of Nonparametric Statistics*, vol. 2, pp. 183–194, apr. 2007, doi: 10.1080/10485259308832551.

[181]K. J. Berry, J. E. Johnston, S. Zahran, e P. W. Mielke, «Stuart's tau measure of effect size for ordinal variables: Some methodological considerations», *Behavior Research Methods*, vol. 41, fasc. 4, pp. 1144–1148, nov. 2009, doi: 10.3758/BRM.41.4.1144.

[182]A. Barbiero e A. Hitaj, «Goodman and Kruskal's Gamma Coefficient for Ordinalized Bivariate Normal Distributions», *Psychometrika*, vol. 85, fasc. 4, pp. 905–925, dic. 2020, doi: 10.1007/s11336-020-09730-5.

[183]F. P. Holgado–Tello, S. Chacón–Moscoso, I. Barbero–García, e E. Vila–Abad, «Polychoric versus Pearson correlations in exploratory and confirmatory factor analysis of ordinal variables», *Qual Quant*, vol. 44, fasc. 1, Art. fasc. 1, gen. 2010, doi: 10.1007/s11135-008-9190-y.

[184]J. Choi, M. Peters, e R. O. Mueller, «Correlational analysis of ordinal data: from Pearson's r to Bayesian polychoric correlation», *Asia Pacific Educ. Rev.*, vol. 11, fasc. 4, pp. 459–466, dic. 2010, doi: 10.1007/s12564-010-9096-y.

[185]U. Olsson, «Maximum likelihood estimation of the polychoric correlation coefficient», *Psychometrika*, vol. 44, fasc. 4, pp. 443–460, dic. 1979, doi: 10.1007/BF02296207.

[186]J. Choi, S. Kim, J. Chen, e S. Dannels, «A Comparison of Maximum Likelihood and Bayesian Estimation for Polychoric Correlation Using Monte Carlo Simulation», *Journal of Educational and Behavioral Statistics*, vol. 36, fasc. 4, pp. 523–549, ago. 2011, doi: 10.3102/1076998610381398.

[187]J. Fox, *polycor: Polychoric and Polyserial Correlations*. 2022. [Online]. Disponibile su: https://CRAN.R-project.org/package=polycor

[188]R Core Team, *R: A Language and Environment for Statistical Computing*. Vienna, Austria: R Foundation for Statistical Computing, 2023. [Online]. Disponibile su: https://www.R-project.org/